Öskurhóll, Hveravellir at Kjölur

Yohannes Lemma Didana

MULTIDIMENSIONAL INVERSION OF MT DATA FROM KRÝSUVÍK HIGH-TEMPERATURE GEOTHERMAL FIELD, SW-ICELAND, AND STUDY OF HOW 1D AND 2D INVERSION CAN REPRODUCE A GIVEN 2D/3D RESISTIVITY STRUCTURE USING SYNTHETIC MT DATA

MULTIDIMENSIONAL INVERSION OF MT DATA FROM KRÝSUVÍK HIGH-TEMPERATURE GEOTHERMAL FIELD, SW ICELAND, AND STUDY OF HOW 1D AND 2D INVERSION CAN REPRODUCE A GIVEN 2D/3D RESISTIVITY STRUCTURE USING SYNTHETIC MT DATA

MSc thesis
School of Engineering and Natural Sciences
Faculty of Earth Sciences
University of Iceland

by

Yohannes Lemma Didana
Geological Survey of Ethiopia - GSE
Geothermal Resource Exploration and Assessment Core Process
P.O. Box 2302
Addis Ababa
ETHIOPIA
yohlema@yahoo.com, dyohanneslemma@ymail.com

INTRODUCTION

The Geothermal Training Programme of the United Nations University (UNU) has operated in Iceland since 1979 with six month annual courses for professionals from developing countries. The aim is to assist developing countries with significant geothermal potential to build up groups of specialists that cover most aspects of geothermal exploration and development. During 1979-2010, 452 scientists and engineers from 47 countries have completed the six month courses. They have come from Asia (42%), Africa (29%), Central America (15%), and Central and Eastern Europe (14%). There is a steady flow of requests from all over the world for the six month training and we can only meet a portion of the requests. Most of the trainees are awarded UNU Fellowships financed by the UNU and the Government of Iceland.

Candidates for the six month specialized training must have at least a BSc degree and a minimum of one year practical experience in geothermal work in their home countries prior to the training. Many of our trainees have already completed their MSc or PhD degrees when they come to Iceland, but several excellent students who have only BSc degrees have made requests to come again to Iceland for a higher academic degree. In 1999, it was decided to start admitting UNU Fellows to continue their studies and study for MSc degrees in geothermal science or engineering in co-operation with the University of Iceland. An agreement to this effect was signed with the University of Iceland. The six month studies at the UNU Geothermal Training Programme form a part of the graduate programme.

It is a pleasure to introduce the 24th UNU Fellow to complete the MSc studies at the University of Iceland under the co-operation agreement. Mr. Yohannes Lemma, BSc in Physics, of the Geological Survey of Ethiopia, completed the six month specialized training in Geophysical Exploration at the UNU Geothermal Training Programme in October 2007. His research report was entitled: "Magnetotelluric and transient electromagnetic method in geothermal exploration, with an example from Tendaho geothermal field, Ethiopia". After one year of geothermal research work in Ethiopia, he came back to Iceland for MSc studies at the Faculty of Earth Sciences of the University of Iceland in August 2008. In April 2010, he defended his MSc thesis presented here, entitled "Multidimensional inversion of MT data from Krýsuvík high-temperature geothermal field, SW Iceland, and study of how 1D and 2D inversion can reproduce a given 2D/3D resistivity structure using synthetic MT data". His studies in Iceland were financed by the Government of Iceland through a UNU-GTP Fellowship from the UNU Geothermal Training Programme. We congratulate him on his achievements and wish him all the best for the future. We thank the Faculty of Earth Sciences at the School of Engineering and Natural Sciences of the University of Iceland for the co-operation, and his supervisors for the dedication.

Finally, I would like to mention that Yohannes' MSc thesis with the figures in colour is available for downloading on our website *www.unugtp.is* under publications.

With warmest wishes from Iceland,

Ingvar B. Fridleifsson, director
United Nations University
Geothermal Training Programme

ACKNOWLEDGEMENTS

ABSTRACT

Electromagnetic (EM) methods are frequently used in the exploration of geothermal resources for determining the spatial distribution of electrical conductivity. Of the various EM methods, magnetotelluric (MT) method was found to be the most effective in defining a conductive reservoir at a depth exceeding 1 km overlain by a larger and more conductive clay cap.

The two main objectives of this study are: firstly to explore how 1D and 2D inversion can reproduce a given 2D and 3D resistivity structure using synthetic MT data and secondly to investigate the subsurface resistivity distribution of Krýsuvík high-temperature geothermal field in SW-Iceland, using multidimensional inversion of MT data. The 2D and 3D synthetic models considered in the study were better reproduced by 1D inversion of the determinant of impedance tensor and 2D inversion of TM mode data than by 2D inversion of TE mode and combined TE and TM mode data. 1D and 2D inversion of MT data along two profiles and 3D inversion of 58 MT sites were performed in Krýsuvík area. In the 1D inversion of MT data, transient electromagnetic (TEM) data from the same location as the MT soundings are jointly inverted in order to correct the static shift in the MT data. The 2D and 3D inversion of MT data were performed on previously shift corrected MT data. The full impedance tensor elements were used in the 3D inversion of MT data. The Atlantic Ocean was included as a fixed feature in the 2D and 3D inversion to account for the effect of the highly conductive ocean on MT measurements. The 1D and 2D inversion of MT data from Krýsuvík high-temperature geothermal field revealed three main resistivity structures down to a depth of 10 km: a high-resistivity surface layer underlain by conductive layer followed by high resistivity. The 3D inversion confirmed this main result. In addition, the 3D inversion model showed a low-resistivity zone trending ENE-WEW at a depth of about 1.35 km which has the same direction as transform faults inferred from seismicity. The nature of this low resistivity which is overlain by high resistivity is not well known. The 3D inversion, moreover, revealed a deep conductive body embedded at a depth of about 2 km and reaching a depth of 5 km within the high resistivity. It is located in the central part of Krýsuvík area between the two hyaloclastites ridges and is about 10 km2 in horizontal dimension. The deep conductive body is presumably associated with the heat source of the geothermal system.

TABLE OF CONTENTS

LIST OF FIGURES

NOMENCLATURE

$\vec{E}$ (V m-1)   Electric field
$\vec{B}$ (T)   Magnetic Induction
$\vec{H}$ (A m-1)   magnetic intensity
$\vec{D}$ (C m-2)   Electric Displacement
η (Cm-3)   Electric Charge Density of free charges
$\vec{j}$ (Am-2)   Electric Current Density
σ (Sm-1)   Electric Conductivity
μ (H/m)   Magnetic Permeability
ε (F/m)   Electric Permittivity
δ (m)   Electromagnetic Skin Depth
T (s)   Period
f (Hz)   Frequency
t (s)   Time
ω (rad/s)   Angular Frequency
ρ (Ωm)   Resistivity (specific resistance)
$\hat{Z}$ (Ω)   Impedance tensor (2x2 matrices)
$(\hat{Y})$ ((Ωm)-1 or S)   Admittance
χe Dielectric Susceptibility
k (m-1)   Propagation Constant (wave number)
x, y and x´, y´   Reference Frame and Reference Frame Rotated through an angle θ
T   Tipper
R   Real
I   Imaginary
Mr   Length of the real induction arrow
Mq   Length of the imaginary induction arrow
ρa (Ωm)   Apparent Resistivity
φ (°)   Impedance phase
I=√-1   Imaginary number

ACRONYMS AND ABBREVIATIONS

MT   Magnetotelluric
TEM   Transient Electromagnetic
ÍSOR   Iceland GeoSurvey
TE   Transverse Electric
TM   Transverse Magnetic
1D   One dimensional
2D   Two dimensional
3D   Three dimensional
ADU-06   Analogue-Digital Unit (Metronix data logger)
REBOCC   REduced Basis OCCam Inversion
EM   Electromagnetic

1. INTRODUCTION

Electromagnetic (EM) data provide a substantial contribution to the geophysical mapping and monitoring of geothermal reservoirs. Magnetotellurics (MT) and Transient Electromagnetic (TEM) methods are widely used in geothermal exploration. Geothermal resources are ideal targets for EM methods since they produce strong variations in subsurface electrical resistivity.

The MT method has been used in geothermal exploration since the early 1970s (Berktold, 1983). In the last decade, the advancement of computing has allowed realistic modelling and inversion of MT data leading to the characterization of electrical resistivity structure of geothermal reservoirs (Newman et al., 2008).

Krýsuvík is one of the high-temperature geothermal areas on Reykjanes peninsula in south west Iceland. A total of 96 MT and more than 200 TEM sites were acquired from Krýsuvík high-temperature geothermal field and surrounding area since 1989 (Eysteinsson, 1999 & 2001; Hersir et al., 2010). These data are used to study the subsurface resistivity distribution of Krýsuvík high-temperature geothermal field.

1D and 2D inversion of synthetic MT data are also presented, generated from 3D models. The goal of the synthetic data analysis is to study how 1D and 2D inversion can reproduce a given 2D and 3D resistivity structure.

The overall objective of this study can be summarized as:

1. Study how 1D and 2D MT inversion can reproduce a given 2D and 3D resistivity structure using synthetic MT data.
2. Image the subsurface resistivity distribution of Krýsuvík high-temperature geothermal field using 1D, 2D and 3D inversion of MT data. Correlate the resulting resistivity structure with other geophysical investigations, geology and alteration mineralogy from boreholes in the area.

The MT theory, field procedure and data processing will be presented in the thesis.

2. THEORY: THE MT METHOD

2.1 MT overview

Magnetotellurics (MT) is a passive exploration technique that utilises a broad spectrum of the naturally occurring geomagnetic variations as a source for electromagnetic induction in the Earth. The MT technique involves measuring fluctuations in the natural electric, **E**, and magnetic, **B**, fields in orthogonal directions on the surface of the Earth as a means of determining the conductivity structure of the Earth at depths ranging from a few tens of metres to several hundreds of kilometres. The fundamental theory of MT was first propounded by Tikhonov (1950, reprinted 1986) and, in more detail, by Cagniard (1953). Central to the theses of both authors was the realisation that electromagnetic responses from any depth could be obtained by extending the sounding period (T). This principle is embodied in the electromagnetic skin depth relation, which describes the exponential decay of electromagnetic fields as they diffuse into a medium:

$$\delta(T) = (T/\pi\mu\bar{\sigma})^{1/2}$$

Where $\delta(T)$ is the electromagnetic skin depth in metres at a given period, T, $\bar{\sigma}$ is the average conductivity of the medium penetrated and μ is magnetic permeability.

At a depth, $\delta(T)$, the real part of electromagnetic fields has attenuated to e^{-1} of the amplitude at the surface of the Earth. Hence, in MT studies, one electromagnetic skin depth is generally equated with the *penetration depth* of electromagnetic fields into the Earth.

By Faraday´s Law of Induction, varying magnetic field induces an electric current within conductors like the Earth, and by Ohm´s Law this current generates an electric field. The strength of the electric field is dependent on the conductivity of the medium and strength of inducing source magnetic field. Hence, by observing the magnetic and electric fields simultaneously, determining their ratios at varying frequencies, one can derive the conductivity variations with depth.

On the surface of the Earth, one measures the time variations of the three components of the magnetic field (H_x, H_y, and H_z), and the two horizontal components of the Earth´s electric field (E_x and E_y). An example of their variation is shown in Figure 1 from a measuring site in Krýsuvík.
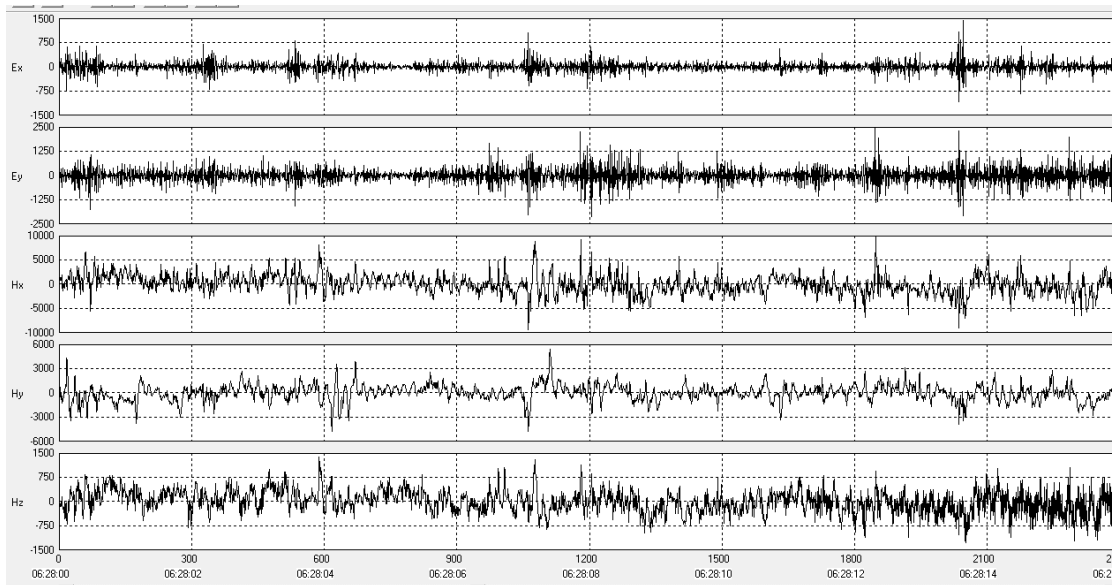
FIGURE 1: Typical MT time series. The times series show the E_x, E_y, H_x, H_y, and H_z components of electric (in mV/m) and magnetic (in nT) fields, respectively. It is measured on 16/07/07, and is the 16 s high frequency band

There are two frequency bands that are problematic in MT data acquisition. The most well-known one is the so-called *MT dead band*, frequencies between about 0.1-10 Hz. Not only is there low signal at these frequencies but also there is a natural maximum in the near surface micro-seismic noise due to coupling of the wind with the ground.

The MT method depends on the penetration of the EM energy into the Earth. The MT method operates under two main assumptions: First, we assume a quasi-static approximation by neglecting displacement currents. Mathematically, the wave equation of EM propagation becomes the diffusion equation. Secondly, we assume a uniform plane electromagnetic wave source. After impinging upon the Earth, the natural EM fields propagate essentially vertically into Earth because of the large resistivity contrast at the air-Earth interface, which causes a vertical refraction of both fields transmitted into the earth (Vozoff, 1972). The time varying horizontal magnetic field induces a horizontal electric field at right angles through Faraday's law. The electric field in the conducting earth drives the telluric currents (Vozoff, 1991).

2.2 Source field in MT

Electromagnetic field with frequencies higher than 1 Hz (i.e. periods shorter than 1 s) have their origins in meteorological activity such as lightening discharges. The lightening discharges from equatorial regions, which propagate around the world within the waveguide bounded by the ionosphere and Earth´s surface, are of most significance. The signals discharged by lightening are known as "sferics" and encompass a broad range of electromagnetic frequencies. Sferics propagates around the world within the waveguide bounded by the ionosphere and Earth´s surface. During the day, the waveguide is ~ 60 km wide, increasing to ~90 km at night-time.

Interactions between the solar wind (Parker, 1958) and the Earth´s magnetosphere and ionosphere generate electromagnetic fluctuations with frequencies lower than 1 Hz (i.e. periods longer than 1 s). Briefly, the solar wind is a continual stream of plasma, radiating mainly protons and electrons from the sun. On encountering the terrestrial magnetic field (at the magnetopause), these charged particles are deflected in opposite directions, thereby establishing an electric field (Figure 2). Variations in density, velocity and magnetic field intensity of the solar wind produce rapidly varying distortions of the Earth's magnetosphere.
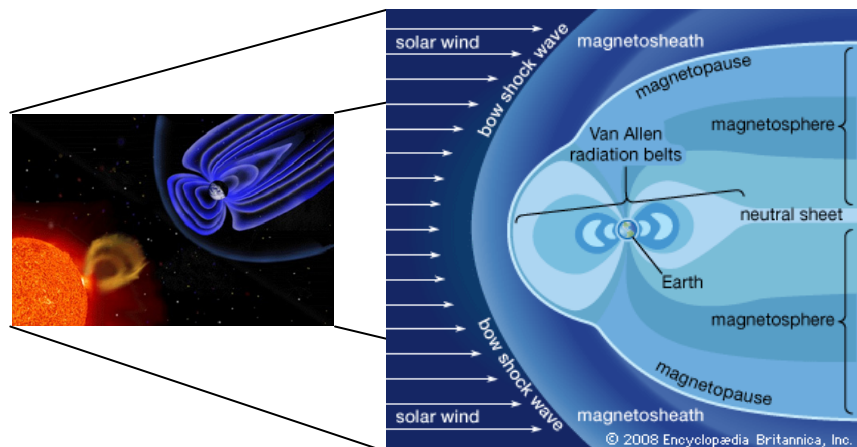
FIGURE 2: Interaction of solar wind with the magnetosphere. Source region for low frequency (< 1 Hz) natural EM fields (taken from Encyclopaedia Britannica, 2010)

The largest geomagnetic field variations on the earth surface (up to the order of a few hundred nT) take place during *magnetic storms*, which occur owing to increases in the rate at which plasma is ejected from the sun. Magnetic storms can last for several days, and in Polar Regions can lead to magnificent displays of light known as *aurora borealis* and *aurora australis*, or *northern and southern lights*, respectively. Auroras are associated with the solar wind, a flow of ions continuously flowing outward from the sun. The Earth's magnetic field traps these particles, many of which travel toward the poles where they are accelerated towards the earth.

2.3 Basic EM theory and Maxwell's equations

The behaviour of electromagnetic fields is described by Maxwell's Equations expressed as:

$$\nabla \times \vec{E} = -\frac{\partial \vec{B}}{\partial t} \qquad \text{Faraday's Law} \qquad (2.3.1)$$

$$\nabla \times \vec{H} = \vec{j} + \frac{\partial \vec{D}}{\partial t} \qquad \text{Ampere's Law} \qquad (2.3.2)$$

$$\vec{\nabla} \cdot \vec{B} = 0 \qquad \text{Gauss's Law for Magnetism} \quad (2.3.3)$$

$$\vec{\nabla} \cdot \vec{D} = \eta \qquad \text{Gauss's Law} \qquad (2.3.4)$$

where $\vec{E}$ is the electric field (Vm^{-1}), $\vec{B}$ is the magnetic field (T), $\vec{H}$ is the magnetic intensity (Am^{-1}), $\vec{D}$ is the electric displacement (Cm^{-2}), η is the electric charge density owing to free charges (Cm^{-3}) and $\vec{j}$ is the electric current density owing to free charges (Am^{-2}). The symbols $\nabla \times$ and $\nabla \cdot$ stand for curl and divergence, respectively.

For a linear, isotropic medium, the following relationships have been shown to hold (constitutive relationships):

$$\vec{B} = \mu \vec{H} \qquad (2.3.5a)$$

$$\vec{D} = \varepsilon \vec{E} \qquad (2.3.5b)$$

$$\vec{j} = \sigma \vec{E} \qquad (2.3.5c)$$

where σ is the electric conductivity (Sm^{-1}) which is the reciprocal of electrical resistivity (ρ), μ is the magnetic permeability (H/m) and ε is the electric permittivity (F/m).

σ, ε and μ describe intrinsic properties of the materials through which the electromagnetic fields propagate. In anisotropic materials they are expressed in a tensor form.

As well as these formulae that govern how EM waves travel through a uniform medium, there are conditions that must be met by the EM fields at the boundary where two media of different conductivity are in contact. These boundary conditions are that the normal component of the current density, j_n, the normal component of the magnetic field, B_n, and the tangential component of the electric field, E_t, must all be continuous across the boundary, i.e. they must be of the same value on both sides of the boundary.

2.4 Diffusion of EM fields

Maxwell's Equations are valid for a medium which is both homogeneous and isotropic; i.e. we require the intrinsic properties of the material ε, μ and σ to be constant in time and space. We can re-write Equations 2.3.1 and 2.3.2 using the constitutive Equations 2.3.5a-2.3.5c as:

$$\nabla \times E = -\mu \frac{\partial H}{\partial t} \qquad (2.4.1)$$

$$\nabla \times H = \sigma E + \varepsilon \frac{\partial E}{\partial t} \qquad (2.4.2)$$

The electric charge density, η, is zero in Equation 2.3.4 since no charges can be collected in a homogeneous conducting medium. There are no free charges in such a medium. Therefore Equation 2.3.4 can be re-written as:

$$\nabla \cdot E = 0. \qquad (2.4.3)$$

By taking the time derivative of Equation 2.4.2 and multiplying by μ and using Equation 2.4.1, we get:

$$-\nabla \times \nabla \times \boldsymbol{E} = \mu\sigma \frac{\partial \boldsymbol{E}}{\partial t} + \mu\varepsilon \frac{\partial^2 \boldsymbol{E}}{\partial t^2}$$

Using the vector identity:

$$\times \nabla \times \boldsymbol{A} = -\nabla^2 \boldsymbol{A} + \nabla(\nabla \cdot \boldsymbol{A}) \tag{2.4.4}$$

And considering the divergence condition in Equation 2.4.3, we get:

$$\nabla^2 \boldsymbol{E} - \mu\sigma \frac{\partial \boldsymbol{E}}{\partial t} - \mu\varepsilon \frac{\partial^2 \boldsymbol{E}}{\partial t^2} = 0 \tag{2.4.5}$$

Similarly by performing the same operation on Equation 2.4.1 and 2.4.2, we have:

$$\nabla^2 \boldsymbol{H} - \mu\sigma \frac{\partial \boldsymbol{H}}{\partial t} - \mu\varepsilon \frac{\partial^2 \boldsymbol{H}}{\partial t^2} = 0 \tag{2.4.6}$$

Equations 2.4.5 and 2.4.6, which completely describe the electric and magnetic fields in a homogeneous medium, are called *the telegraphers' equations* (Zhdanov and Keller, 1994).

When σ = 0, the telegraphers' Equations 2.4.5 and 2.4.6 can be written as follows:

$$\nabla^2 \boldsymbol{E} - \mu\varepsilon \, \partial^2 \boldsymbol{E}/\partial t^2 = 0$$

$$\nabla^2 \boldsymbol{H} - \mu\varepsilon \, \partial^2 \boldsymbol{H}/\partial t^2 = 0$$

These equations are called non-diffusive *wave equations*. They describe the nature of electromagnetic wave propagation in a non-conductive medium.

Re-writing Faraday's and Ampere's-Maxwell's Laws using the constitutive equations and assuming the time dependency $e^{-i\omega t}$ of the fields, with angular frequency being ω = 2π/T, gives:

$$\nabla \times \boldsymbol{E} = -\frac{\partial \boldsymbol{B}}{\partial t} = i\omega\mu\boldsymbol{H} \tag{2.4.7}$$

$$\nabla \times \boldsymbol{H} = \boldsymbol{J} + \frac{\partial \boldsymbol{D}}{\partial t} = (\sigma - i\omega\varepsilon)\boldsymbol{E} \tag{2.4.8}$$

Taking the curl of both of these equations, and substituting the above equations, gives:

$$\nabla \times \nabla \times \mathrm{E} = i\omega\mu(\nabla \times \mathrm{H}) = i\omega\mu(\sigma - i\omega\varepsilon)\mathrm{E} \tag{2.4.9}$$

$$\nabla \times \nabla \times \boldsymbol{H} = (\sigma - i\omega\varepsilon)\nabla \times \boldsymbol{E} = (\sigma - i\omega\varepsilon)i\omega\mu\boldsymbol{H} \tag{2.4.10}$$

Using the vector identity in Equation 2.4.4 and the divergence conditions in Equation 2.4.3, Equation 2.4.9 can be written as:

$$\nabla \times \nabla \times \boldsymbol{E} = -\nabla^2 \boldsymbol{E} = i\omega\mu(\sigma - i\omega\varepsilon)\boldsymbol{E}$$

$$\nabla^2 \boldsymbol{E} + i\omega\mu(\sigma - i\omega\varepsilon)\boldsymbol{E} = 0 \tag{2.4.11}$$

Similarly, Equation 2.4.10 can be written as:

$$\nabla \times \nabla \times \boldsymbol{H} = -\nabla^2 \boldsymbol{H} = (\sigma - i\omega\varepsilon)i\omega\mu\boldsymbol{H}$$

$$\nabla^2 \boldsymbol{H} + i\omega\mu(\sigma - i\omega\varepsilon)\boldsymbol{H} = 0 \tag{2.4.12}$$

The Equations 2.4.11 and 2.4.12 are in the form of the vector Helmholtz differential equation:

$$\nabla^2 \boldsymbol{F} + k^2 \boldsymbol{F} = 0 \qquad \text{(dependency on } \omega \text{ is assumed)}$$

where k is the propagation constant in the medium and is given by:

$$k^2 = i\omega\mu\sigma + \omega^2\mu\varepsilon = \omega\mu(i\sigma + \omega\varepsilon) \qquad (2.4.13)$$

where σ, μ and ε are the uniform conductivity, permeability and permittivity of the medium, respectively, and ω is the angular frequency.

The resistivity of subsurface rocks is usually in the range of $\rho \approx 1 - 10^4 \Omega m$ (or $\sigma \approx$ 1-10^{-4}S/m). The periods used in MT are in the range of $T \approx 10^{-4} - 10^4$ s or $(f \approx 10^4 - 10^{-4} Hz)$. Taking permittivity of vacuum $\varepsilon_o = 8.85$ x 10^{-12} F/m and dielectric susceptibilities of earth materials χ_e in the range 1-100,the maximum value of the product $\omega \varepsilon$ in bracket Equation 2.4.13 is:

$$(\omega\varepsilon)_{max} = 2\pi f \varepsilon_o \chi_e = 2\pi \cdot 10^4 \cdot 8.85 \ x \ 10^{-12} \cdot 100 \approx 5 \cdot 10^{-5}$$

This implies that $\sigma \gg \omega\varepsilon$ (quasi-static approximation) in Equation 2.4.13.

Thus, the wave propagation term, k, in Equation 2.4.13 reduces to:

$$k^2 = i\omega\mu_o\sigma \qquad (2.4.14)$$

And the vector Helmholtz equation reduces to the diffusion equation:

$$\nabla^2 \boldsymbol{F} + i\omega\mu_o\sigma\boldsymbol{F} = 0 \qquad (2.4.15)$$

FIGURE 3: Refraction of a plane EM wave incident on earth´s surface

That describes the diffusion of EM field into the medium.

Equations 2.4.11 and 2.4.12 can be re-written as:

$$\nabla^2 \boldsymbol{E} + i\omega\mu\sigma\boldsymbol{E} = 0 \qquad (2.4.16)$$

$$\nabla^2 \boldsymbol{H} + i\omega\mu\sigma\boldsymbol{H} = 0 \qquad (2.4.17)$$

Consider a plane electromagnetic wave of angular frequency ω with angle of incidence (θ_i) at the surface of a homogeneous earth with resistivity $\rho = 1/\sigma$. The refracted wave propagates into the half space with angle of refraction (θ_t) as shown in Figure 3.

Using Snell´s law we have:

$$\frac{1}{v_o} \sin\theta_i = \frac{1}{v} \sin\theta_t \qquad (2.4.18)$$

where $v_o = \dfrac{1}{\sqrt{\varepsilon_o\mu_o}} = c$ and $v = \sqrt{\dfrac{2\omega}{\mu_o\sigma}}$ are the velocities of the EM wave in air and half space

earth, respectively. c is speed of light.

Substituting v_o and v in Equation 2.4.18 and rearranging:

$$\sin\theta_t = \sin\theta_i \sqrt{\frac{2\varepsilon_o\omega}{\sigma}}$$

Since resistivity of subsurface rocks ρ is $< 10^4 \Omega m$ and $\omega < 10^4$ Hz for MT measurements:

$$\frac{2\varepsilon_o \omega}{\sigma} < 10^{-3}$$

Therefore θ_t is practically zero and the refracted wave travels vertically downwards into the Earth for all angles of incidence θ_i.

Assume Cartesian coordinate system with x in the North direction, y in the East direction and z vertically downwards. When a wave is propagating along the z direction, for a uniform plane wave, there is no variation of electric and magnetic vectors with respect to x or y i.e.

$$\frac{\partial}{\partial x} = 0 \; and \; \frac{\partial}{\partial y} = 0 \; and \; E_z = 0.$$

The scalar forms of Equation 2.4.7 and 2.4.8 (dropping the displacement current terms) are:

$$\frac{\partial E_x}{\partial z} = i\omega\mu_o H_y \tag{2.4.19}$$

$$\frac{\partial H_y}{\partial z} = -\sigma E_x \tag{2.4.20}$$

Differentiating Equations 2.4.19 and 2.4.20 with respect to z, yields:

$$\frac{\partial^2 E_x}{\partial z^2} = i\omega\mu_o \frac{\partial H_y}{\partial z} = -i\omega\mu_o \sigma E_x = -k^2 E_x \tag{2.4.21}$$

$$\frac{\partial^2 H_y}{\partial z^2} = -\sigma \frac{\partial E_x}{\partial z} = -i\omega\mu_o \sigma H_y = -k^2 H_y \tag{2.4.22}$$

The general solutions of Equations 2.4.21 and 2.4.22 are in the form:

$$E_x = Ae^{-ikz} + Be^{ikz} \tag{2.4.23}$$

$$H_y = \frac{k}{\omega\mu_o}\left(Ae^{-ikz} - Be^{ikz}\right) \tag{2.4.24}$$

2.5 A plane EM wave in a horizontally stratified medium

Consider the travel of a plane electromagnetic wave into a flat earth built from a set of horizontal layers. Current flow is excited in the earth by a downward travelling electromagnetic wave. Making use of a coordinate system with z = 0 at the boundary between the atmosphere and the solid earth as shown in Figure 4. The earth consisting of N layers, each with a uniform conductivity, σ_i, and of a thickness, d_i. A monochromatic (single frequency) quasi-stationary electromagnetic field is vertically incident on the earth. We will assume that the magnetic permeability is that of free space everywhere.

FIGURE 4: Surface impedance of a layered earth. Current flow is excited in the earth by a downward travelling EM wave

Referring to Equations 2.4.16 and 2.4.17 within each of the uniform layers, the electric and magnetic fields comprising a plane electromagnetic wave do satisfy the one dimensional Helmholtz equations.

$$\partial^2 H / \partial z^2 + k_j{}^2 H = 0$$

7

$$\partial^2 E / \partial z^2 + k_j{}^2 E = 0$$

For $z_{j-1} \leq z \leq z_j$, where $k_j{}^2 = i\,\omega\mu_0\sigma_j$ is the wave propagation constant for the jth layer $z_j = \sum_1^j d_i$ is the depth to the top of the jth layer.

Solutions to these equations can be written as:

$$E(z) = A_j e^{ik_j Z} + B_j e^{-ik_j Z}$$

$$H(z) = \frac{k_j}{\omega\mu_0}\left(A_j e^{ik_j Z} - B_j e^{-ik_j Z}\right)$$

Where A_j , B_j, j =1, 2, ... ,N are arbitrary vector constants.

The electromagnetic field vectors in a plane wave will always lie in horizontal planes. Because of this the vectors **E** and **H** will have zero components in the z-direction.

$$\vec{E} = \left(E_x, E_y, 0\right)$$

$$\vec{H} = \left(H_x, H_y, 0\right)$$

The horizontal components of the electric fields in layer j are written as:

$$E_x\,(z) = A_{xj} e^{ik_j Z} + B_{xj} e^{-ik_j Z} \tag{2.5.1}$$

$$E_y\,(z) = A_{yj} e^{ik_j Z} + B_{yj} e^{-ik_j Z} \tag{2.5.2}$$

Where $z_{j-1} \leq z \leq z_j$ for all values of z within the layer j or on its bounding surfaces.

We can rewrite Faraday´s laws as shown in Equations 2.3.1 and 2.4.7 for plane electromagnetic waves, using the determinant representation of the term $\nabla \times \boldsymbol{E}$.

$$\begin{vmatrix} \vec{d}_x & \vec{d}_y & \vec{d}_z \\ \frac{\partial}{\partial x} & \frac{\partial}{\partial y} & \frac{\partial}{\partial z} \\ E_x & E_y & 0 \end{vmatrix} = i\omega\mu_0\left(H_x\vec{d}_x + H_y\vec{d}_y\right) \tag{2.5.3}$$

Where $\vec{d}_x, \vec{d}_y, \vec{d}_z$ are unit vectors along the directions of a set of Cartesian coordinates.

Another property of the plane waves is that the field components are identical over the entire xy plane; therefore, the spatial derivatives with respect to x and y are zero, i.e. $\frac{\partial}{\partial x} = 0$ and $\frac{\partial}{\partial y} = 0$, and thus Equation 2.5.3 becomes:

$$\begin{vmatrix} \vec{d}_x & \vec{d}_y & \vec{d}_z \\ 0 & 0 & \frac{d}{dz} \\ E_x & E_y & 0 \end{vmatrix} = i\omega\mu_0\left(H_x\vec{d}_x + H_y\vec{d}_y\right) \tag{2.5.4}$$

Which gives:

$$H_x = -\frac{1}{i\omega\mu_0}\frac{dE_y}{dz} \tag{2.5.5}$$

$$H_y = \frac{1}{i\omega\mu_0}\frac{dE_x}{dz} \tag{2.5.6}$$

With appropriate substitution from Equations 2.5.1 and 2.5.2 into Equations 2.5.5 and 2.5.6, we get:

$$H_x\,(z) = \frac{-k_j}{\omega\mu_0}\left(A_{yj}e^{ik_jZ} - B_{yj}e^{-ik_jZ}\right) \tag{2.5.7}$$

$$H_y\,(z) = \frac{k_j}{\omega\mu_0}\left(A_{xj}e^{ik_jZ} - B_{xj}e^{-ik_jZ}\right) \tag{2.5.8}$$

The magnetic field in each layer contains the same constant as in the electric field components.

Using Tikhonov-Cagniard approach (Zhdanov and Keller, 1994) to write the wave impedance as:

$$Z_{xy}\, = E_x(z)/H_y(z) \tag{2.5.9}$$

$$Z_{yx}\, = E_y(z)/H_x(z) \tag{2.5.10}$$

Substituting Equations 2.5.1 and 2.5.8 into Equation 2.5.9, we have:

$$Z_{xy}(z) = \frac{\omega\mu_0}{k_j}\frac{\left(A_{xj}e^{ik_jZ} + B_{xj}e^{-ik_jZ}\right)}{\left(A_{xj}e^{ik_jZ} - B_{xj}e^{-ik_jZ}\right)}$$

The impedance expression is valid only within the jth layer. This expression can be made more readable if numerator and denominator are divided by the factor $\left(A_{xj}B_{xj}\right)^{1/2}$.

$$Z_{xy}(z) = \frac{\omega\mu_0}{k_j}\left[\frac{\left(A_{xj}/B_{xj}\right)^{1/2}e^{ik_jZ} + \left(B_{xj}/A_{xj}\right)^{1/2}e^{-ik_jZ}}{\left(A_{xj}/B_{xj}\right)^{1/2}e^{ik_jZ} - \left(B_{xj}/A_{xj}\right)^{1/2}e^{-ik_jZ}}\right]$$

If we introduce the notation:

$$q_j\, = -\,ln\left(A_{xj}/B_{xj}\right)^{1/2}$$

The impedance equation becomes:

$$Z_{xy}(z) = \frac{\omega\mu_0}{k_j}\left[\frac{e^{\left(ik_jZ-q_j\right)} + e^{-\left(ik_jZ-q_j\right)}}{e^{\left(ik_jZ-q_j\right)} - e^{-\left(ik_jZ-q_j\right)}}\right]$$

$$= \frac{\omega\mu_0}{k_j}\,\coth(ik_jz - q_j\,) \tag{2.5.11}$$

For z$_{j-1}$ $\leq$ z $\leq$ z$_j$.

The two arbitrary constants A$_{xj}$ and B$_{xj}$ for each layer are reduced to a single constant, q$_j$. The horizontal component of the electric and magnetic fields are continuous across the boundaries between layers. Therefore, the wave impedance is also continuous across the surfaces between layers, thus:

$$Z_{xy}(z_{j-1}) = Z_{xy}(z_j - d_j) \tag{2.5.12}$$

From Equation 2.5.11, we have for the j th layer:

$$\frac{\omega\mu_0}{k_j}\,\coth(ik_jz_j - q_j\,) = Z_{xy}(z_j) \tag{2.5.13}$$

or,

$$q_j = ik_jz_j - \coth^{-1}\left[\frac{k_j}{\omega\mu_0}Z_{xy}(z_j)\right] \tag{2.5.14}$$

Substituting q$_j$ into Equation 2.5.11 at z= $z_j - d_j$= z$_{j-1}$, we have:

$$Z_{xy}(z_{j-1}) = Z_{xy}(z_j - d_j) = \frac{\omega\mu_0}{k_j}\coth\{ik_j(z_j - d_j) - q_j\}$$

$$= -\frac{\omega\mu_0}{k_j}\coth\left\{ik_jd_j - \coth^{-1}\left(\frac{k_j}{\omega\mu_0}Z_{xy}(z_j)\right)\right\}$$

9

This equation comprises a recursive relationship tying the impedance from layer j+1 to the impedance in layer j. This recursive procedure can be used to expand the expression for wave impedance at the earth´s surface (where we can measure it physically) through any number of layers, removing the constant, q_j, one by one:

For j = 1,

$$Z_{xy}(0) = -\frac{\omega\mu_0}{k_1}\coth\left\{ik_1d_1 - \coth^{-1}\left(\frac{k_1}{\omega\mu_0}Z_{xy}(z_1)\right)\right\}$$

For j = 2,

$$Z_{xy}(z_1) = -\frac{\omega\mu_0}{k_2}\coth\left\{ik_2d_2 - \coth^{-1}\left(\frac{k_2}{\omega\mu_0}Z_{xy}(z_2)\right)\right\}$$

For j = N-2,

$$Z_{xy}(z_{N-3}) = -\frac{\omega\mu_0}{k_{N-2}}\coth\left\{ik_{N-2}d_{N-2} - \coth^{-1}\left(\frac{k_{N-2}}{\omega\mu_0}Z_{xy}(z_{N-2})\right)\right\}$$

For j = N-1,

$$Z_{xy}(z_{N-2}) = -\frac{\omega\mu_0}{k_{N-1}}\coth\left\{ik_{N-1}d_{N-1} - \coth^{-1}\left(\frac{k_{N-1}}{\omega\mu_0}Z_{xy}(z_{N-1})\right)\right\} \tag{2.5.15}$$

Where $Z_{xy}(0)$ is the impedance measured on the Earth´s surface over an N-layered medium, $Z_{xy}(z_1)$ is the impedance at the bottom of the first layer, etc.

At the bottom layer the constants A_x and A_y are zero, since **E** and **H** goes to zero as z goes to infinity. Therefore, for layer N we have:

$$E_x(z) = B_{xN}e^{ik_N Z} \tag{2.5.16}$$

$$H_y(z) = \frac{k_N}{\omega\mu_0}B_{xN}e^{ik_N Z} \tag{2.5.17}$$

For $z_{N-1} \leq z \leq \infty$.

Consequently, the impedances Z_{xy} and Z_{yx} in the layer with index N are:

$$Z_{xy}(z) = E_x(z)/H_y(z) = \omega\mu_0/k_N$$

$$Z_{yx}(z) = E_y(z)/H_x(z) = \omega\mu_0/k_N$$

For $z_{N-1} \leq z \leq \infty$.

In particular, at the last interface, $z = z_{N-1}$, we have:

$$Z_{xy}(z_{N-1}) = \omega\mu_0/k_N \tag{2.5.18}$$

Substituting Equation 2.5.18 into Equation 2.5.15, we finally arrive at an expression for the impedance at the surface of the earth:

$$Z_{xy}(0) = \frac{\omega\mu_0}{k_1}\coth\left\{-ik_1d_1 + \coth^{-1}\left[\frac{k_1}{k_2}\coth(-ik_2d_2 + \coth^{-1}(\frac{k_2}{k_3}\coth(-ik_3d_3 + \right.\right.$$
$$\left.\left. \cdot + \coth^{-1}\left(\frac{k_{N-2}}{k_{N-1}}\coth\left\{-ik_{N-1}d_{N-1}+\coth^{-1}\left(\frac{k_{N-1}}{k_N}\right)\right\}\right)\cdots\right]\right\}\right\}$$

2.6 MT transfer functions

Magnetotelluric transfer functions or magnetotelluric responses are functions that relate measured electromagnetic field components at a given frequencies. The magnetotelluric transfer functions depend on the electrical properties of the materials at a given frequency. Hence, they characterise the conductivity distribution of the underlying materials according to the measured frequency.

The magnetotelluric transfer functions consist of the Impedance Tensors and Geomagnetic Transfer functions.

2.6.1 Impedance tensor and its rotation

The impedance tensor describes the relation between the electric and magnetic fields. In matrix form this is given by:

$$\begin{pmatrix} E_x \\ E_y \end{pmatrix} = \begin{pmatrix} Z_{xx} & Z_{xy} \\ Z_{yx} & Z_{yy} \end{pmatrix} \begin{pmatrix} H_x \\ H_y \end{pmatrix}$$

Or the electric and magnetic field spectra are linearly related as:

$$E_x(\omega) = Z_{xx}(\omega)H_x(\omega) + Z_{xy}(\omega)H_y(\omega) \qquad (2.6.1.1a)$$

$$E_y(\omega) = Z_{yx}(\omega)H_x(\omega) + Z_{yy}(\omega)H_y(\omega) \qquad (2.6.1.1b)$$

$$\vec{E} = \hat{Z}\vec{H} \text{ or } \vec{H} = \hat{Z}^{-1}\vec{E} = \hat{Y}\vec{E}$$

Where Zxy, Zyx are the principal impedances while Zxx, Zyy are the supplementary ones (contributions from parallel components of the magnetic field), $\hat{Y}$ is admittance which is the inverse of the impedance tensor $\hat{Z}$.
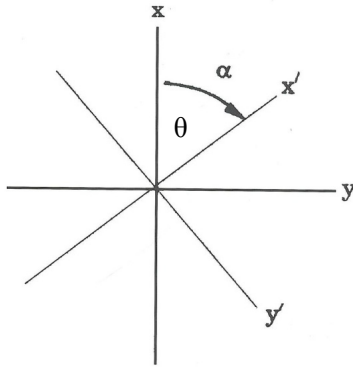
FIGURE 5: Impedance tensor rotation reference frame

The elements of the impedance tensor are in general dependent on the measurement directions x and y. Consider Figure 5, the impedance can be rotated through an angle θ from the x-direction (north) to a new coordinate system according to:

$$Z'(\omega) = R(\theta)Z(\omega)R(\theta)^T = RZR^T \qquad (2.6.1.2)$$

Where $R(\theta) = \begin{bmatrix} \cos\theta & \sin\theta \\ -\sin\theta & \cos\theta \end{bmatrix}$ is the rotation operator and R^T is the transpose of R:

$$R^T(\theta) = \begin{bmatrix} \cos\theta & -\sin\theta \\ \sin\theta & \cos\theta \end{bmatrix}$$

$$E' = RZR^T H'$$

$$E' = Z'H' \qquad (2.6.1.3)$$

and the elements are:

$$Z'_{xx} = Z_{xx}\cos^2\theta + (Z_{xy} + Z_{yx})\sin\theta\cos\theta + Z_{yy}\sin^2\theta \qquad (2.6.1.4a)$$

$$Z'_{xy} = Z_{xy}\cos^2\theta + (Z_{yy} - Z_{xx})\sin\theta\cos\theta - Z_{yx}\sin^2\theta \qquad (2.6.1.4b)$$

$$Z'_{yx} = Z_{yx}\cos^2\theta + (Z_{yy} - Z_{xx})\sin\theta\cos\theta - Z_{xy}\sin^2\theta \qquad (2.6.1.4c)$$

$$Z'_{yy} = Z_{yy}\cos^2\theta - (Z_{xy} + Z_{yx})\sin\theta\cos\theta + Z_{xx}\sin^2\theta \qquad (2.6.1.4d)$$

In one dimensional isotropic model (Cagniard, 1953).

$$Z_{xx} = Z_{yy} = 0, \qquad Z_{xy} = -Z_{yx}$$

Under this condition, Equation 2.6.1.4 a, b, c, d reduces to:

$$Z'_{xx} = Z'_{yy} = 0 \quad Z'_{xy} = Z_{xy}$$

and,

$$Z'_{yx} = Z_{yx}$$

Thus, the 1D impedance tensor is independent of the measurement axis.

From the above rotated forms of the impedance tensor (Equations 2.6.1.4a-2.6.1.4d), we can say that several combination of impedance tensors are rotationally invariant, that is, they have the same value whatever the angle of rotation is.

Consider the sum of the diagonal elements, $S_1 = Z_{xx} + Z_{yy}$. From Equations 2.6.1.4a-2.6.1.4d:

$$S'_1 = Z'_{xx} + Z'_{yy} = Z_{xx}\cos^2\theta + (Z_{xy} + Z_{yx})\sin\theta\cos\theta + Z_{yy}\sin^2\theta$$

$$+Z_{yy}\cos^2\theta - (Z_{xy} + Z_{yx})\sin\theta\cos\theta + Z_{xx}\sin^2\theta$$

$$= Z_{xx}(\cos^2\theta + \sin^2\theta) + Z_{yy}(\cos^2\theta + \sin^2\theta)$$

$$= Z_{xx} + Z_{yy} = S_1$$

Thus S_1 is rotationally invariant. The difference of the off-diagonal elements $D_1 = Z_{xy} - Z_{yx}$ is also *rotationally invariant.* However $Z_{xx} - Z_{yy}$ and $Z_{xy} + Z_{yx}$ are not invariant.

$$Z'_{xx} - Z'_{yy} = (\cos^2\theta - \sin^2\theta)(Z_{xx} - Z_{yy}) + 2\sin\theta\cos\theta\,(Z_{xy} + Z_{yx})$$

$$= \cos2\theta(Z_{xx} - Z_{yy}) + \sin2\theta(Z_{xy} + Z_{yx})$$

and, similarly,

$$Z'_{xy} + Z'_{yx} = (\cos^2\theta - \sin^2\theta)(Z_{xy} + Z_{yx}) - 2\sin\theta\cos\theta\,(Z_{xx} - Z_{yy})$$

$$= \cos2\theta(Z_{xy} + Z_{yx}) - \sin2\theta(Z_{xx} - Z_{yy})$$

Therefore, S_1 and D_1 are functions of the coordinates of the observation site, the frequency, and the properties of the medium. They are not functions of the orientation of the sensor axes.

In practice, the angle, θ_0, which maximizes the off-diagonal elements Z'_{xy} and Z'_{yx} and minimizes diagonal elements Z'_{xx} and Z'_{yy}, are found between 0° and 90° and would show repetition in other quadrants. When this angle is determined, provided:

$$\left(|Z'_{xx}|^2 + |Z'_{yy}|^2\right) = minimum \tag{2.6.1.5}$$

Automatically implies that:

$$\left(|Z'_{xy}|^2 + |Z'_{yx}|^2\right) = maximum \tag{2.6.1.6}$$

This leads to the definition of two modes of apparent resistivities. For a purely two-dimensional Earth, these are expressed as:

$$\rho_{xy} = 0.2T|Z'_{xy}|^2 \quad , \quad \phi'_{xy} = \arctan\,(Im\,Z'_{xy}/Re\,Z'_{xy}) \tag{2.6.1.7a}$$

$$\rho_{yx} = 0.2T|Z'_{yx}|^2 \quad , \quad \phi'_{yx} = \arctan\,(Im\,Z'_{yx}/Re\,Z'_{yx}) \tag{2.6.1.7b}$$

It has now become a common practice to calculate the effective (determinant) impedance which is rotationally invariant (Ranganayaki, 1984) as a determinant of the impedance matrix in Equation 2.6.1.2.

$$Z_{det} = \left[Z_{xx} Z_{yy} - Z_{xy} Z_{yx} \right]^{1/2} \qquad (2.6.1.8)$$

$$\rho_{det} = \frac{1}{\mu\omega} \left| Z_{xx} Z_{yy} - Z_{xy} Z_{yx} \right| \qquad (2.6.1.9a)$$

and

$$\phi_{det} = phase\ of\ (Z_{xx} Z_{yy} - Z_{xy} Z_{yx}) \qquad (2.6.1.9b)$$

The dependence of the impedance tensor upon the direction of the coordinate axes x, y can be displayed by polar diagrams (Berdichevisky, 1968; Berdichevisky et al., 1989).

Impedance polar plots provide a measure for the MT data dimensionality. Polar Plots show the modulus of a component of the impedance tensor as a function of the rotation angle θ ($0 < \theta < 2\pi$) at different frequencies.

$$\left| Z'_{xy}(\theta) \right| = Z_{xy} cos^2\theta + \left(Z_{yy} - Z_{xx} \right) \sin\theta \cos\theta - Z_{yx} sin^2\theta$$

$$\left| Z'_{xx}(\theta) \right| = Z_{xx} cos^2\theta + \left(Z_{xy} + Z_{yx} \right) \sin\theta \cos\theta + Z_{yy} sin^2\theta$$

Analysis of the shape of polar plots provides information about the level of 3D distortions and /or noise that may occur within the data. In case of 1D resistivity structure, the principal impedance polar diagrams are circles, while the polar diagrams of diagonal impedances collapse to a point (minimal) (Figure 6). For 2D or 3D resistivity structures, the principal impedances elongate in a direction either parallel or perpendicular to the strike (Reddy et al., 1977). The 2D diagrams for principal impedances are ovals (peanut shape), while diagram of diagonal elements takes the form of a flower with for identical petals (Figure 6). The bisectors between these petals are oriented parallel and perpendicular to the strike directions. A similar behaviour for the polar impedance diagrams is observed in an axially symmetric 3D model. When 3D model is asymmetric, the regular form of the impedance polar diagrams is distorted. Z_{xx} and Z_{xy} can be similar and look like figure-eight (Figure 6).
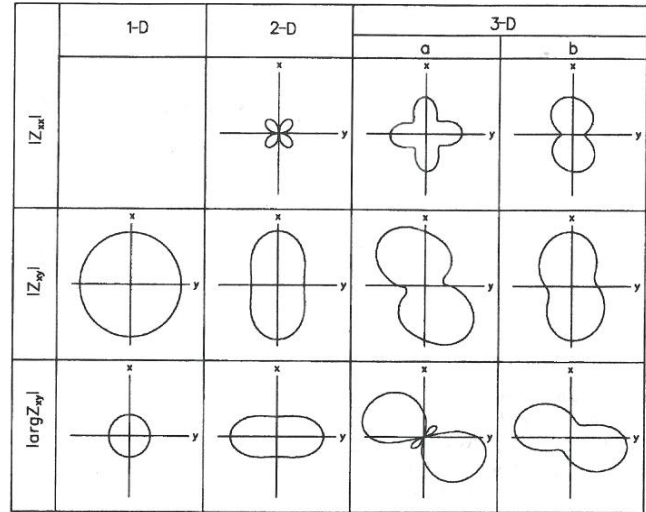
FIGURE 6: Polar diagrams of the impedance tensor (taken from Berdichevsky and Dmitriev, 2002)

*Skew i*s the ratio of the amplitudes of the diagonal impedance elements to the off-diagonal impedance elements. Skew is another measure of 3D dimensionality. It does not change with rotation of the coordinates.

$$skew = \left| \frac{Z_{xx} + Z_{yy}}{Z_{xy} - Z_{yx}} \right|$$

In 1D and 2D cases, the skew should be zero. Large deviations from zero were taken in the past as indicators of three-dimensionality. Typically, values below 0.2 were taken to indicate that the responses could be interpreted in a 1D or 2D manner (Simpson and Bahr, 2005; Berdichevsky and Dmitriev, 2002).

Another parameter which is often used as a 3-D indicator is the *ellipticity* of the rotation ellipses. The ellipticity is the ratio of the minor to the major axis of the ellipse in the principal direction given by:

$$\beta = \left| \frac{Z'_{xx}(\theta_0) - Z'_{yy}(\theta_0)}{Z'_{xy}(\theta_0) + Z'_{yx}(\theta_0)} \right|$$

where θ_0 is the angle obtained when Equation 2.6.1.5 and 2.6.1.6 are satisfied.

This is zero (for noise-free data) in the 1D case, and in the 2D case when the x or y axis is along the geoelectric strike direction.

2.6.2 Geomagnetic Transfer functions

The geomagnetic transfer function (Tipper) $\mathcal{T}$ is a complex vector showing the relationship between the horizontal and the vertical field, i.e.

$$H_z(\omega) = \mathcal{T}_{zx}H_x(\omega) + \mathcal{T}_{zy}H_y(\omega) \tag{2.6.2.1}$$

For a homogeneous 1D Earth, there is no induced vertical magnetic field H_z, and hence the transfer functions $(\mathcal{T}_{zx}, \mathcal{T}_{zy})$ are zero. By contrast, close to a boundary between low- and high-conductivity structures (for example, at the boundary between ocean and land), there is H_z field.

Parkinson inductions arrows are graphical representation of the transfer function components $\mathcal{T}_{zx}$ and $\mathcal{T}_{zy}$ (Parkinson, 1962). In the *Parkinson convention*, the vectors point *towards* lateral increase in electrical conductivity (Parkinson, 1959). Parkinson arrows have a real (in-phase) and quadrature (out-of-phase) part. Length of the real (M_r) and quadrature (M_q) arrows are given by:

$$M_r = (\Re\mathcal{T}_{zx}{}^2 + \Re\mathcal{T}_{zy}{}^2)^{1/2} \tag{2.6.2.2}$$

$$M_q = (\Im\mathcal{T}_{zx}{}^2 + \Im\mathcal{T}_{zy}{}^2)^{1/2} \tag{2.6.2.3}$$

Orientation of the arrows is similarly determined by:

$$\theta_r = \tan^{-1}\left(\frac{\Re\mathcal{T}_{zy}}{\Re\mathcal{T}_{zx}}\right) \tag{2.6.2.4}$$

$$\theta_q = \tan^{-1}\left(\frac{\Im\mathcal{T}_{zy}}{\Im\mathcal{T}_{zx}}\right) \tag{2.6.2.5}$$

In Equations 2.6.2.4 and 2.6.2.5 above, θ_r and θ_q are clockwise positive from x-direction (usually geomagnetic north).

2.7 Dimensionality in MT

2.7.1 1D MT theory

1D resistivity models are models where the resistivity varies with depth only, i.e. $\rho = \rho(z)$. A layered model is an example of 1D model.

For a 1D earth, the diagonal elements of the impedance tensor, Z_{xx} and Z_{yy} are zero, whilst the off-diagonal components are equal in magnitude, but have opposite signs, independent of rotation, i.e.

$$Z_{1D} = \begin{pmatrix} 0 & Z_{xy} \\ -Z_{xy} & 0 \end{pmatrix} \tag{2.7.1.1}$$

This shows that the two estimates of the apparent resistivity curves are identical, and the phases difference between Z_{xy} and Z_{yx} is exactly 180° apart. The xy phase should lie in the first quadrant (0°-90°), and the yx phase should lie in the third quadrant ((-90°) - (-180°)).

Following the field equations for the propagation in a uniform space, Equation 2.4.23 and 2.4.24, we can see that for a uniform half space the (complex-valued) impedance within the medium is given by:

$$Z_{xy}(\omega) = \frac{E_x(\omega)}{H_y(\omega)} = \frac{\omega\mu_o}{k} \tag{2.7.1.2}$$

Taking the absolute square gives:

$$\left|\frac{E_x(\omega)}{H_y(\omega)}\right|^2 = \left|\frac{\omega\mu_o}{k}\right|^2 = \frac{\omega\mu_o}{\sigma} \tag{2.7.1.3}$$

$$\frac{1}{\sigma} = \frac{1}{\omega\mu_o}\left|\frac{E_x(\omega)}{H_y(\omega)}\right|^2 = \rho$$

which is the true resistivity of the half space as a function of frequency.

In the quasi stationary approximation $= \sqrt{\omega\mu_o\sigma}\frac{1}{\sqrt{2}}(1 + i)$, we have:

$$Z = \sqrt{\frac{\omega\mu_o}{\sigma}}\frac{\sqrt{2}}{1+i} = \sqrt{\frac{\omega\mu_o}{\sigma}}\frac{1-i}{\sqrt{2}} = \sqrt{\frac{\omega\mu_o}{\sigma}}e^{i\pi/4} \tag{2.7.1.4}$$

In Equation 2.7.1.4, $\pi/4 = 45°$ is the phase difference between E_x and H_y with E_x leading H_y. For non-homogenous earth, the apparent resistivity, ρ_a (Ωm) is defined by:

$$\rho_a = \frac{1}{\mu_0\omega}|Z|^2$$

Similarly, the phase of the complex impedance tensor is defined by:

$$\phi = tan^{-1}\left(\frac{Im\ Z}{Re\ Z}\right)$$

The depth to which EM waves penetrate into a uniform ground of resistivity ρ is characterized by the skin depth (δ). *Skin depth* is defined as the depth where the electromagnetic field has reduced to e^{-1} of its original real value at the surface:

$$\delta(\omega) = \frac{1}{Real(k)} = \frac{1}{Real(\sqrt{(i\omega\mu_o\sigma)})} = \sqrt{\frac{2}{\omega\mu\sigma}} \tag{2.7.1.5}$$

which reduces to:

$$\delta(T) \approx 500\sqrt{\rho T} \qquad \text{(in metres)}$$

T is the period (in s). Theoretically penetration to all depths is assured - one merely needs to measure longer and longer period to probe deeper and deeper into the Earth.

Apparent resistivity and impedance phase are usually plotted as a function of period, $T = 2\pi/\omega$. The functions $\rho_a(T)$ and $\phi(T)$ are not independent of each other, but are linked via the following Kramers-Kroenig relationship (Weidelt, 1972):

$$\phi(\omega) = \frac{\pi}{4} - \frac{\omega}{\pi}\int_0^\infty log\left(\frac{\rho_a(\omega')}{\rho_0}\right)\frac{d\omega'}{\omega'^2-\omega^2} \tag{2.7.1.6}$$

Equation 2.7.1.6 states that the function $\rho_a(T)$ can be predicted from the function $\phi(T)$ except for a scaling coefficient, ρ_o. Equation 2.7.1.6 illustrates that the phase for a frequency ω is dependent on the apparent resistivity for all frequencies ω', with the influence of $\rho_a(\omega')$ largest for $\omega' = \omega$ due to the scaling term $\frac{1}{\omega'^2-\omega^2}$. Therefore, the phase anticipates the behaviour of the apparent resistivity with period; but it cannot determine its absolute position.

2.7.2 2D earth MT theory

In a 2D earth the conductivity is constant in one horizontal direction while changing both in the vertical and other horizontal direction. The direction along which the conductivity is constant is called the geoelectric strike or electromagnetic strike.

For a 2D Earth, Z_{xx} and Z_{yy} are equal in magnitude, but have opposite sign, whilst Z_{xy} and Z_{yx} differ. Two independent modes of the impedance are analyzed for 2D earth analysis in Cartesian coordinate system with x parallel to strike and y perpendicular to strike. Transverse electric (TE) mode (**E**-polarization) is when the electric field is parallel to strike. Transverse magnetic (TM) mode (**B**-polarization) is when the magnetic field is parallel to strike. Diagonal elements of the impedance tensor for a perfectly 2D earth are zero:

$$Z_{2D} = \begin{bmatrix} 0 & Z_{xy} \\ Z_{yx} & 0 \end{bmatrix} \tag{2.7.2.1}$$

where:

$$Z_{xy}(\omega) = Z_{TE} = \frac{E_x(\omega)}{H_y(\omega)}$$

$$Z_{yx}(\omega) = Z_{TM} = \frac{E_y(\omega)}{H_x(\omega)}$$

Figure 7 shows a very simple two-dimensional (2D) model with a vertical contact between two zones of different conductivity, σ_1 and σ_2 striking in the y-direction. The resistivity boundary may represent a geological fault or a dyke.

The physical principle governing induction at the discontinuity is conservation of current. Since electric current must be conserved across the boundary, the change in conductivity demands that the electric field, E_y, must also be discontinuous. All other components of the electromagnetic field are continuous across the boundary. Ohm´s Law can be used to connect the current density to the electric field across the boundary. For the y-component of the current density:
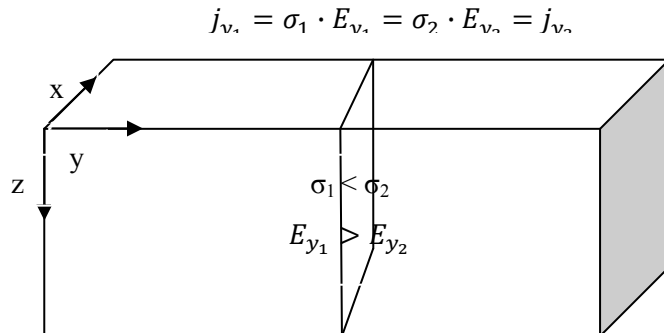
FIGURE 7: 2D resistivity model at lateral contact striking in the x-direction. The resistivity boundary separates two regions of differing conductivity ($\sigma1 < \sigma2$). The electric field Ey is discontinuous across the resistivity boundary

$$j_{y_1} = \sigma_1 \cdot E_{y_1} = \sigma_2 \cdot E_{y_2} = j_{y_2} = constant \tag{2.7.2.2}$$

The discontinuity in the conductivities causes a jump in the electric field normal to the boundary (E_y component on Figure 7).

For a body with infinite length along strike direction, or one with a strike length is significantly longer than the skin depth (penetration depth) (Equation 2.7.1.5), there are no field variations parallel to the strike ($\frac{\delta}{\delta x} = 0$). Furthermore, the EM fields are orthogonal and can be decoupled into TE and TM mode (Figure 7).

The TE mode can be described in terms of electromagnetic field components E_x, B_y, and B_z from Equation 2.3.1 as:

$$\left.\begin{array}{l} \frac{\partial E_x}{\partial y} = \frac{\partial B_z}{\partial t} = -i\omega B_z \\[6pt] \frac{\partial E_x}{\partial z} = \frac{\partial B_y}{\partial t} = i\omega B_y \\[6pt] \frac{\partial B_z}{\partial y} - \frac{\partial B_y}{\partial z} = \mu\sigma E_x \end{array}\right\} \quad \textbf{E}\text{-polarization} \qquad (2.7.2.3)$$

There is no discontinuous behaviour for TE mode as E_y component doesn't exist in this mode.

The TM mode can be described in terms of the electromagnetic field B_x, E_y and E_z :

$$\left.\begin{array}{l} \frac{\partial B_x}{\partial y} = \mu\sigma E_z \\[6pt] -\frac{\partial B_x}{\partial z} = \mu\sigma E_y \\[6pt] \frac{\partial E_z}{\partial y} - \frac{\partial E_y}{\partial z} = i\omega B_x \end{array}\right\} \quad \textbf{B}\text{-polarization} \qquad (2.7.2.4)$$

At the air-ground boundary, $E_z = 0$. Since E_y is discontinuous across a vertical contact, the impedances- Z_{yx} and Z_{yy} associated with E_y are also discontinuous. From Equation 2.7.2.2 above, discontinuity in the electric field (and also for Z_{yx}) is σ_2/σ_1 for TM mode across the boundary. Therefore, there will be a discontinuity in ρ_{yx} of magnitude $(\sigma_2/\sigma_1)^2$. Thus, TM mode resolves the lateral resistivity boundary due to discontinuity in ρ_a. However, the resistivities close to the boundary are estimated low for conductive and too high for more resistive region. The TE mode is continuous regarding the ρ_a estimates.

As a consequence of the discontinuous behaviour exhibited by ρ_{yx}, TM mode resistivities tend to resolve lateral conductivity variations better than the TE resistivites. However, TE mode has an associated vertical magnetic field (Equation 2.7.2.3). Vertical magnetic fields are generated by lateral conductivity gradients and boundaries, and spatial variations of the ratio H_z/H_y can be used to diagnose lateral conductivity contrasts from TE mode.

The TM mode contains no vertical magnetic field components, but does contain a vertical electric field within the Earth. In the TM mode, electric current cross the boundaries between regions of differing resistivity. This causes building up of electric charges develop on the boundaries. Thus physics of this mode includes both inductive and galvanic effects. Galvanic effects, such as charge build up on boundaries; will be observed at all frequencies (including direct currents).

2.7.3 3D MT theory

The 3D resistivity models are the general type of geoelectric structure. Here, the conductivity changes along all directions ($\sigma = \sigma(x,y,z)$). .

MT transfer functions take the general forms with all non-zero components (Equations 2.6.1.2 and 2.6.2.1). There is no any rotation direction through which the diagonal components of the magnetotelluric tensor or any component of the tipper vector can vanish.

2.8 The galvanic distortion phenomenon

Distortion in MT is a phenomenon produced by the presence of shallow and local bodies or heterogeneities, which are much smaller than the targets of interest and skin depths. These bodies cause charge distributions and induced currents that alter the magnetotelluric responses at the studied or regional scale (Kaufman, 1988; Chave and Smith, 1994). In the case that these bodies are of the similar scale as the depth of interest, they can be modelled in a 3D environment.

Distortion can be inductive or galvanic. Inductive distortions are generated by current distributions that have a small magnitude and decay with period. Under the condition $\sigma \gg \omega\varepsilon$ (quasi-stationary approximation) they can be ignored (Berdichevsky and Dmitriev, 1976).

Galvanic distortion is caused by charge distributions accumulated on the surface of shallow bodies, which produce anomalous electromagnetic field. This anomalous magnetic field is small, whereas the anomalous electric field is of the same order of magnitude as its regional counterpart and is frequency independent (Bahr, 1988; Jiracek,1990). Hence the galvanic distortion is treated as the existence of an anomalous electric field, $\mathbf{E}_a$.

There are different methods to correct galvanic distortion over one dimensional and two dimensional structures (Zhang et al., 1987; Bahr, 1988; Groom and Bailey, 1989 and Smith, 1995). In the method proposed by Groom and Bailey (1989) the distortion is described by the contribution of four tensors, represented by the gain (g) parameter, the twist (T), shear (S) and anisotropy (A). The gain (g) and anisotropy (A) accounts for the static shift parameter in Groom and Bailey decomposition.

In the case of a 1D Earth, galvanic distortion produces a constant displacement of apparent resistivity along all frequencies (Pellerin and Hohmann, 1990). This is known as *Static shift,* and does not affect the phase. A static shift also occurs in a 2D Earth. There is no general analytical or numerical way to model the cause of static shift and thus correct it by using MT itself. Electromagnetic methods which only measure magnetic fields such as TEM do not have the static shift problems that affect MT soundings (Simpson and Bahr, 2005). Therefore, TEM data can be used in conjunction with MT data from the same site in order to correct for static shifts (Sternberg et al., 1988; Pellerin and Hohmann, 1990; Árnason, 2008).

3. INSTRUMENTATION, FIELD PROCEDURE AND DATA PROCESSING

3.1 Instrumentation and field procedure

The equipment for MT data acquisition consists of magnetic and electric field sensors and a data logger that controls and performs the data acquisition process and the data storage. A typical field setup of MT measurement is shown in Figure 8. The electric and magnetic sensors measure the horizontal electric and magnetic field components. Commonly, there are five channels for a typical MT data acquisition system. These are two electric field channels (E_x and E_y) and three magnetic field channels (H_x, H_y, and H_z).
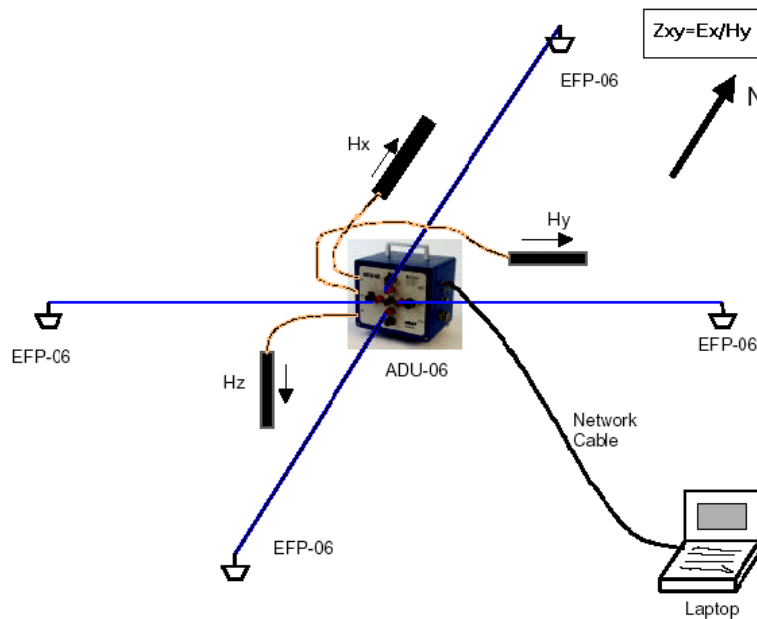
FIGURE 8: A typical 5-channel MT field setup
(taken from ADU-06's Manual)

The electric field components (E_x and E_y) are determined by measuring the potential difference, ΔV, between pairs of electrodes, which are connected via a shielded cable to form a dipole and buried in the ground at known distance, d, which gives $E = \Delta V/d$. In the field setup, one electric dipole is oriented in the magnetic N-S direction, and the other in the magnetic E-W direction (Figure 8). Non-polarisable electrodes usually consist of a porous pot containing a metal in contact with a solution, which gives contact to the ground through a porous material usually PbCl or $CuSO_4$.

The most commonly used magnetic sensors in MT studies are induction coils. A set of three induction coils plus a spirit level and a compass for aligning their axes are required in order to measure all three components of the time varying magnetic field (H_x, H_y, and H_z).

The data logger is the central control unit of the MT measuring system. It controls the acquisition process and amplifies the sensor signals and converts these data into digital format through an A/D converter.

3.2 Time series processing

MT data processing transforms the time varying geoelectric field components into Earth response functions which contain information on the distribution of the conductivity structure.

Commonly time series processing involves three main steps:

1. Data setup and preconditioning:
2. Time to frequency domain conversion; and
3. Estimation of the MT transfer functions

3.2.1 Data setup and preconditioning

The recorded time series are divided into M segments containing N data points each. The value of N is chosen depending on the recorded time window such that each segment contains evaluation periods

equally spaced on a logarithmic scale. In addition, each time window must be divided into a sufficient number of segments for further statistical estimation of the transfer functions.

Once the segments have been defined, they are inspected in order to identify and remove trends and noise effects. This is performed manually and/or automatically using specific software.

3.2.2 Time to frequency domain conversion

For each segment, the measured channels E_i (i =x, y) and H_j (j= x, y, z) are converted from time to frequency domain using the Discrete Fourier Transform (Brigham, 1974) or Cascade Decimation (Wight and Bostick, 1980). Conversion from time to frequency domain is usually done by FFT because of its speed. A raw spectrum with N/2 frequencies is obtained. From these, evaluation frequencies, equally distributed in a log scale, optimally 6-10 per period decade, are chosen. The final spectra are smoothed by averaging over neighbouring frequencies using a parzen window function.

Each field component must be calibrated according to the instrument sensitivity at a given frequency. The auto and cross spectra of segment K, which are products of the field components and their complex conjugates, are then obtained for each frequency: $\langle E_{Kj}(\omega) \cdot E_{Kj}^*(\omega)\rangle$, $\langle H_{Kj}(\omega) \cdot H_{Kj}^*(\omega)\rangle$, $\langle E_{Kj}(\omega) \cdot H_{Kj}^*(\omega)\rangle$ and $\langle H_{Kj}(\omega) \cdot E_{Kj}^*(\omega)\rangle$. These are stored in the spectral matrix, which contains the contribution from all the segments at a specific frequency.

An estimate of the auto-spectral density, or spectrum, of channel A around frequency f_j in the band (f_{j-m}, f_{j+m}) is given by:

$$\langle A(f_j)\rangle = \sqrt{\frac{1}{2m+1} \sum_{k=j-m}^{j+m} A_k A_k^*} = \langle A_j A_j^*\rangle^{1/2}$$

where A is **E** or **H**. The square of this is the autopower spectral density at f_j. In the same way the crosspower density at f_j of two channels , A and B, is given by:

$$\langle A(f_j) \cdot B(f_j)\rangle = \frac{1}{2m+1} \sum_{k=j-m}^{j+m} A_k B_k^* = \langle A_j B_j^*\rangle$$

3.2.3 Estimation of the MT transfer functions

The evaluation of MT transfer functions need averaging of spectra over a number of closely spaced frequencies of the corresponding field components in the frequency domain, which can be obtained from two segments which are given in Equations 2.6.1.1a, b and 2.6.2.1:

$$E_x(\omega) = Z_{xx}H_x(\omega) + Z_{xy}H_y(\omega)$$

$$E_y(\omega) = Z_{yx}H_x(\omega) + Z_{yy}H_y(\omega)$$

$$H_z(\omega) = \mathcal{T}_{zx}H_x(\omega) + \mathcal{T}_{zy}H_y(\omega)$$

The conventional way of solving the impedance equations assumes Z_{ij} are constant over an averaging band (window), which is physically reasonable if the bands are narrow enough. In each band, each equation has crosspower taken with H_x and H_y in turn, giving pairs of equations:

$$\langle E_x H_x^*\rangle = Z_{xx}\langle H_x H_x^*\rangle + Z_{xy}\langle H_y H_x^*\rangle$$

$$\langle E_y H_y^*\rangle = Z_{yx}\langle H_x H_y^*\rangle + Z_{yy}\langle H_y H_y^*\rangle$$

where $H_x^*(\omega)$ and $H_y^*(\omega)$ are conjugates of horizontal magnetic field.

In the same way, tipper crosspower of H_z are taken with H_x and H_y to give two equations:

$$\langle H_z H_x^* \rangle = \mathcal{T}_{zx} \langle H_x H_x^* \rangle + \mathcal{T}_{zy} \langle H_y H_x^* \rangle$$

$$\langle H_z H_y^* \rangle = \mathcal{T}_{zx} \langle H_x H_y^* \rangle + \mathcal{T}_{zy} \langle H_y H_y^* \rangle$$

Solving the pairs of simultaneous equations for impedance and tipper allows obtaining six independent estimates of the transfer functions (Vozoff, 1972).

$$Z_{xx} = \frac{\langle E_x H_x^* \rangle \langle H_y H_y^* \rangle - \langle E_x H_y^* \rangle \langle H_y H_x^* \rangle}{\langle H_x H_x^* \rangle \langle H_y H_y^* \rangle - \langle H_x H_y^* \rangle \langle H_y H_x^* \rangle}$$

$$Z_{xy} = \frac{\langle E_x H_x^* \rangle \langle H_x H_y^* \rangle - \langle E_x H_y^* \rangle \langle H_x H_x^* \rangle}{\langle H_y H_x^* \rangle \langle H_x H_y^* \rangle - \langle H_y H_y^* \rangle \langle H_x H_x^* \rangle}$$

$$Z_{yx} = \frac{\langle E_y H_x^* \rangle \langle H_y H_y^* \rangle - \langle E_y H_y^* \rangle \langle H_y H_x^* \rangle}{\langle H_x H_x^* \rangle \langle H_y H_y^* \rangle - \langle H_x H_y^* \rangle \langle H_y H_x^* \rangle}$$

$$Z_{yy} = \frac{\langle E_y H_x^* \rangle \langle H_x H_y^* \rangle - \langle E_y H_y^* \rangle \langle H_x H_x^* \rangle}{\langle H_y H_x^* \rangle \langle H_x H_y^* \rangle - \langle H_y H_y^* \rangle \langle H_x H_x^* \rangle}$$

$$\mathcal{T}_{zx} = \frac{\langle H_z H_x^* \rangle \langle H_y H_y^* \rangle - \langle H_y H_x^* \rangle \langle H_z H_y^* \rangle}{\langle H_x H_x^* \rangle \langle H_y H_y^* \rangle - \langle H_y H_x^* \rangle \langle H_x H_y^* \rangle}$$

$$\mathcal{T}_{zy} = \frac{\langle H_z H_y^* \rangle \langle H_x H_x^* \rangle - \langle H_z H_x^* \rangle \langle H_x H_y^* \rangle}{\langle H_x H_x^* \rangle \langle H_y H_y^* \rangle - \langle H_y H_x^* \rangle \langle H_x H_y^* \rangle}$$

Similar estimates of the transfer functions were done by variety of methods, for example Sims et al. (1971).

3.2.4 Remote-reference estimates

The remote reference method (Goubau et al., 1979; Gamble et al., 1979; Clarke et al., 1983) involves deploying additional sensors (usually magnetic) at a site remote from the main (local) measurement site. Whereas the uncontaminated (natural) part of the induced field can be expected to be coherent over spatial scales of many kilometres, noise is generally random and incoherent at two locations far away from each other (10-100 km). Therefore, by measuring selected electromagnetic components at both local and remote sites, bias effects arising from the presence of noise that is uncorrelated between sites can be removed. Correlated noise that is present in both local and remote sites cannot be removed by this method. The distance between local and remote sites in order to realise the assumption of uncorrelated noise depends on the noise source, intended frequency range of measurement and conductivity of the sounding medium. The noise can take the form of wind-induced noise, for which the remote needs to be some hundreds of metres away, to cultural disturbances, for which in extreme cases the remote has to be many tens to hundreds of kilometres away.

At either site (the local and remote), the electric and magnetic field spectrum are linearly related as given in Equation 2.6.1.1a, b. Multiplying these equations by the spectra $R_x^*(\omega)$ and $R_y^*(\omega)$ and average over a number of determinations.

$$\langle E_x R_x^* \rangle = Z_{xx} \langle H_x R_x^* \rangle + Z_{xy} \langle H_y R_x^* \rangle$$

$$\langle E_y R_y{}^* \rangle = Z_{yx}\langle H_x R_y{}^* \rangle + Z_{yy}\langle H_y R_y{}^* \rangle$$

$$\langle E_x R_y{}^* \rangle = Z_{xx}\langle H_x R_y{}^* \rangle + Z_{xy}\langle H_y R_y{}^* \rangle$$

$$\langle E_y R_x{}^* \rangle = Z_{yx}\langle H_x R_x{}^* \rangle + Z_{yy}\langle H_y R_x{}^* \rangle$$

These four equations can be solved for the four desired remote reference estimates of the impedance tensors elements Z_{ij} as given below:

$$Z_{xx} = \frac{\langle E_x R_x{}^* \rangle \langle H_y R_y{}^* \rangle - \langle E_x R_y{}^* \rangle \langle H_y R_x{}^* \rangle}{\langle H_x R_x{}^* \rangle \langle H_y R_y{}^* \rangle - \langle H_x R_y{}^* \rangle \langle H_y R_x{}^* \rangle}$$

$$Z_{xy} = \frac{\langle E_x R_x{}^* \rangle \langle H_x R_y{}^* \rangle - \langle E_x R_y{}^* \rangle \langle H_x R_x{}^* \rangle}{\langle H_y R_x{}^* \rangle \langle H_x R_y{}^* \rangle - \langle H_y R_y{}^* \rangle \langle H_x R_x{}^* \rangle}$$

$$Z_{yx} = \frac{\langle E_y R_x{}^* \rangle \langle H_y R_y{}^* \rangle - \langle E_y R_y{}^* \rangle \langle H_y R_x{}^* \rangle}{\langle H_x R_x{}^* \rangle \langle H_y R_y{}^* \rangle - \langle H_x R_y{}^* \rangle \langle H_y R_x{}^* \rangle}$$

$$Z_{yy} = \frac{\langle E_y R_x{}^* \rangle \langle H_x R_y{}^* \rangle - \langle E_y R_y{}^* \rangle \langle H_x R_x{}^* \rangle}{\langle H_y R_x{}^* \rangle \langle H_x R_y{}^* \rangle - \langle H_y R_y{}^* \rangle \langle H_x R_x{}^* \rangle}$$

where the remote fields are denoted by R_x and R_y.

As with single-station estimation, typically the magnetic field contains less noise than the electric fields, and thus the remote fields R_x and R_y used for the above equations are the remote magnetic fields.

4. 1D, 2D AND 3D MT INVERSION CODES USED

The aim of this chapter is to give a brief overview of the 1D, 2D and 3D MT inversion routines used in the thesis.

The MT method for imaging Crustal and Upper Mantle conductivity has found increasing use in both geophysical exploration and large scale tectonic studies. Initial application of MT was based on 1D interpretation for which many inversion codes are well developed and being used (see e.g. Jupp and Vozoff, 1975; Constable et al., 1987; Smith and Booker, 1988).

For various practical reasons, the programs TEMTD (Árnason, 2006), **RE**duced **B**asis **OCC**am (**REBOCC**) (Siripunvaraporn and Egbert, 2000), and WSINV3DMT (Siripunvaraporn et al., 2005), are used for 1D inversion, 2D inversion and 3D inversion of MT data, respectively.

4.1 1D inversion of MT data

The program TEMTD was used to perform 1D inversion of MT data. The program was written by Knútur Árnason of ÍSOR (Árnason, 2006). The program can do 1D inversion of TEM and MT data separately and jointly. The program can invert MT apparent resistivity and/or phase derived from either of the off-diagonal elements of the MT tensor (xy and yx modes), the rotationally invariant determinant or the average of the off-diagonal elements.

In the joint inversion, one additional parameter is inverted for (in addition to the layered model parameters), namely a static shift multiplier needed to fit both the TEM and MT data with the same model. The program can do both standard layered inversion (inverting for resistivity values and layer thicknesses) and Occam (minimum structure) inversion with exponentially increasing layer thicknesses with depth. It offers a user specified damping of first (sharp steps) and second order derivatives (oscillations) of model parameters (logarithm of resistivity and layer thicknesses).

4.2 2D inversion of MT data

For most MT data sets, 2D or 3D inversion is required. Over the past decade a substantial progress has been made on the development of 2D and 3D MT inversion methods. These have included straight forward extensions of linearized search methods developed previously for 1D regularized inversion (deGroot-Hedlin and Constable, 1990; Uchida, 1993), the subspace method (Oldenburg et al., 1993) and methods based on direct iterative minimization of a regularized penalty functional (Rodi and Mackie, 2001).

REBOCC (REduced Basis OCCam**)** is a code for 2D inversion of MT data. It is based on an efficient variant of the OCCAM algorithm of deGroot-Heldin and Constable (1990), (Siripunvaraporn and Egbert, 2000). The code can invert for apparent resistivity (ρ_a) and phase (ϕ) of TM and TE modes as well as real and imaginary parts of the vertical magnetic transfer function (tipper).

The reason why this inversion code is chosen for this processing work is because it is:

- Freely available for academic use
- Fast
- Stable
- Moderate memory requirement
- Easy to use

4.2.1 Overview of REBOCC

The inverse models are descretized into M constant resistivity blocks, m = [m_1, m_2. . ., m_M] and there are N observed data d =[d_1,d_2, ..., d_N] with uncertainties e =[e_1, e_2, ...,e_n]. The data misfit functional $X_d{}^2$ can be expressed as:

$$X_d{}^2 = (d - F[m])^T C_d{}^{-1}(d - F[m]) \qquad (4.2.1)$$

Where $F[m]$ denotes the model response, the superscript T represents matrix transpose and C_d is the data covariance matrix, which is diagonal and contains the data uncertainties.

The normalized root mean square (RMS) misfit of the data is defined as $^1/_N X_d{}^2$.

Because of the non-uniqueness of the inverse problem, an infinite number of models can produce the same misfit in Equation 4.2.1.

Most modern MT inversion schemes resolve non-uniqueness by seeking models that have minimum possible structure for a given level of misfit (Parker, 1994). Therefore, a model structure functional $X_m{}^2$ is introduced.

$$X_m{}^2 = (m - m_o)^T C_m{}^{-1}(m - m_o) \qquad (4.2.2)$$

Where m_o is a base (or prior) model, and C_m is a model covariance matrix, which characterizes the magnitude and smoothness of the resistivity variation with respect to the prior model m_o.

The minimum structure inverse problem is to minimize $X_m{}^2$ subject to $X_d{}^2 = X_*{}^2$, where $X_*{}^2$ is the desired level of misfit.

The two functionals are combined to yield the unconstrained functional U(m,λ) with $X_*{}^2$ the desired level of misfit:

$$U(m,\lambda) = X_m{}^2 + \lambda^{-1}\left(X_d{}^2 - X_*{}^2\right) \rightarrow minimum \qquad (4.2.3)$$

In Equation 4.2.3 the Lagrange multiplier λ acts to "trade off" between minimizing the norm of data misfit and the norm of the model (Tikhonov and Arsenin, 1977; and Parker, 1994).

When λ is large, the data misfit becomes less important and more weight is given toward producing a smoother model. In contrast, as λ goes to zero, the inverse problem becomes closer to the ill conditioned least square problem, resulting in an erratic model (Parker, 1980). In order to minimize Equation 4.2.3, the stationary points have to be found with respect to m and λ. Instead of using Equation 4.2.3, the penalty functional $W_\lambda(m)$ is differentiated with respect to m.

$$W_\lambda(m) = X_m{}^2 + \lambda^{-1} X_d{}^2 \rightarrow minimum \qquad (4.2.4)$$

For a constant value of λ, the stationary points U(m,λ) and $W_\lambda(m)$ are the same. The stationary points of Equation 4.2.3 can be found by minimizing Equation 4.2.4 for a series of λ values and then choosing λ so that the misfit satisfies the constraint $X_d{}^2 = X_*{}^2$.

Instead of solving the minimization problem in the model space, REBOCC code transforms the problem into the data space, by expressing the solution as a linear combination of "representers" (i.e. rows of the sensitivity matrix smoothed by the model covariance). This transformation reduces the size of the system of equations to be solved from M x M to N x N (where M is the number of model parameters and N is number of data parameters). Since the number of model parameters M is often much larger than the number of data parameters N, this approach reduces the CPU time and memory requirement significantly. In general, MT data are smooth in period and for closely spaced sites in space. This causes data redundancy. Therefore, in the data space approach, there is no need to use all representers. A subset of this basis function (of dimension L) is sufficient to construct the model

without significantly loss of detail. Hence, the size of the system of equations to be solved further reduces to L x L (where L << N and M).

Even though the construction of the solution is made from the subset of the smoothed sensitivities, the goal of the inversion remains to find the norm minimizing model subject to fitting all of the data well enough.

Because the aim is searching for the minimum norm model, the REBOCC inversion can be divided into two stages: Phase I for bringing down the misfit to the desired level X_*^2, and Phase II for searching for the model with minimum norm while keeping the misfit at the desired level (or smoothing process). Phase II is necessary in order to wipe out the spurious features occurring while the program tries to reduce the misfit.

Since the MT inverse problem is non-linear, the desired misfit may never be reached and phase II will never be executed. It is better to restart the inversion process with a higher desired misfit, and a model from the previous run as a starting model.

4.2.2 Forward modelling

The forward modelling is of central importance in any inversion method and hence must be fast, accurate and reliable. The REBOCC inversion uses forward modelling to compute the sensitivity matrix, and responses for calculating the misfit. To obtain MT responses at the surface, one must solve for the electric (**E**) and magnetic (**H**) fields simultaneously via solving the second order Maxwell's Equations. Memory requirements can be significantly reduced by solving the second order equations (Siripunvaraporn et al., 2002).

For the transverse electric (TE) mode, i.e. the electric currents flow parallel to the strike of the structure:
$$\nabla \times \nabla \times \boldsymbol{E} = i\omega\mu\sigma E \qquad (4.2.5)$$
(Time dependence $e^{-i\omega t}$ is assumed)

And for the transverse magnetic (TM) mode, i.e. the electric currents flow perpendicular to the strike.

$$\nabla \times \nabla \times \boldsymbol{H} = i\omega\sigma\mu\boldsymbol{H} \qquad (4.2.6)$$

where **E** and **H** are electric and magnetic fields, σ is the conductivity, μ is magnetic permeability for free space and ω is the angular frequency (see also section 2.4).

In REBOCC, a finite difference (FD) method with the TE and TM mode differential equations as discretized in Smith and Booker (1991) is used. The discrete form of the differential equations can be expressed as **Ax = b,** where **b** contains the terms associated with the known boundary values and the source fields, and **x** represents the unknown fields (**E** for TE and **H** for TM mode).

The matrix **A** is sparse (5 non-zero diagonals) and symmetric. The accuracy of the solution is controlled by the quality of the grid mesh.

4.2.3 Input files requirement for REBOCC

The input information for the REBOCC inversion code is divided into three mandatory input files and four optional files. The mandatory files are: startup file, data file(s) and starting model file.

The Startup file defines all parameters used for the inversion. The data file contains the data, i.e, ρ_a and φ of the TE and TM mode, or real $\mathcal{R}$ and imaginary $\mathfrak{I}$ part of Tipper, used for inversion. The starting model file defines the model grid size and the initial resistivity value of each model block.
The optional files include sensitivity inclusion matrix file(s), distortion file (s), prior model file and model control file. In REBOCC flat surface of the earth is assumed.

For a detailed description of each of the above files refer to the user manual by Siripunvaraporn and Egbert (1999).

4.2.4 Model grid design

The accuracy of the numerical solution to the 2D problem depends strongly on the level of discretization (Muller and Loseche, 1975). A properly discretized mesh is important to ensure accurate results. In designing the model grids the following general rules were applied, whenever possible (see Mackie, 2002). However, wider inter-station gaps and uneven distribution of MT sites, sometimes, impedes strict applications of these rules.

4.2.5 Vertical grid spacing

1. Surface layer thickness: 1/10 skin depth at shortest period in the most conductive surface block.
2. Increase the thickness of each layer by a factor 1.2 to 1.5 until one gets ½ skin depth in deep model at longest period.
3. The total depth of the model should be about 2 skin depths at the longest period. If the deepest block is more than ½ skin depth thick, the layer increase factor needs be reduced.

4.2.6 Horizontal grid spacing

1. Column width can increase away from the stations by a factor of 1.5 to 2.0. Ideally, one would want the model to be about twice as wide as it is deep.
2. Column widths should be about 1/3 skin depth in blocks where lateral inductive gradients are significant. Otherwise one wants to simply sample the half wavelength of the galvanic field. If there are enough sites so as not to alias the lateral response variation, then 1 block/site should be fine.
3. Block width can increase by a factor 1.2 to 1.5 in between stations depending on the spacing.
4. The block widths must be as uniform as possible within the area bounded by the stations.

4.3 3D inversion of MT data

WSINV3DMT (Siripunvaraporn et al., 2005) is a full 3D inversion program for Magnetotelluric data. It is extended and implemented from the 2D data space Occam inversion (Siripunvaraporn and Egbert, 2000). The inversion seeks the smoothest minimum structure model subject to an appropriate fit to the data.

The original Occam inversion was introduced by Constable et al. (1987) for 1D MT data. It was later expanded to 2D MT data by deGroot-Hedlin and Constable (1990). Occam inversion is stable and converges to the desired misfit in relatively small number of iterations compared to most other methods. They both are based on the model space method. Computational costs associated with construction and inversion of a model-space Occam approach makes 3D MT inversion impractical. This due to all computations depends on the size of model parameter, M.

These difficulties can be overcome with a data-space approach, where data space matrix (N x N matrix) dimensions depend on the size of the data set N, rather than the number of model parameters M. Generally, N << M for MT data. As discussed in Siripunvaraporn and Egbert (2000), the transformation of the inverse problem to the data space can significantly improve the computational efficiency for the 2D MT problem. The WSINV3DMT inversion code is based on the data space approach (Siripunvaraporn et al., 2005). With the transformation to data space the computational costs (i.e. CPU times and RAM required) are significantly reduced making the 3D inversion practical for PCs and workstations. The 3D forward modelling algorithm is based on a staggered grid finite difference solution of Maxwell's equations. This approach allows for complicated model structures (Siripunvaraporn et al., 2005).

- The data parameter size N is the total size of the dataset, which generally is the product of the number of periods N_p, the number of stations N_s, and the number of responses N_r (maximum is 8 for all impedances), i.e. $N = N_p N_s N_r$.
- The model parameter size M is the total number of discretization blocks, which is a product of number of discretization in x (north-south) M_x, number of discretization in y (east-west) M_y and number of discretization in z (vertical) M_z, i.e. $M = M_x M_y M_z$.

WSINV3DMT program requires RAM storage memory at least $1.2 \times (8N^2 + 8NM)$ to store the $N \times N$ representer matrix and $N \times M$ sensitivity matrix. The program requires extra memory for other computations. Total storage is dominated by these two matrices. The factor 1.2 which accounts for this is not exact, but is generally an average approximation. This factor ranges between 1.0-1.4 (or larger) depending on the size N and M.

4.3.1 Input files requirement for WSINV3DMT

There are several input files that need to be prepared before running WSINV3DMT. The Startup file lists all of the input files and several parameters used by the program. The data file contains the data, i.e. station locations, all impedance tensor data (real and imaginary part) and error bar of the impedance tensor. The initial model file defines the model grid size and the initial resistivity value of each model block. The optional files include prior model file and model control file. If users want to include "known" features in the model, such as the ocean, this control model index file is important.

For a detailed description of each of the above files refer to the user manual of WSINV3DMT by Siripunvaraporn et al., 2006.

5. 1D AND 2D INVERSION OF SYNTHETIC MT DATA FOR A GIVEN 2D AND 3D RESISTIVITY STRUCTURE

5.1 Introduction

Different MT inversion codes have been developed to model 1D, 2D and 3D resistivity structures over the last decades. The 2D inversion of MT data has been commonly used to model earth resistivity structures. The objective of this study is to compare whether 1D and 2D inversion codes reproduce similar resistivity structure as a given 2D and 3D resistivity model structures using synthetic data.

In order to achieve this objective, three programs (codes) were used. WSINV3DMT (Siripunvaraporn et al., 2005) was used to run a 3D forward modelling for a given 2D or 3D resistivity model structure. The EDI (Electrical Data Interchange) files were generated by forward modelling run using WSINV3DMT for a given resistivity structure or model. The EDI files are extracted from calculated response files. These EDI files were used to run 1D and 2D MT inversion. The program TEMTD (Árnason, 2006) was used to perform 1D inversion of MT data for the determinant of the impedance tensor. The program REBOCC (Siripunvaraporn et al., 1999) was used for 2D MT data inversion.

Four models are given below that are used to generate 2D and 3D synthetic data for 26 sites, 16 periods and 8 responses (real and imaginary parts of Z_{xx}, Z_{xy}, Z_{yx}, and Z_{yy}). The complex impedance tensors for 16 periods (0.1000, 0.1780, 0.3160, 0.5620, 1.0000, 1.780, 3.160, 5.620, 10.00, 17.80, 31.60, 56.20, 100.0, 178.0, 316.0, and 562.0 seconds) are forward modelled with 5% Gaussian noise. The model mesh used for the 3D forward modelling is 31 x 31 x 24 blocks. The model mesh has dimension of 219 km x 219 km x 104.4 km in x-, y- and z- directions. The central part of the model mesh was uniform, with a cell width of 1 km for 9 x 9 grids in x and y directions on the surface. Then it increases to 2 km, 3 km, 5 km, and up to 20 km in x- and y-directions. The model mesh thicknesses of the 24 layers in z direction are 30,30,40,100,100,200,300,400,500,600,700,800,900,1000,1000,2000,2000,3000,5000,8000, 10000,15000,20000,30000 metres. The total number of data parameters of the model were 26 x 16 x 8= 3328, and the total number of model parameters were 31 x 31 x 24 = 23064. A starting model of homogeneous half space of resistivity 100 Ωm is used for 1D and 2D inversion.

5.1.1 Model 1: Vertical conductive prism with variable dimensions (2D case)

The first model used to generate synthetic data consists of three conductive prisms with variable dimensions (shown in Figure 9). The top conductive vertical prism is 219 km x 9 km x 2.8 km and is embedded at a depth of 200 m at the central part of the mesh grid. The middle vertical conductive prism underlying the first prism is 219 km x 19 km x 7.7 km. The bottom conductive prism underlying the second prism is 219 km x 39 km x 93.7 km.
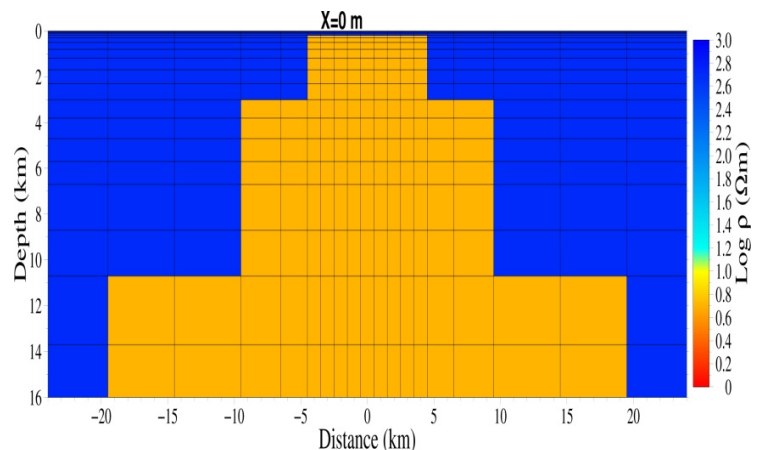
The resistivity cross-section obtained from 1D inversion using TEMTD for the determinant of impedance tensor is shown in Figure 10.

FIGURE 9: The 2D model used to generate data for the inversion on a profile in y direction at x=0. It consists of high conductivity blocks (5 Ωm) and low conductivity blocks (500 Ωm)

The cross-section of TE mode, TM mode and combined TE and TM modes of 2D inversion are shown in Figures 11, 12 and 13, respectively.
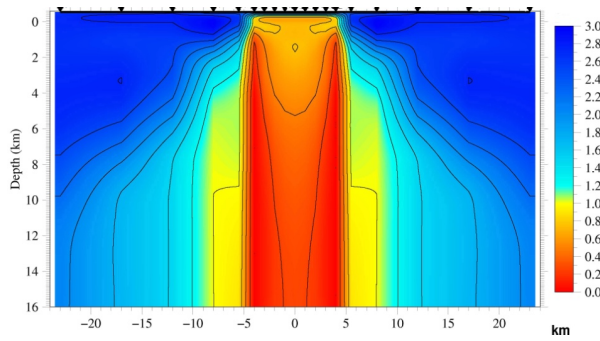
FIGURE 10: 1D inversion model (RMS=0.2) from response of the model given in Figure 5.1. The 1D MT site locations are shown as triangles on top
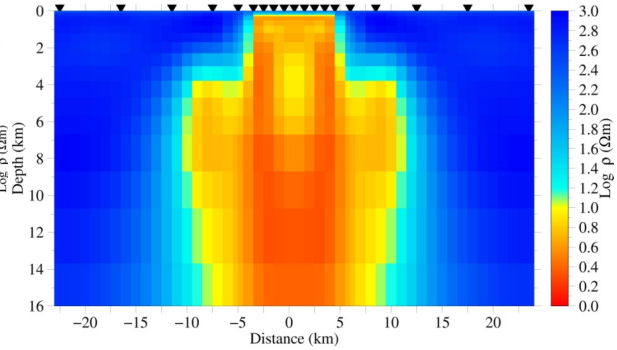

FIGURE 11: 2D inversion model using TE mode data from the model given in Figure 5.1. The 2D inversion model using TE mode data gave RMS of 1.3 after 8 iterations
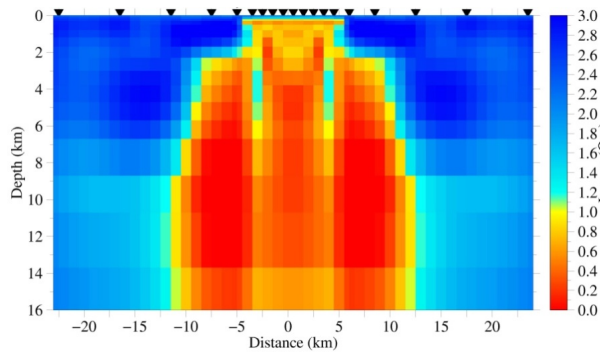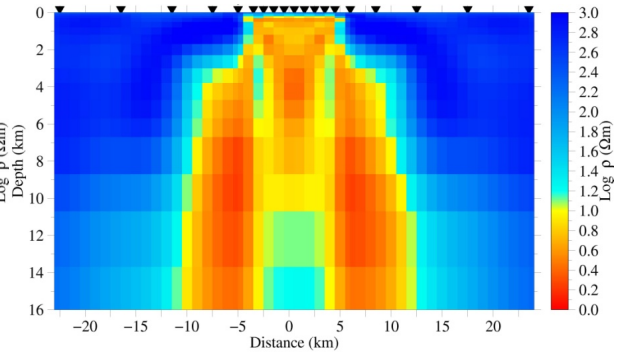

FIGURE 12: 2D inversion model using TM mode data from the model given in Figure 5.1. The 2D inversion model using TM mode data gave RMS of 1.6 after 15 iterations

FIGURE 13: 2D inversion model using both TE and TM modes data from the model given in Figure 5.1. Convergence of the joint inversion of TE and TM modes was attained after 12 iterations with RMS of 2.6

The 2D model used to generate the data for inversion shown in Figure 9 is not exactly reproduced by 1D and 2D dimensional inversion programs as shown in Figures 10, 11, 12, and 13. The 1D inversion of the determinant of the impedance tensor shows shrunk (contracted) anomaly of the conductive body in the centre of the cross-section as shown in Figure 10. The resistivity of the conductive body is underestimated in the central part of the cross-section within a horizontal distance of 9 km (Figure 10). Away from the centre (on both the left and right hand side) of the cross-section, resistivity of the conductive body is overestimated (Figure 10). The 2D inversion models using TM mode data and combined TE and TM mode shown in Figures 12 and 13 better reproduced the model shown in Figure 9 compared to the TE mode model in Figure 11. The TE mode model showed a decreasing horizontal dimension of the conductive body with increasing depth. This shows that the inductive effects for which TE mode is sensitive are decreasing as frequency is getting low. The edges of the third broad conductive prism at depth of 10.7 km on the model shown in Figure 9 are not well resolved by the 1D and 2D inversion programs used. This is because the inversion algorithm used here for the 1D and 2D inversion are based on Occam inversion technique which generates smooth models with minimum structures.

5.1.2 Model 2: Magma chamber buried at depth (3D case)

The initial model used for 3D forward modelling consists of a surface layer of high resistivity (500 Ωm) 200 m thick underlain by a low-resistivity second layer (10 Ωm) which is 100 m thick as shown in Figure 14. At the centre of the third 13.4 km thick layer of resistivity 50 Ωm is a low-resistivity body (magma chamber) of 5 Ωm is embedded at a depth of 3 km from the surface. The dimension of the magma chamber is 9 km x 9 km x 1.7 km. The bottom fourth layer is of resistivity 10 Ωm and 90.7 km thick.
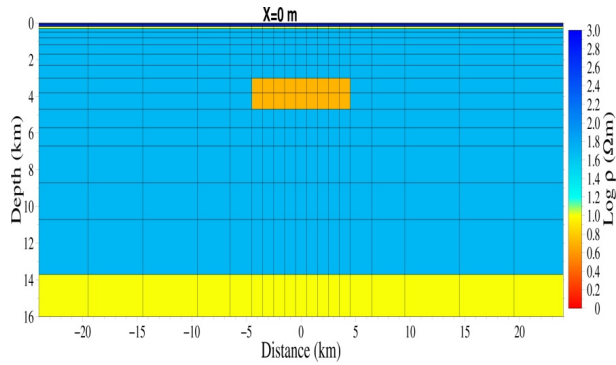
FIGURE 14: The 3D model used to generate data for the inversion on a profile in y direction at x =0. It consists of a surface layer of high resistivity (500 Ωm), a second layer of resistivity (10 Ωm), a third layer of intermediate resistivity (50 Ωm) and fourth layer of low resistivity (10 Ωm)

The EDI files extracted from the 3D forward modelling response are used to run 1D and 2D MT inversions.

The resistivity cross-section obtained from 1D inversion of the determinant of the impedances is shown in Figure 15.

The resistivity cross-section from 2D inversion using TE mode, TM mode and joint TE and TM modes data is given in Figures 16, 17 and 18, respectively.

The 3D model used to generate the data for inversion shown in Figure 14 is reproduced well by 1D and especially 2D inversion using TM mode data as shown in Figures 15 and 17, respectively. However, the true resistivity contrast between the host and the conductor are underestimated in both cases, i.e. the resistivity of the conductive body at depth of 3 km is overestimated. The 2D inversion result using TE and combined TE and TM modes data reproduced resistivity structure quiet differently from the given 3D model as shown in Figures 16 and 18. The 2D inversion of TE and combined TE and TM mode inserts spurious structures such as deep conductive roots beneath the body in an effort to account for 3D effect of the conductive body at depth of 3 km in the data (Figures 16 and 18). The low-resistivity layer at the bottom of the cross-section in Figure 14 is not resolved by 2D inversion of TE mode and combined TE and TM mode as shown on Figures 16 and 18. The 1D inversion for the determinate of the impedance tensor created an up-doming feature of the conductive body at the centre part of the bottom layer at a depth of 13.7 km (Figure 15). The resistivity of the layer at the bottom of the cross-section in the 3D model in Figure 14 is estimated as too low in the central part and too high at both margins by 1D inversion model for the determinant of the impedance tensor (Figure 15). The thin first and second layers which are 200 m and 100 m thick, respectively in the 3D model in Figure 14 are not resolved by 1D and 2D inversions shown in Figures 15-18. This is because the shortest period (0.1 s) used in the response calculation had skin depth greater than the thickness of the thin layers.
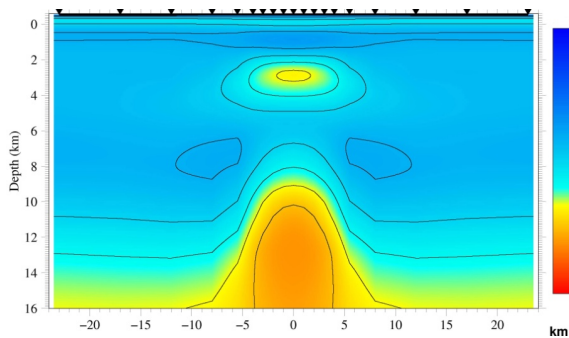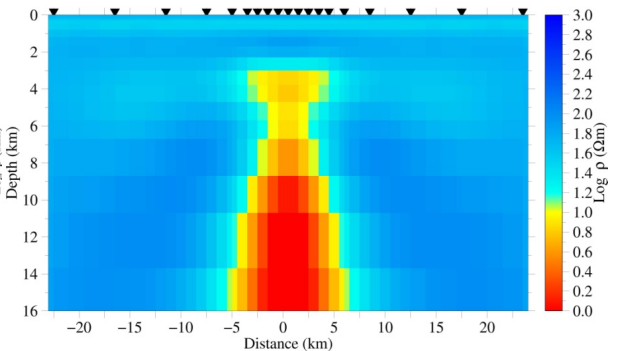

FIGURE 15: 1D inversion model (RMS= 0.1) from response of the model given in Figure 14

FIGURE 16: 2D inversion model using TE mode data from the model given in Figure 14. The 2D inversion model using TE mode data gave RMS of 1.5 after 10 iterations

5.1.3 Model 3: A resistive vertical body between two conductive bodies (2D case)

The third model used to generate data from the 3D forward modelling is shown in Figure 19. This model consists of central high-resistive block (500 Ωm) of 219 km x 3 km x 16 km in dimension and the two conductive bodies (5 Ωm) surrounding the resistive body at the centre are 219 km x 8 km x 104.2 km each.
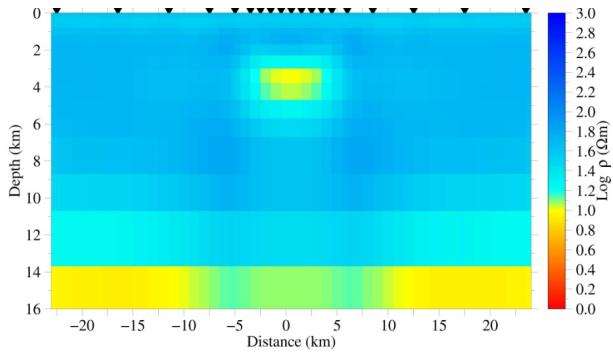
FIGURE 17: 2D inversion model using TM
mode data from the model given in Figure 14.
The 2D inversion model using TM mode data
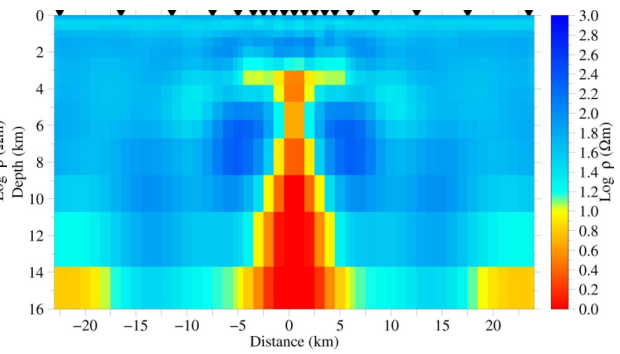gave RMS of 1.02 after 7 iterations

FIGURE 18: 2D inversion model using both
TE and TM mode data from the model given in
Figure 14. The 2D inversion model using joint
TE and TM modes data gave RMS of 1.8 after
10 iterations

The resistivity cross-section obtained from 1D inversion of the determinant of the impedances is shown in Figure 20. The resistivity cross-section from 2D inversion using TE mode, TM mode and joint TE and TM modes data are given in Figures 21, 22 and 23, respectively.

The 2D model used to generate data for inversion shown on Figure 19 is similarly reproduced by 1D inversion, two dimensional inversions for TM data and combined TE and TM modes data as shown on Figures 20, 22 and 23. The TE mode is resolved the conductive body compared to the resistive body (Figure 21). The TE data resolved the high-resistivity body at the centre of the model only at a shallow depth (Figure 21).

The TM mode is more sensitive to the contrast in resistivity (lateral boundaries) as compared to the TE mode. Thus TM mode which includes both inductive and galvanic effects resolved the lateral resistivity variation well. With increasing depth TM mode resolution of the resistivity contrast between the resistive body at the centre of the model and the surrounding low-resistivity bodies is decreasing.
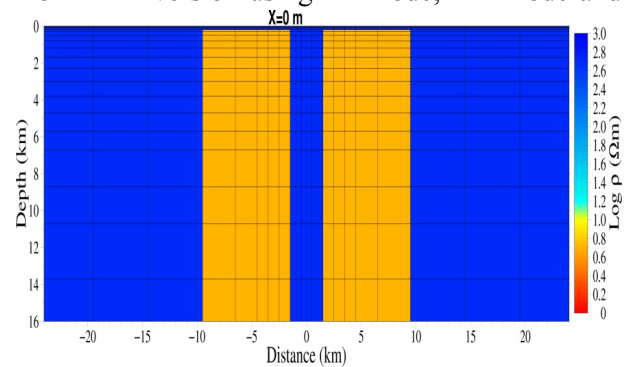

FIGURE 19: The 2D model used to generate
data for the inversion on a profile in y direction
at x=0. It consists of high conductivity blocks
(5 Ωm) and a low conductivity block (500 Ωm).
The two conductors are buried from 200 m
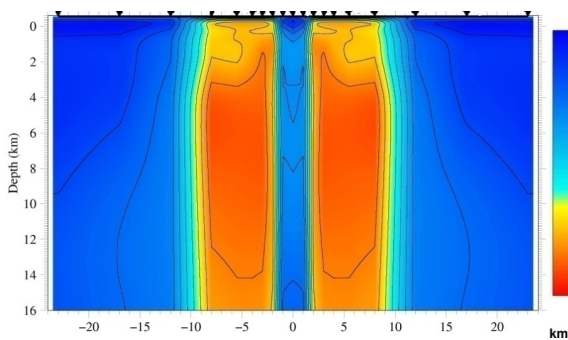below the surface to the bottom
of the model grid

FIGURE 20: 1D inversion model
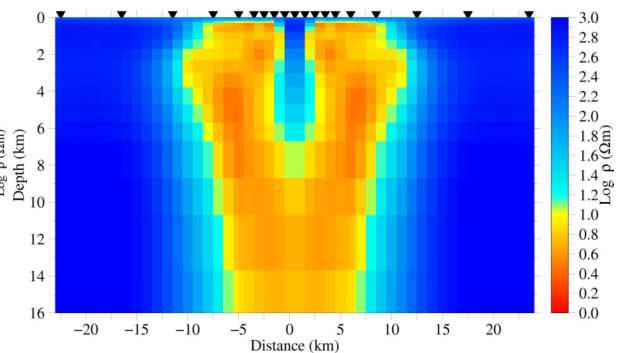(RMS= 0.6) from response of the model
given in Figure 19

FIGURE 21: 2D inversion model using TE
mode data from the model given in Figure 19.
The 2D inversion model using TE mode data
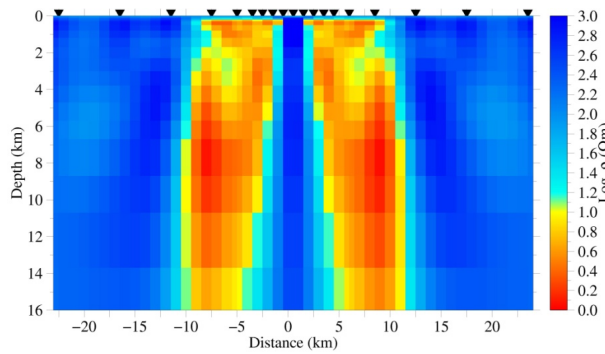gave RMS of 1.69 after 15 iterations

31

FIGURE 22: 2D inversion model using TM mode data from the model given in Figure 19. The 2D inversion model using TM mode data gave RMS of 1.5 after 9 iterations
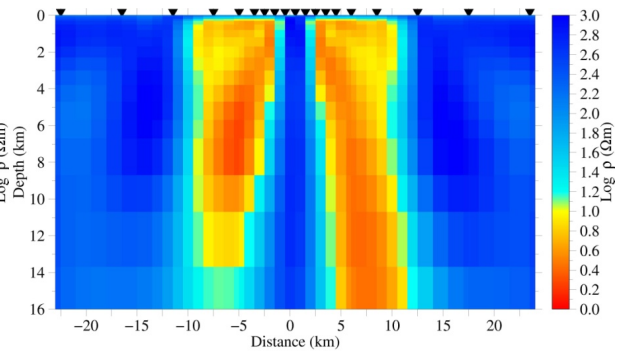

FIGURE 23: 2D inversion model using both TE and TM mode data from the model given in Figure 19. The 2D inversion model using joint TE and TM modes data gave RMS of 5.5 after 10 iterations

5.1.4 Model 4: Vertical conductive cylinder with variable dimensions (3D case)

The fourth model used to generate synthetic data consists of three vertical conductive cylinders with different base diameter and height placed at the centre of a resistive host body (shown in Figure 24). The top conductive vertical cylinder has a base diameter of 7 km, in thickness 2.8 km and is embedded at a depth of 200 m in the central part of the mesh grid. The middle vertical conductive cylinder underlying the first cylinder has a base diameter of 13 km and thickness of 7.7 km. The bottom conductive cylinder underlying the second cylinder has a base diameter of 29 km and thickness of 29.3 km.
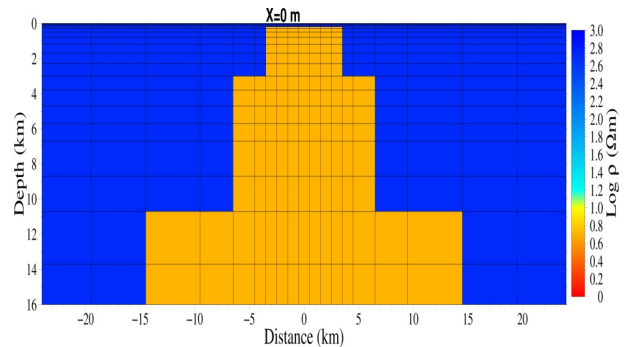
FIGURE 24: The 3D model used to generate the data for the inversion on a profile in y direction at x=0. It consists of high conductivity blocks (5 Ωm) and low conductivity blocks (500 Ωm)

The resistivity cross-section obtained from 1D inversion of the determinant of the impedances is shown in Figure 25. The resistivity cross-section from 2D inversion using TE mode, TM mode and combined TE and TM modes data are given in Figures 26, 27 and 28, respectively.

The 3D model in Figure 24 used to generate data was not reproduced well by 1D and 2D inversions as shown on Figures 25-28. The 1D inversion of the determinant of the impedance tensor shows shrunk (contracted) anomaly of the conductive cylinders at the centre of the cross-section as shown in Figure

FIGURE 25: 1D inversion model (RMS=0.2) from response of the model given in Figure 24

FIGURE 26: 2D inversion model using TE mode data from the 3D model given in Figure 24. The 2D inversion model using TE mode data gave RMS of 2.8 after 14 iterations

32

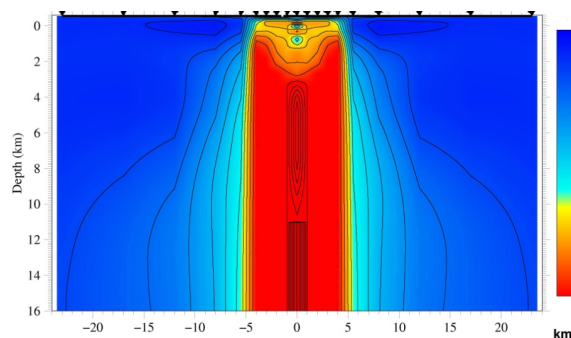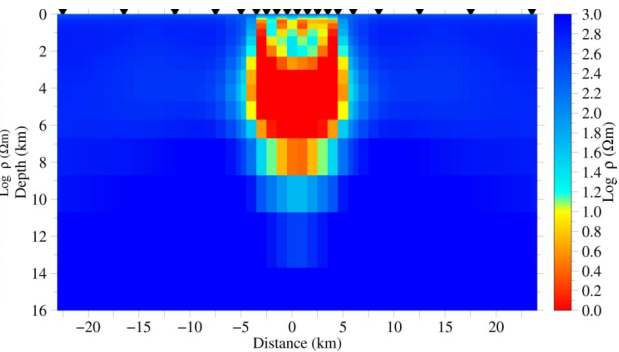25. The 1D inversion for the determinant of the impedance tensor underestimates the resistivity of the cylinders at the central part of the cross-section for horizontal distance of 10 km (Figure 25). Outside this central low resistivity for top, middle and bottom conductive cylinders resistivity is overestimated (Figure 25). The 2D inversion using TM mode which is sensitive to lateral boundaries (boundary charges) resolved the central part of the conductive cylinders for a horizontal distance of 10 km , but the resistivity estimate is too high (Figure 27). The 2D inversion using TE mode and combined TE and TM shows quiet different resistivity structure compared to the given 3D resistivity structure (Figures 26 and 28). This shows that TE mode has difficulty in resolving 3D effects of conductive cylinders.
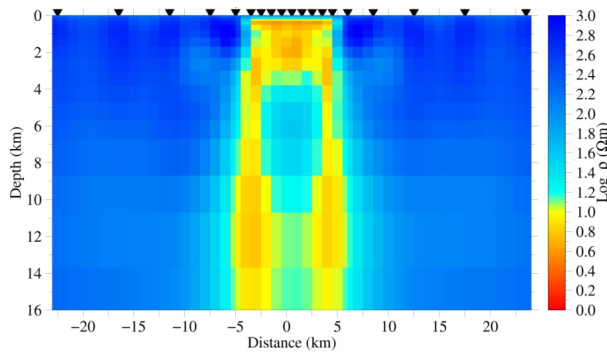

FIGURE 27: 2D inversion model using TM mode data from the 3D model given in Figure 24. The 2D inversion model using TM mode data gave RMS of 1.7 after 8 iterations
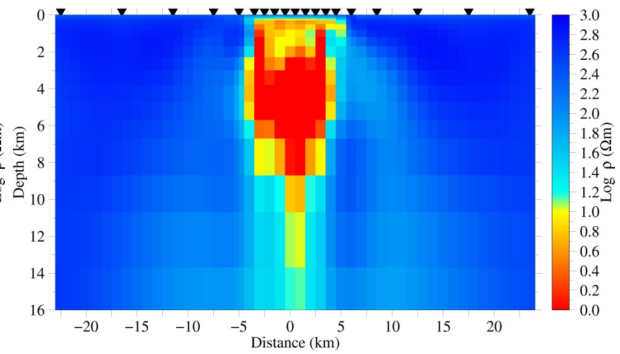
FIGURE 28: 2D resistivity inversion model using both TE and TM mode data from the 3D model given in Figure 24. The 2D inversion model using joint TE and TM modes data gave RMS of 3.3 after 11 iterations

5.2 Conclusions

The programs TEMTD and REBOCC are based on Occam inversion technique. Occam inversion produces a smooth model with minimum structure that fits a data set within certain tolerances, although a smooth model might not be the best fit to the data (deGroot-Hedlin and Constable, 1990). Since EM energy propagates diffusively, MT soundings resolve conductivity gradients rather than sharp boundaries or thin layers.

Complex geometries of synthetic data generated by 3D forward modelling were inverted by 1D inversion program (TEMTD) and 2D inversion program (REBOCC) of MT data. The 1D inversion for the determinant of impedance tensor reproduced contracted (shrunk) anomaly of conductive bodies of variable dimensions embedded within a resistive body for the given initial 2D and 3D resistivity model structures. Inverting only for the TM mode data generated a reasonable resistivity structure of the given 2D and 3D resistivity model structures. The 2D inversion of the TM mode is less affected by 3D effects caused by conductive structures (Wannamaker et al., 1984, Berdichevisky et al., 1998). This is because the TM mode is sensitive to lateral conductivity variation (galvanic effects) with charges uniformly distributed over the length of the body. However, the true resistivity contrasts can be underestimated by the TM mode inversion. The 2D inversion for the TE and joint inversion of TE and TM mode generated spurious structures such as deep conductive roots beneath the conductive body in some of the models generated to account for 3D effects. The accuracy of 2D approximation of 3D structures depends on geometry of the 3D body, conductivity and the mode of MT field used (Berdichevisky et al., 1995). The TE mode is more stable to 3D effects associated with bodies of high resistivity, in which charges are concentrated at the edge of the body and produce a small effect in the middle of the body (Berdichevisky et al., 1995). In general, the 2D and 3D synthetic models considered in the study were better reproduced (resolved) by 1D inversion of the determinant of impedance tensor and 2D inversion of TM mode data than by 2D inversion of TE mode and combined TE and TM mode data.

6. A CASE STUDY: MULTIDIMENSIONAL INVERSION OF MT DATA FROM KRÝSUVÍK HIGH-TEMPERATURE GEOTHERMAL FIELD, SW ICELAND

6.1 Introduction

In this part of the thesis, MT data modelling of Krýsuvík geothermal field using 1D, 2D and 3D inversion will be presented.

Krýsuvík is one of the high-temperature geothermal areas on the Reykjanes peninsula in south west Iceland. The Krýsuvík high-temperature geothermal field is divided into at least five sub-fields: Trölladyngja, Hveradalir-Seltún, Austurengjar, Köldunámur and Sandfell (Ármannsson et al., 1994).

A total of 96 MT and more than 200 TEM sites were acquired from Krýsuvík high-temperature geothermal field and surrounding area since 1989 (Eysteinsson, 1999 & 2001; Hersir et al., 2010). These data will be used to study the subsurface resistivity distribution of Krýsuvík high-temperature geothermal field using 1D and 2D inversion along two profiles and 3D inversion for the whole area.

6.2 Location and geography of the study area

Krýsuvík area is located about 25 km southwest of Reykjavík, the capital of Iceland, on the Reykjanes peninsula (see Figure 29).

FIGURE 29: Location Map of Krýsuvík geothermal field

Topographically, the study area has a relatively flat lava plain with an average elevation of about 200 m a.s.l. (Figure 29). The two elongated hyaloclastite ridges in the middle of the field range in elevation between 160 m and 400 m a.s.l.

6.3 Review of previous work

6.3.1 Geologic and tectonic setting of Reykjanes Peninsula and Krýsuvík

The Reykjanes Peninsula, SW-Iceland, is the on-land continuation of the Reykjanes Ridge section of the Mid-Atlantic Ridge. Volcanism takes place mainly within four fissure systems (Jakobsson, 1972; Pálmason and Saemundsson, 1974) (Figure 30). Several rock units of different ages and lithologies cover the Reykjanes Peninsula including postglacial basaltic lavas, interglacial and supraglacial lavas, and hyaloclastite and tuffaceous sediments beside other glacial and recent sediments.
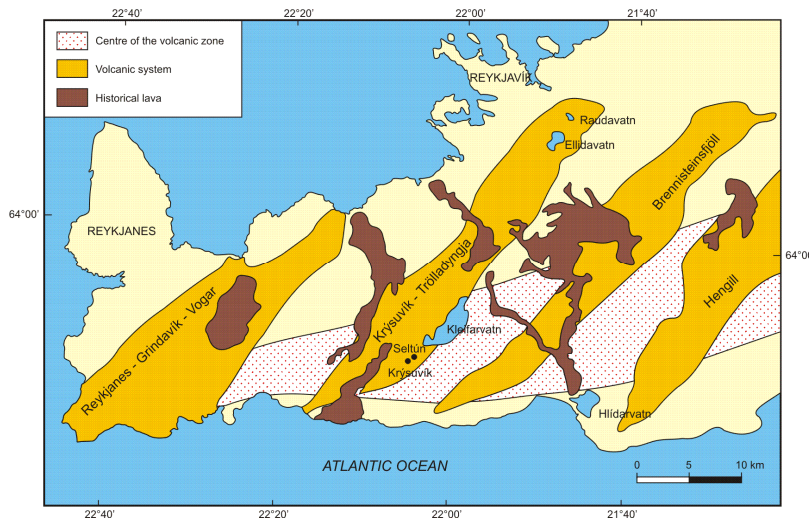
FIGURE 30: The main volcanic systems on Reykjanes Peninsula (modified from Jakobsson, 1972; picture courtesy to Abdelghafoor, 2007)

The EW ridge axis is at an oblique angle with the ESE-WNW plate spreading direction, is the reason for the en-echelon arrangement of the fissure systems (Figure 30). The only occurrence of acid lavas on the Reykjanes Peninsula is in the Hengill volcanic system, located in the eastern most fissure system (Saemundsson, 1995).

Krýsuvík is located at the boundary between an area of predominantly supra glacial eruptions (e.g. table mountains) to the east and an area of predominantly subglacial eruptions to the west,

with formations such as hyaloclastite ridges. The Inter- and Postglacial volcanism, i.e. volcanic activity during the ice free periods, is represented by subaerial volcanic products and morphological landscape like explosion craters and lava flows. The common products are lava flows, pyroclastic scoria, welded lava and scoria and explosion breccias (Vargas, 1992). Malapitan (1995) described the rocks of the Krýsuvík high-temperature area as consisting of extensive post-glacial lava and ridges of pillow lava, pillow breccias and hyaloclastites formed under the ice sheet environment (Figure 31).

Krýsuvík lies in a NE-SW elongated valley within the active volcanic zone which is characterized by fissure swarms striking NE-SW. The Krýsuvík fissure swarm is one of these large en-echelon structural units (fissure swarms) of the Reykjanes Peninsula (Vargas, 1992). Surface manifestations of the Krýsuvík geothermal system are marked by a high-intensity clay alteration zone, boiling springs, warm springs, mud pools, warm soil, hydrothermal explosion craters and mineralized water in Graenavatn Lake, deposits of silica sinters, oxidation, sulphate deposits, steam vents and mineral veins.
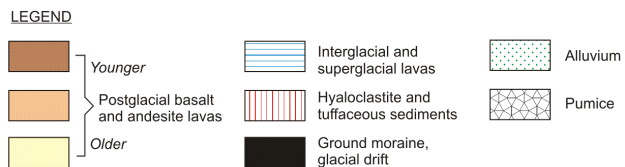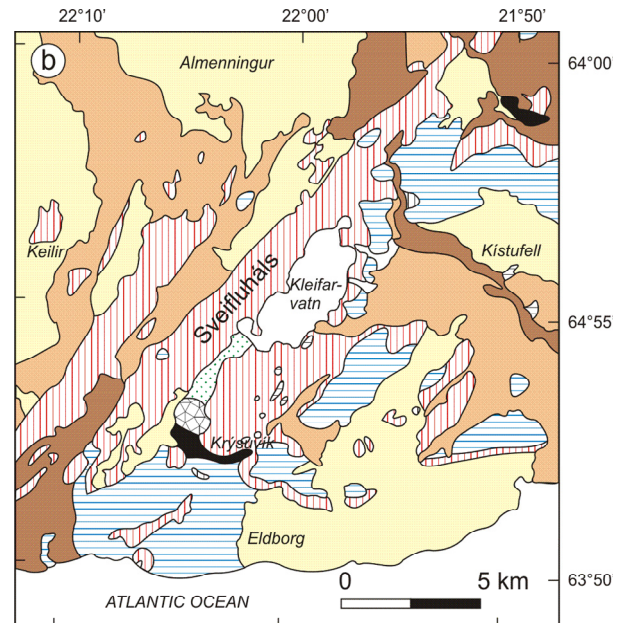

FIGURE 31: Regional geological map of Krýsuvík and the surrounding area (redrawn from Saemundsson and Einarsson, 1980; picture courtesy to Abdelghafoor, 2007)

6.3.2 Previous geo-scientific work

The Krýsuvík area attracted the interest of researchers for many decades (Arnórsson et al., 1975, Flóvenz et al., 1986; Georgsson, 1987, Eysteinsson, 2001, Magnússon and Árnason, 2002);

Fridleifsson et al., 2002; Mortensen et al., 2006; Hersir et al., 2010). Several geological, geophysical and geochemical studies have been carried out in the Krýsuvík geothermal field. Previous geological maps were prepared by Imsland (1973), Jónsson (1978), Saemundsson and Einarsson (1980) and Saemundsson et al., (2010). Imsland (1973) mapped Sveifluháls and classified the rocks there into eight stratigraphic units composed of hyaloclastite, glacial sediments and other volcanic materials, while Jónsson (1978) made detailed maps (scale 1:25,000) of the entire Reykjanes Peninsula, but mostly focussed on mapping the Holocene lavas. Saemundsson and Einarsson (1980) prepared a more generalized geological map of the Reykjanes Peninsula in the scale 1:250,000. Vargas (1992) studied the geological and geothermal condition of the Krýsuvík valley, producing a geological map for the area south of the Lake Kleifarvatn. Saemundsson et al., (2010) have published a new geological map of south west Iceland in the scale 1: 100000.

Arnórsson et al. (1975) carried out an exploration programme consisting of two phases: (1) a surface exploration using geophysical, geological and geochemical methods; and (2) drilling of slim 800-1000 m deep exploratory wells. As part of their study, an electrical resistivity map at 600 m depth based on Schlumberger DC soundings were produced that showed the Sveifluháls area with three different resistivity zones: < 10 Ωm, 10-30 Ωm and 30-50 Ωm.

The earlier reports (such as Arnórsson et al., 1975) showed the maximum logged temperature in the Krýsuvík-Trölladyngja area as high as 262°C (in well KR-06 at Trölladyngja). All wells except well KR-07 indicate temperature inversion at various depths in Krýsuvík high-temperature geothermal field (e.g. Kamah, 1996; Fridleifsson et al., 2002). Arnórsson (1987) studied the gas chemistry of the Krýsuvík geothermal field, particularly in the Sveifluháls area and found from CO_2 geothermometer that the subsurface temperatures were in the range 290-300°C. Einarsson et al. (1991) investigated the youngest lava flows in the Krýsuvík area, using radiocarbon dating and tephrochronology to determine the age of the lavas. They suggested that these lavas were formed in an eruption in 1151 AD and named it the Krýsuvík Fires. Yohannes (2004) used silica and cation geothermometers to calculate temperatures for 19 fluid samples from Krýsuvík. Temperatures calculated by various solute geothermometers were generally higher than measured temperatures. This is indicative of mixing between ground water and geothermal fluids.

In the eighties an extensive resistivity survey was carried out in the area (Flóvenz et al., 1986; Georgsson, 1987). In general, the resistivity of surface layers above the ground water table is very high, especially in the Postglacial lava formations where the resistivity values are in the range of about 10,000 Ωm but low where the surface layer has been strongly altered; there the resistivity could go down to less than 15 Ωm. The low-resistivity layers are correlated with geothermal activity in permeable near-horizontal layers of hyaloclastite breccias, below which denser and cooler basalts dominate, manifested in increasing resistivity with depth (10-80 Ωm) (Georgsson, 1987). A large negative magnetic anomaly in the Krýsuvík area is believed to reflect a large up-flow zone from the past where a large body of rock has lost a part of its original magnetic properties through alteration and demagnetization (Arnórsson et al., 1975). Eysteinsson (2001) performed TEM resistivity measurements around Trölladyngja and Núphlídarháls. The resistivity cross-sections from the TEM survey show a low-resistivity cap underlain by a high-resistivity core as seen in most geothermal fields in Iceland. Kebede (2001) made comparison of DC and TEM method resistivity structures of the Krýsuvík area. According to the result of the two methods the Krýsuvík area is characterized by a high-resistivity surface layer, followed by low-resistivity layer. Hersir et al. (2010) made 1D joint inversion of the 96 MT/TEM soundings from Krýsuvík. Their results show similar subsurface resistivity structure as in other high-temperature geothermal fields in Iceland, a conductive layer related to hydrothermal alteration underlain by high resistivity. The anomalous resistivity structure stretches along the main fracture zone and to the southeast coinciding with fractures inferred from seismicity (Hersir et al., 2010). Magnússon and Árnason, (2002) inferred transform fault from earthquake studies in Krýsuvík area.

Clifton et al. (2003) reported on the surface effects of earthquakes in June 17th 2000. Part of their study covers the Kleifarvatn area. They concluded that the earthquakes occurred along N striking

right lateral strike-slip faults. A major hydrological effect was the draining of water through an open fissure in the lake bed, lowering the lake level by more than 4 m.

Geoffroy and Dorbath (2008) observed clear relation between seismicity and low V_p/V_s zones, as well as the clustering of seismicity beneath Krýsuvík area, and suggested that earthquakes were linked to high fluid pressures at depth.

6.4 Instrumentation and data processing of MT data

6.4.1 MT instrumentation

A 5-channel MT data acquisition system (MTU-5) and a 2-channel system (MTU-2EP) from Phoenix Geophysics Ltd (Figure 32) were used to record the MT data studied here. MTU-5 can acquire two channels of electric field data and three channels of magnetic data from coil sensors. MTU-2EP can acquire two channels of electric field. The MTU controls the data acquisition process, and converts the signals into digital format through 24 bit ADU. The instrument synchronizes to Co-ordinated Universal Time (UTC) via Signals from the Global Positioning System (GPS) satellites.

FIGURE 32: Phoenix V5-2000 MT system. From left to right; five non-polarizing electrodes, 3 induction coil cables, 3 MTC-50 induction coils, battery, MTU-5 recording unit, GPS antenna, and case for the unit. The picture is taken from Phoenix Geophysics website

The electric field components E_x and E_y are indirectly measured through the potential difference ΔV between two electrodes separated a distance d along the desired direction with $E = \Delta V / d$ (Figure 8). Both electrodes are in contact with the ground (soil) and are connected to the MTU-5 (data logger) that stores the measured signal. The separation between the electrodes used varies between 50 m and 100 m. The electrodes are composed of PbCl2 solution in a ceramic container that is designed to ensure a good contact between the outside wires and the soil.

6.4.2 Data processing

Time-series data were downloaded from the MTU-5 units and inspected using the program Synchro-Time Series View. This program allows viewing and printing graphical representations of the raw time-series data, power spectra derived from the time-series data and coherence between pairs of orthogonal electric and magnetic components. Using the program SSMT2000, provided by Phoenix Geophysics-Canada (Phoenix Geophysics, 2005), Fourier transforms were produced from the raw time-series data. The cross-powers were stored in files and could be displayed graphically using the MTU-Editor program. MT-Editor is a Window-based program which takes as input files created by SSMT2000. MT-Editor merges the cross powers and displays its calculations graphically. This leads to viewing the different characteristics of the sounding, such as apparent resistivity, phase, impedance, strike direction, coherence, and so on, across the full frequency range that was acquired.

MT-Editor also has the option to remove individual cross powers from the calculations, allowing poor quality data to be deleted from the average crosspower. The edits are made by changing a mask, not by deleting data, making it easy to restore individual cross powers or revert to the initial view. The program includes an auto-edit capability that quickly masks cross powers that lie too far from the mean, often saving considerable time in the editing process. When the user is satisfied with the edits, MT Editor Program allows saving the data for use with interpretation software. The EDI (Electrical Data Interchange) file is ready for plotting the resistivity and phase and to make 1D, 2D and 3D inversion (Figure 33).
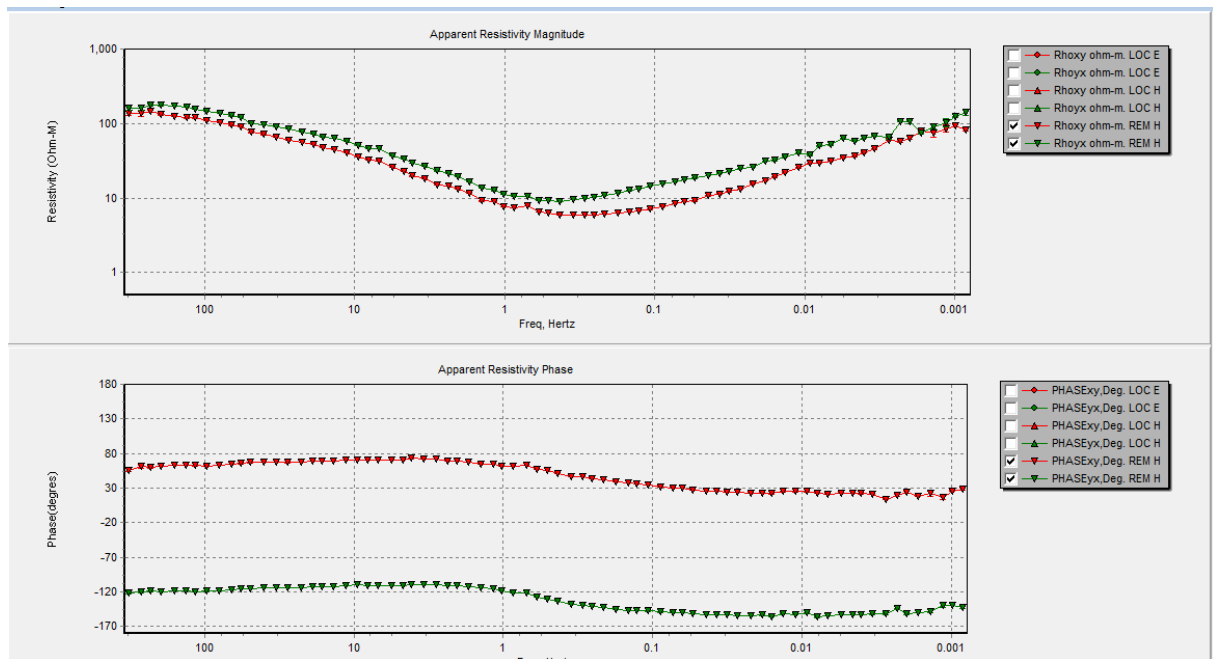
FIGURE 33: MT-Editor output showing apparent resistivity and phase curves (using Remote H as
reference for processing in the program SSMT2000) for MT site 20 measured on 26/07/07

The layout of the MT sensors were x in the magnetic north and y in the magnetic east direction. In the
program SSMT2000, the magnetic declination in Krýsuvík (17°NW) was provided so that the program
rotates the impedance tensor elements to the geographic north-south direction.

6.5 1D inversion of MT data

6.5.1 Joint 1D inversion of TEM and MT soundings

A total of 22 soundings were considered for the joint 1D inversion of TEM and the rotationally
invariant determinant of the impedance tensor for apparent resistivity (ρ_a) and phase (ϕ) of MT
soundings from the Krýsuvík area. The determinant of the impedance tensor is a kind of average
impedance tensor as opposed to considering only Z_{xy} or Z_{yx} for 1D inversion of MT data (see Equation
2.6.1.8 in section 2.6.1). Profile-1 contains 10 soundings and Profile-2 consists of 12 soundings
shown in the Figure 34 as well as mapped faults and fissures (Saemundsson et al., 2010). Profile-1 is
from NW to SE, from Keilir in the northwest to Austurengjar and Geitahlíd in the southeast with a
total distance of about 11 km (Figure 34). Profile-2 runs from Núphlíd in the southwest passing
through Köldunámur to Undirhlídar in the northeast with a total distance of about 17 km (Figure 34).

Typical examples of the measured apparent resistivity and phase curves of Profile-1 and Profile-2 are
shown in Figure 35. They exhibit at short periods (< 1 s) decreasing apparent resistivity values with
increasing period, and increasing apparent resistivity and decreasing phase for periods greater than 1s,
which indicate an increase in apparent resistivity with depth. High phase values (> 45°) at short
periods indicate a conductor at shallow depth. At long periods (> 100 s) the apparent resistivity value
approaches 100 Ωm. The xy and yx apparent resistivity curves start splitting from each other starting
from short periods for all the sites considered in Figure 35. This shows the non 1D resistivity structure
of the MT soundings.

In order to counteract the static shift problem of the MT soundings, TEM data from the same site were
jointly inverted with MT data in the 1D inversion of the rotationally invariant determinant of the
impedance tensor. This method is discussed in detail in section 2.8. A typical plot from the 1D joint
inversion of TEM and MT data (site 68 on Profile-2) is shown on Figure 36. The Figure depicts the
estimate of shift multiplier for site 68 which is given as Shift=1.31 in the upper right corner of the
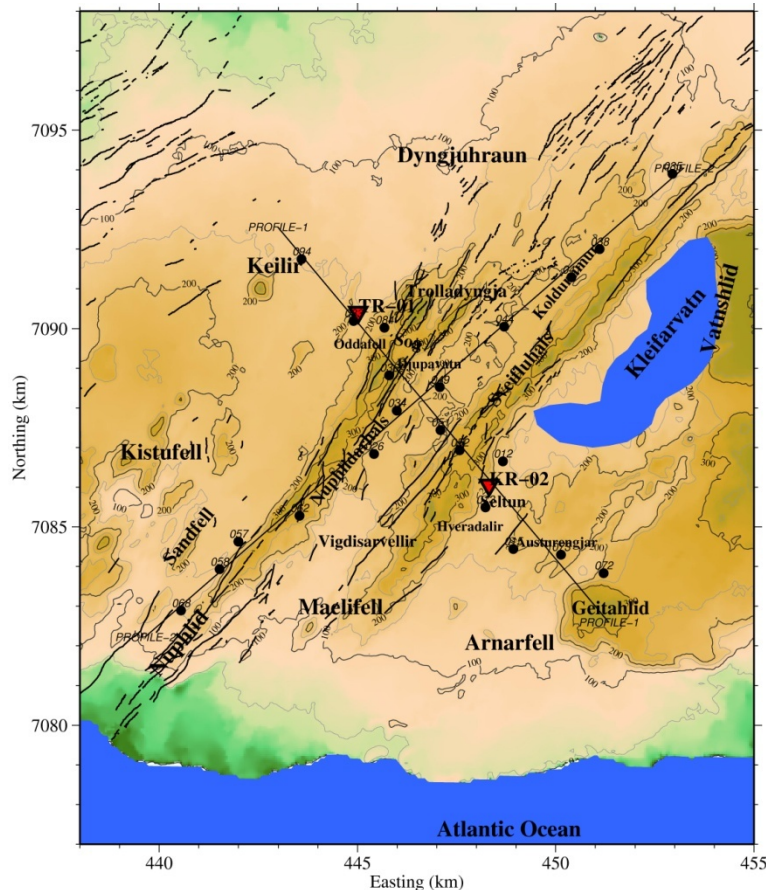
FIGURE 34: Location of Profile-1 and Profile-2 used in the 1D and 2D inversions of MT data in Krýsuvík geothermal field. Profile-1 runs from NW to SE and Profile-2 from SW to NE. The TEM soundings are from the same location as the MT soundings. The Northing and Easting are in UTM units (km). The black dots are MT soundings. Faults and fissures are shown as black lines. The inverted triangles are geothermal wells

apparent resistivity panel. The MT apparent resistivity has to be divided by the shift multiplier in order to get the shift corrected apparent resistivity to tie in with the TEM data.

The static shift statistics of the 22 MT sites obtained from the joint 1D inversion of TEM and MT data is given as a column chart in Figure 37. Out of the 22 MT sites, 7 MT sites were shifted upwards (shift > 1), 14 MT sites were shifted downwards (shift <1) and 1 MT site was not shifted (shift=1). A shift of MT sounding by 0.1 downwards will result in 10 times too low apparent resistivity values and about three times too small depths to resistivity boundaries (skin depth formula in Equation 2.7.1.5). This shows that not correcting for static shift in MT will result in erroneous values of the apparent resistivity and depths values (Árnason, 2008; Árnason et al., 2010).

All high-temperature geothermal fields in Iceland where the host rocks are volcanic have a similar resistivity structure (Flóvenz et al., 1985; Árnason et al., 1987; Eysteinsson et al., 1994; Árnason et al., 2000; Flóvenz et al., 2005). At a certain depth, a low-resistivity (conductive) cap or zone domes up (the outer margin of the reservoir) and is underlain by higher resistivity (a resistive core) (Árnason and Flóvenz, 1992; Árnason et al., 2000). The shallow resistivity structure of high-temperature geothermal systems in basaltic rocks in Iceland is controlled by alteration mineralogy (hydrothermal alteration) (Kristmannsdóttir, 1979; Árnason et al., 2010). The unaltered surface layer has relatively high resistivity and the conduction is mainly pore fluid conduction (Flóvenz et al., 2005). At temperatures of 50-100°C pronounced geothermal alteration occurs with smectite and zeolites as the dominant alteration minerals and the rocks become conductive (mineral conduction) (Flóvenz et al., 2005). At higher temperatures, in the range of 220-240°C, smectite and zeolites are gradually replaced by chlorite as the dominant alteration mineral in mixed layered clay zone and the resistivity increases again most likely due to reduced cation exchange capacity of chlorite (Kristmannsdóttir, 1979; Flóvenz et al., 2005). At still higher temperature epidote becomes abundant (Kristmannsdóttir, 1979; Flóvenz et al., 2005). However, alteration minerals sometimes have indicated a lower or higher temperature than measured in the wells (Árnason et al., 2010). This was interpreted as indicating a young system still heating up with alteration lagging behind and, therefore, not in thermal equilibrium (Árnason et al., 2010). In other cases it showed cooling of the system. The smectite and the zeolites have loosely bound cations that make these minerals conductive, whereas in the chlorites all ions are bound in a crystal lattice, and make them more resistive (Deer et al., 1962).
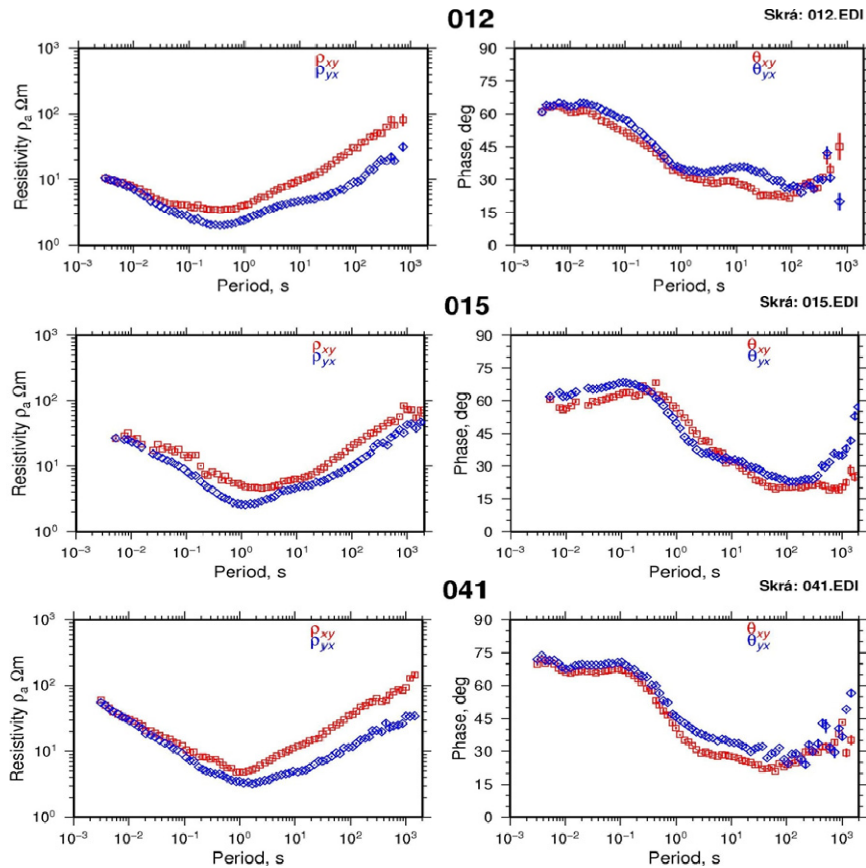
FIGURE 35: Measured apparent resistivity and phase curves from site 012, 015 and 041 on Profile-1 and Profile-2. Location of the sites is shown on the Figure 6.6. Red squares show apparent resistivity and phase in xy (NS) direction. Blue diamonds show apparent resistivity and phase in yx (EW) direction

The resulting resistivity cross-section from the joint 1D inversion of TEM and MT data for Profile-1 is shown on Figure 38. The joint inversion model for each station on Profile-1 is given in Appendix A. The model matches with alteration mineralogy zones of borehole TR-01 and KR-02 (Fridleifsson et al., 2002; Kamah, 1996). The smectite-zeolite zone and mixed layer clay zone correlated with the low-resistivity structure and the chlorite-epidote zone correlated with the high-resistivity structure down to a depth of about 2.3 km (Figure 38). There is a discrepancy in matching between the temperatures indicated by alteration minerals zones and the temperature measured in well KR-02 (Figure 39). For well KR-02, the chlorite-epidote zone which is indicative of temperature above 240°C was found at a depth of 640 m b.s.l. according to alteration mineral zonation (Figure 39). But well KR-02 encountered temperatures lower than 170°C at 600-1000 m depth according to the temperature measured in well KR-02 (Figure 39). This is presumably because the system has undergone cooling after high-temperature alteration minerals formed.

The resistivity cross-section of Profile-1 extending to a depth of 10 km shows three major resistivity structures to a depth of 10 km (Figure 40). A high-resistivity layer (> 100 Ωm) 200-800 m thick is observed at the surface. A second layer of low resistivity (≤ 15 Ωm) 400-1000 m
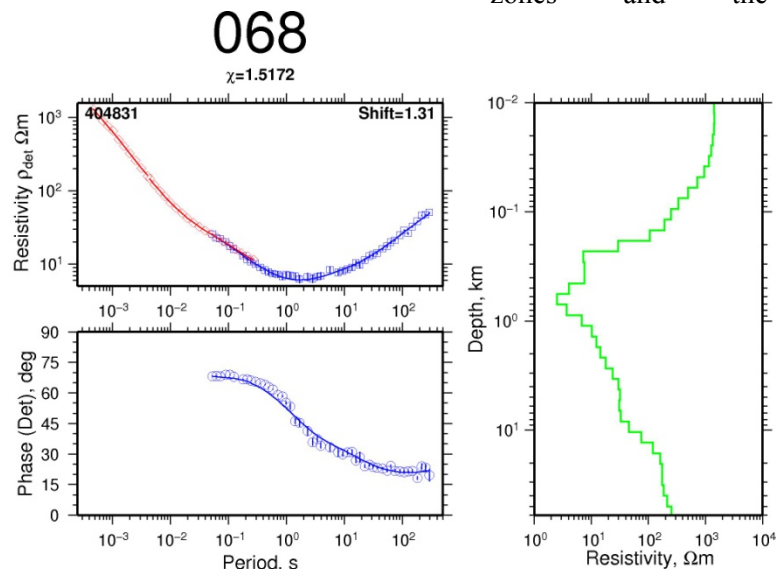

FIGURE 36: Result of 1D joint inversion of TEM and MT data for site 68 on Profile-2. Red diamonds are measured TEM data. Blue squares and blue circles are measured MT apparent resistivities and phases, respectively obtained from the determinant of the MT impedance tensor. The solid curves in the left panels are calculated responses from the Occam inversion model to the right
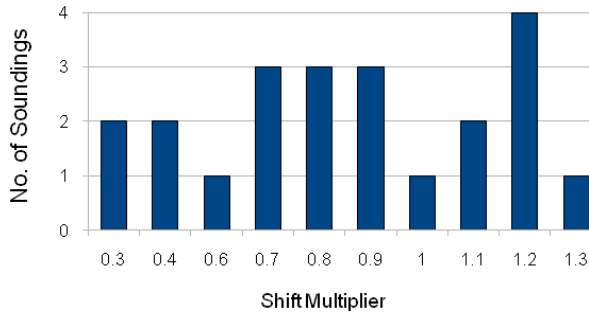
FIGURE 37: Column chart showing static shift
multipliers and corresponding number
of MT soundings

thick is observed underlying the surface high-resistivity layer. High resistivity (> 15 Ωm) is observed at the bottom of the cross-section. There is an indication of low-resistivity body embedded within a third layer of high resistivity at a depth of 2 km under sites 12 and 13.

The resistivity cross-section of Profile-2 also shows resistivity structure similar to that of Profile-1 (Figures 41 and 42). A low-resistivity cap (≤ 15 Ωm) is underlain by a high resistivity (> 15 Ωm), the resistive core. The joint inversion model for each station on Profile-2 is given in Appendix A. The resistivity cross-section of Profile-2 to a depth of 10 km also shows no change of resistivity below 5 km.
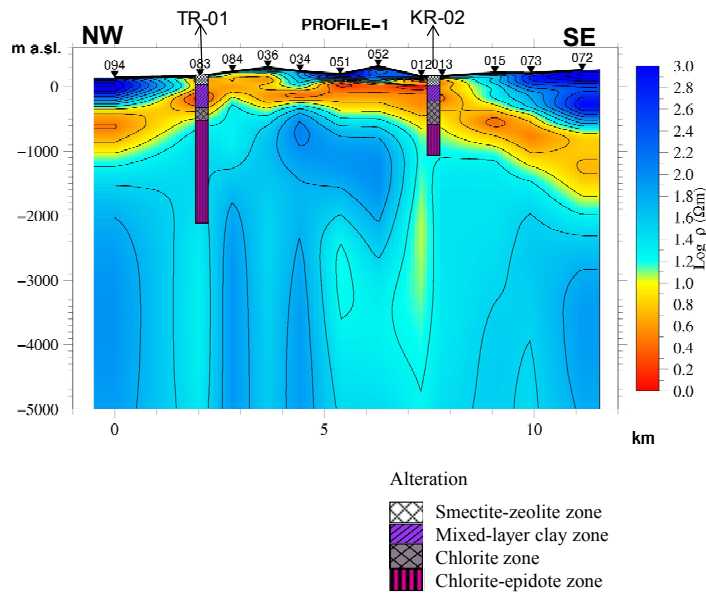

FIGURE 38: Compiled resistivity cross-section for
Profile-1 from 1D inversion of each sounding and
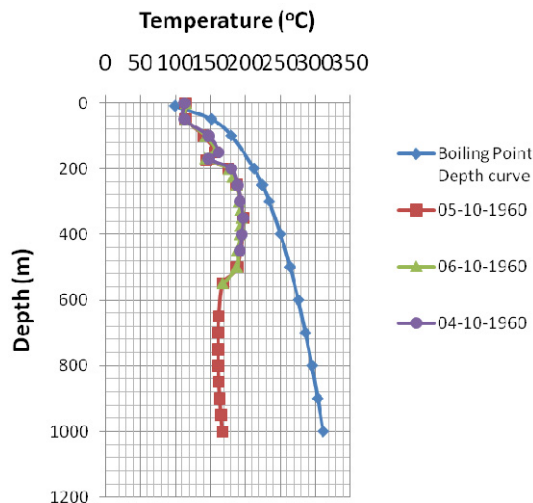alteration mineralogy data from wells
TR-01 and KR-02

FIGURE 39: Temperature profile of well
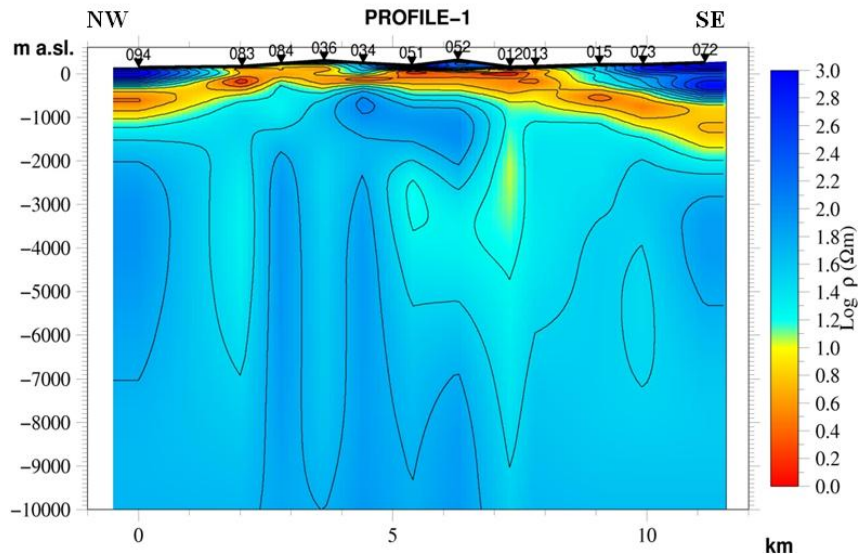KR-02 (from ÍSOR database)

41

FIGURE 40: Compiled resistivity cross-section from the joint 1D inversion of
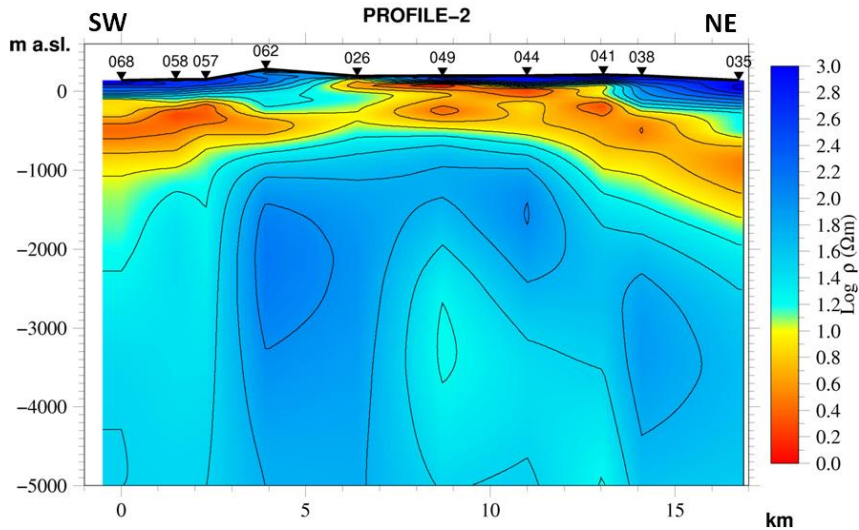TEM and MT data for Profile-1

FIGURE 41: Resistivity cross-section from the joint 1D inversion of
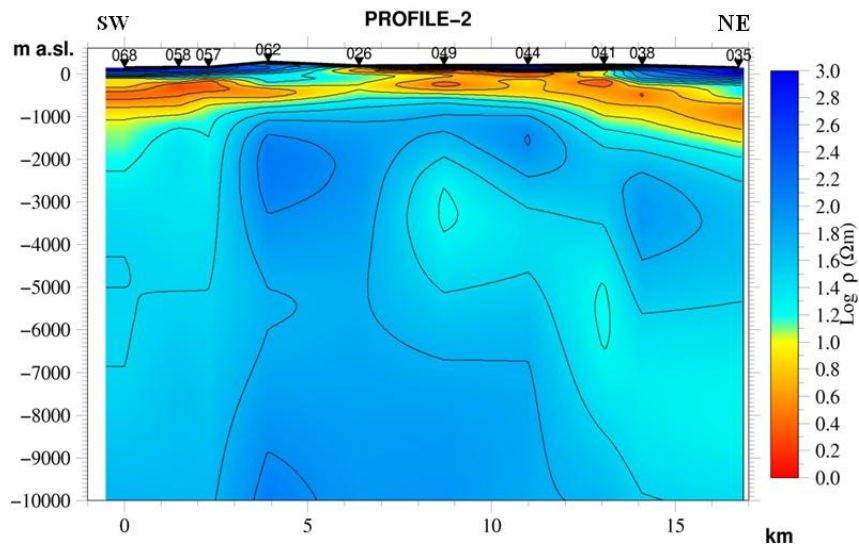TEM and MT for Profile-2 extending to a depth of 5 km b.s.l.

FIGURE 42: Resistivity cross-section from the joint 1D inversion of
TEM and MT for Profile-2 extending to 10 km b.s.l.

6.5.2 Conclusion

The resistivity cross-sections of Profile-1 and Profile-2 from the 1D joint inversion of TEM and MT data show three major resistivity structures. The high-resistivity surface layer can be interpreted as unaltered basaltic lava and hyaloclastites. The low-resistivity layer (≤ 15 Ωm) below the high resistivity can be correlated to the smectite-zeolite or mixed layer clay alteration zone. Below the conductive layer, high resistivity (> 15 Ωm) is observed, which can be correlated to the chlorite-epidote alteration zone as confirmed from the alteration zones of well TR-01 to a depth of about 2.3 km (Fridleifsson et al., 2002). The resistivity structure observed on the two profiles is similar to other high-temperature geothermal fields in Iceland, which is controlled by alteration mineralogy (Árnason et al., 2000; Flóvenz et al., 2005; Árnason et al., 2010). They are characterized by a low-resistivity cap underlain by high-resistivity core. If the alteration and temperature are in equilibrium, the subsurface resistivity structure reflects not only alteration but also the temperature to expect (Árnason et al., 2000). In case of well KR-02 shown on Profile-1, the temperature indicated by alteration is higher than the actual measured in the well. This shows that the system has most likely been cooling down (Árnason et al., 2010). The resistivity cross-section from the 1D joint inversion of TEM and MT data of the two profiles do not reveal a good conductor at great depth which could be associated to heat source of the geothermal system.

6.6 2D inversions of MT data

2D inversion of MT data was performed along the two profiles discussed in the previous chapter. Location of the profiles is shown in Figure 34. A total of 22 soundings were inverted. The program REBOCC was used for the 2D inversion.

6.6.1 Dimensionality analysis of the MT soundings

There are different ways of analysing the dimensionality of MT impedance tensor elements. This includes skew, polar diagrams, tipper, ellipticity, etc. as discussed in section 2.6.1.
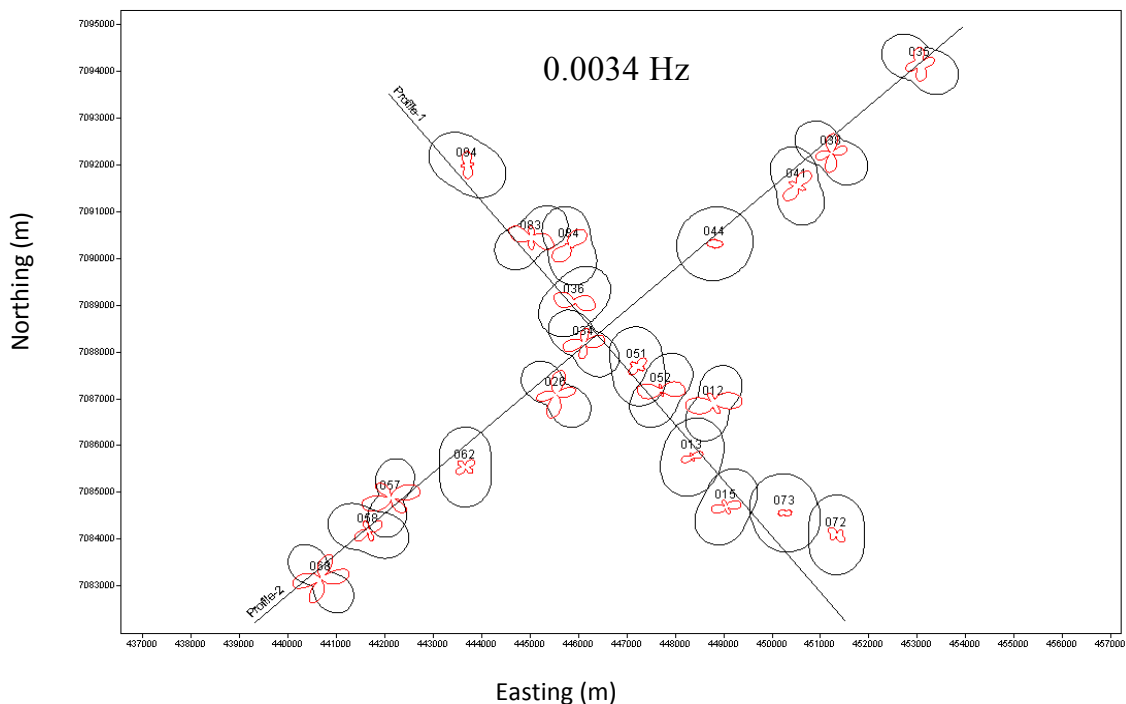

FIGURE 43: Impedance polar diagram for MT sites. The polar diagram show 1D, 2D and 3D structures at frequency of 0.0034 Hz. (|Zxx| =red colour and |Zxy|= black colour in the polar diagram)

A typical example of impedance polar diagram from the 22 MT sites at a frequency of 0.0034 Hz is shown in Figure 43. The polar diagrams were plotted from measured data.

Even though the dimensionality information from the polar diagrams for the two profiles show complicated dimensionality (1D, 2D and 3D) at every frequency and every sounding, 2D inversion was carried out.

6.6.2 Strike direction analysis

When measuring MT, the field setup is not necessarily along geoelectric strike direction. For a 2D Earth with x' or y' direction aligned along electromagnetic strike, Z_{xx} and $Z_{yy,}$ become zero. Measured data rarely have the diagonal impedance tensor elements equal to zero in any co-ordinate system.   The most common approximation is based on the maximization of the off-diagonal elements of the MT tensor and minimization of the diagonal ones, using the sum of the squared modulus of these components (Equations 2.6.1.5 and 2.6.1.6). The resulting strike angle is called Swift angle (principal angle).

The rose diagrams on Figure 44 show the Swift angles for all frequencies (320-0.00114 Hz) for MT sites on two profiles.

FIGURE 44: Rose diagrams showing Swift angles for all data sets on the two profiles

The rose diagrams in Figure 44 show that the Swift angle varies from site to site. The Swift angles on the rose diagram are trending NE-SW/ NNE- SSW direction in general. The rose diagram shows for most of the MT sites a geoelectric strike trending in NE-SW direction and this coincides with the dominant geologic strike of the survey area (Imsland, 1973; Jónsson, 1978; Saemundsson and Einarsson, 1980). Since most of Swift angles of the geoelectric strike are in NE-SW direction, the impedance tensor elements were rotated to align to the dominant geologic strike N40°E for MT sites on Profile-1. Because of 90° ambiguity of the geoelectric strike, soundings on Profile-2 were rotated to N50°W to get the second possible geoelectric strike. In both cases xy mode is TE mode and yx mode is the TM mode.

6.6.3 Static shift correction

After rotating all the MT soundings on the two profiles to the geoelectric strike directions, MT impedances are decoupled into two modes, i.e. the TE mode (electric field parallel to the strike) and the TM mode (electric field perpendicular to the strike) (see section 2.7.2 for details on 2D MT theory).

TEM data from the same location were used to correct for the static shift of MT data before the 2D inversion. 1D joint inversion of TEM and MT data for xy (TE mode) and yx mode (TM mode) for the apparent resistivity (ρ_a) and phase (ϕ) was performed for the rotated MT impedances to find the static shift multipliers.

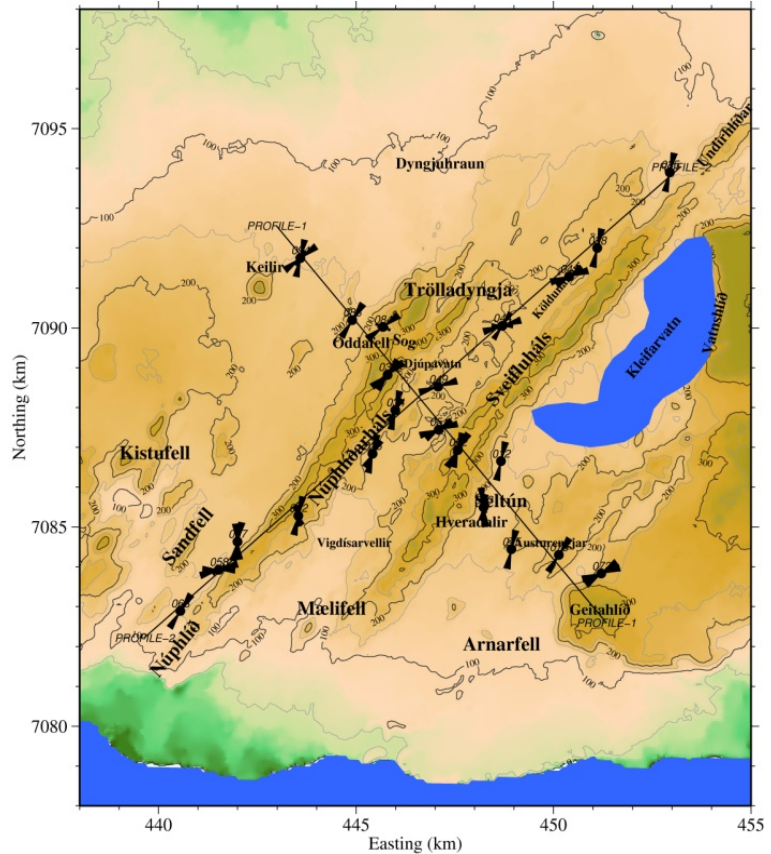The statistics of shift multipliers for the TE and TM modes obtained is given as column chart shown in Figure 45. The shift multipliers are in the range from 0.1 – 2.2.

An example of 1D joint inversion of TEM and TE mode of MT data is shown in Figure 46.

A pseudo-section plot for static shift uncorrected and corrected apparent resistivities, ρ_a of the TE mode of MT data for Profile-1 are shown in Figure 47 and TM mode is in Figure 48.
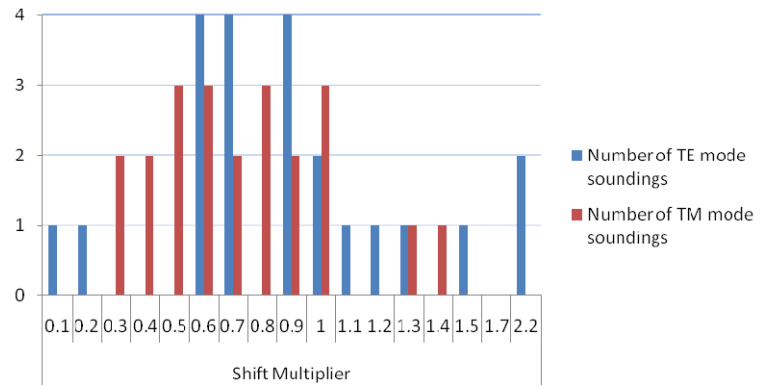

FIGURE 45: Column chart of shift multipliers for the MT soundings used in the 2D inversion. The meaning of the shift multipliers is similar to the ones discussed in Section 6.5
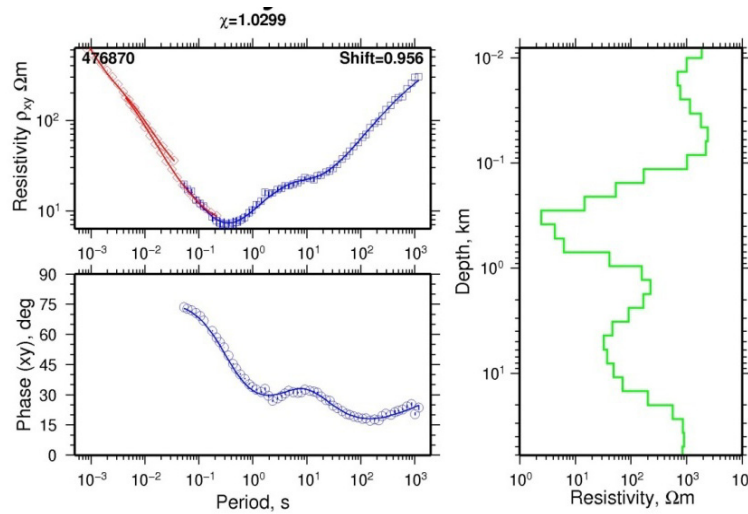

FIGURE 46: Joint inversion of TEM and TE mode of MT data. Red diamonds are the measured TEM apparent resistivity. Blue squares and circles are the apparent resistivity and phase from the TE mode, respectively. The solid curves in the left panels are calculated responses from Occam inversion. On the right top corner of the resistivity panel the shift multiplier = 0.956 is shown. This implies that the MT apparent resistivity has to be divided by 0.956 to tie in with the TEM data
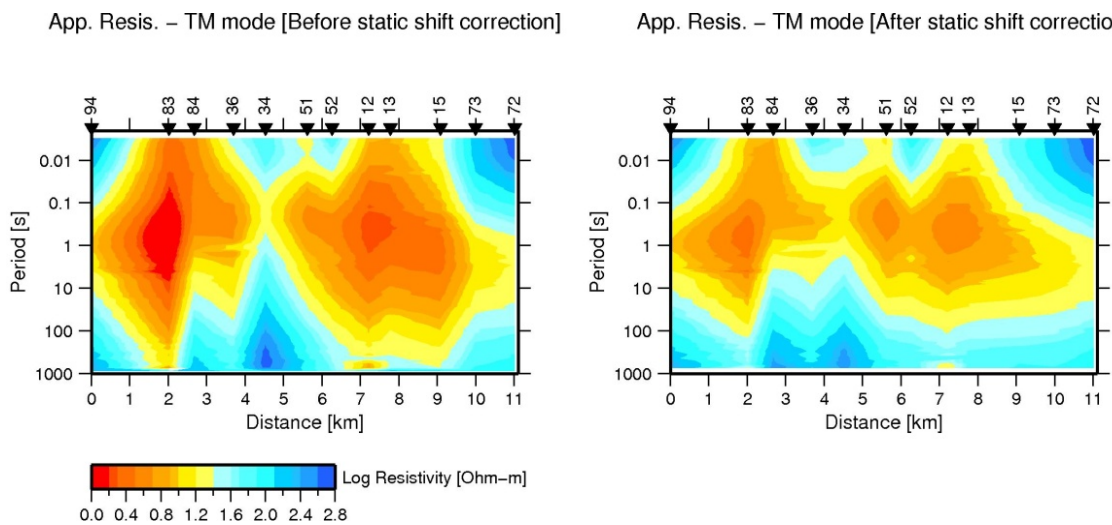

FIGURE 47: Pseudo-section plots of the static shift uncorrected and corrected apparent resistivity of TE mode of MT data for Profile-1

45

App. Resis. – TE mode [Before static shift correction]   App. Resis. – TE mode [After static shift correction]
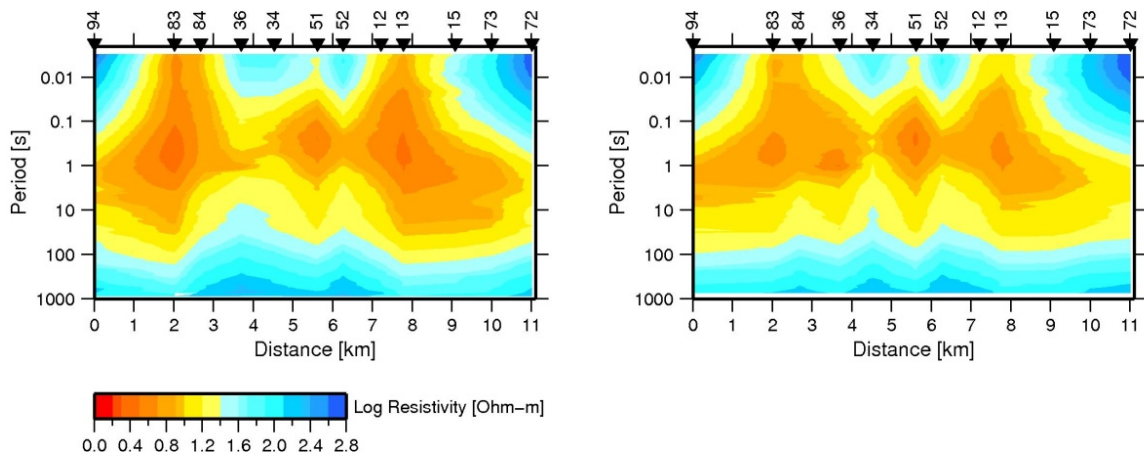
FIGURE 48: Pseudo-section plots of static shift uncorrected and
corrected apparent resistivity of TM mode of MT data for Profile-1

From 6.19 and 6.20, the TM mode data are more shifted than TE mode data for Profile-1. This does not apply to soundings on Profile-2 as seen in Figure 45 in general. Static effects are caused by inhomogeneities close to the surface of the Earth. (See section 2.8).

6.6.4 2D MT mesh grid design

The model mesh for 2D inversion was designed according to the general rule of the thumb procedure given in Section 4.2. The model mesh used to invert 2D MT data using REBOCC contains 52 horizontal and 39 vertical blocks (Figure 49).   Hence, the mesh contains a total of 2028 cells of varying sizes.
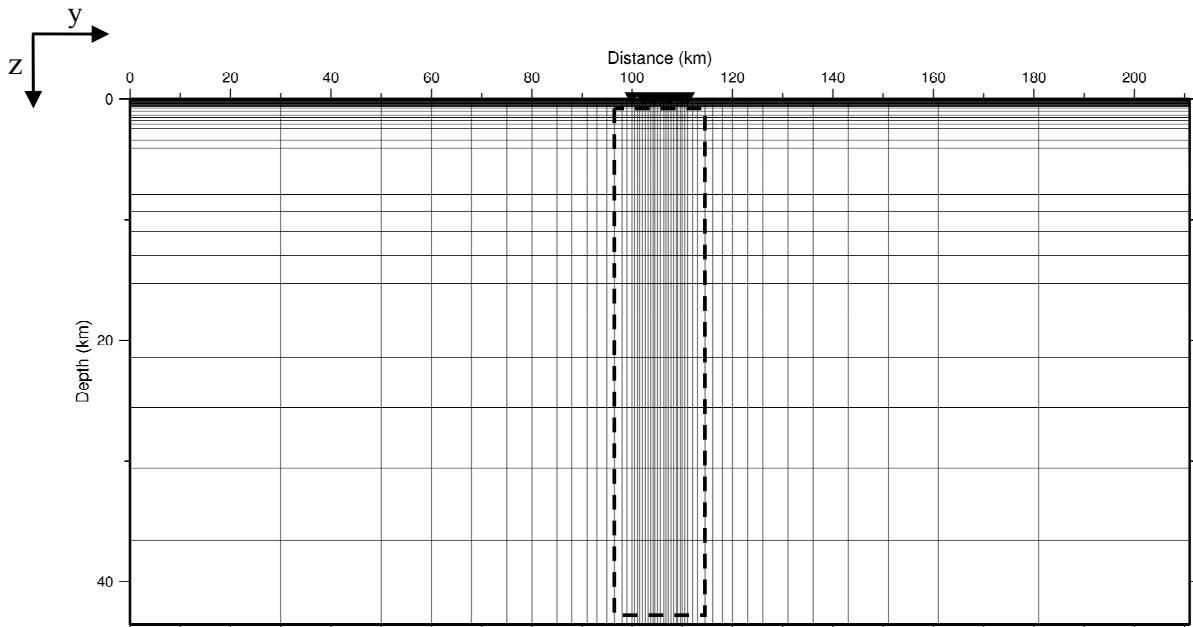

FIGURE 49: Schematic representation of 2D mesh for inversion with REBOCC. The dashed
rectangle at the centre shows the middle part of the mesh that contains MT stations

The dense middle part of the mesh which contains stations in y direction was 11 km for Profile-1 and 17 km Profile-2. The block sizes increased outward on both sides according to the general rule (Section 4.2). The block thickness z increases from 10 m for the surface layer to 200 m towards the

centre of the grid and gradually attains larger values to a total depth of 43 km (Figure 49). Apart from the 39 vertical blocks specified in the grid, REBOCC requires additional air layers. This was included in the input starting model file which also contains the initial resistivity model which could be: a half space, a 1D layered model or a 2D resistivity model. In addition, a model control file was created to account for the effect of the Atlantic Ocean on the MT soundings. In REBOCC inclusion of model control file requires having a prior model file. The resistivity of the ocean was considered to be 0.3 Ωm (Palacky, 1987) in the prior model file. The model control file allows "freezing" part of the model containing ocean layers which means that block resistivity is fixed and can't be changed during the inversion.

The actual model used extended 200 km to the NW and SE for Profile-1 and to the NE and SW of Profile-2 and included the Atlantic Ocean as a fixed feature, to allow for the effects of the highly conductive ocean on the MT measurements made onshore. The effect of the ocean on the MT measurements is discussed on many articles such as Ranganyaki and Madden (1980); Makie et al. (1988); and Eysteinsson and Hermance (1985). The bathymetric information of the Atlantic Ocean was obtained from a Bathymetric map of Norwegian-Greenland seas (Gisle and Manik, 1977). The Atlantic Ocean is about 12 km away from sounding 094 in the NW direction and 6 km from sounding 072 in the SE direction from Profile-1 (Figure 34). The Atlantic Ocean is about 5 km from sounding 068 on Profile-2 in the SW direction (Figure 34).

Two responses for apparent resistivities and phases for TE and TM mode and their corresponding errors were included for in the data file as an input to REBOCC for the two profiles. A total of 73 periods from 0.0031 to 877 s were included in the data file.

6.6.5 Results from 2D inversion of Profile-1

Profile-1 consists of 12 MT stations, each containing 73 periods. A total of 1752 data parameters were considered.

In the first case, TE mode, TM mode and combined TE and TM modes data of Profile-1 were inverted without considering the effect of the Atlantic Ocean. The starting models used for both modes were a uniform half space with a resistivity 100 Ωm.

The TE mode, TM mode and combined TE and TM modes model resistivity structure of Profile-1 show a resistive ($\geq$ 100 Ωm) surface layer, underlain by low-resistivity layer (Figures 50, 51 and 52). Below the conductive layer, high resistivity ($\geq$ 100 Ωm) is observed. This resistivity structure is similar to resistivity structure of the 1D inversion (section 33). The TM mode resistivity cross-section contains low-resistivity vertical structure in the central part below MT sites 36 and 12 which could be a modelling artefact caused by the effect of the conductive ocean (Figures 51).

In the second case, TE mode data and TM mode data of Profile-1 were inverted taking into account the effect of the ocean on the MT soundings. To achieve this, a model control file was designed to fix the resistivity of the ocean. A prior model file was also created assigning a resistivity of the ocean 0.3 Ωm. The starting model used was half space with resistivity of 100 Ωm.

The TE mode, TM mode and joint inversion of TE and TM mode models for Profile-1 (including ocean in the model) are shown in Figures 53, 54, and 55, respectively. The fit of the data and model responses are given in Appendix B. All the resistivity models show a high-resistivity surface layer, underlain by a low-resistivity (conductive) cap of variable thickness and depth followed by high-resistivity structure, resistive core. This resistivity structure from 2D inversion can be correlated to alteration mineralogy. The high-resistivity surface layer can be associated to unaltered hyaloclastites and basaltic lavas, and the conductive layer to smectite-zeolite and mixed layer clay alteration zone. The high resistivity below the low resistivity can be correlated with chlorite-epidote alteration zone down to depth of about 2.3 km.
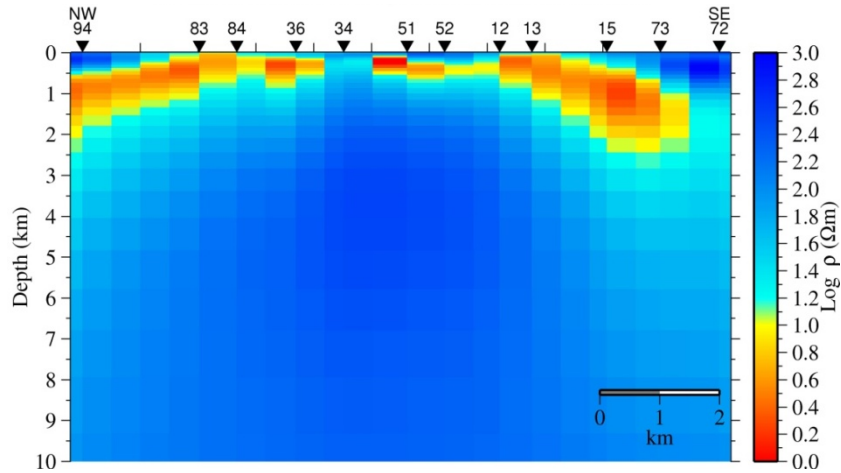
FIGURE 50: 2D model obtained by inverting the TE data for Profile-1 (not taking the ocean into account). This resistivity model was obtained after 10 iterations and RMS of 2.6
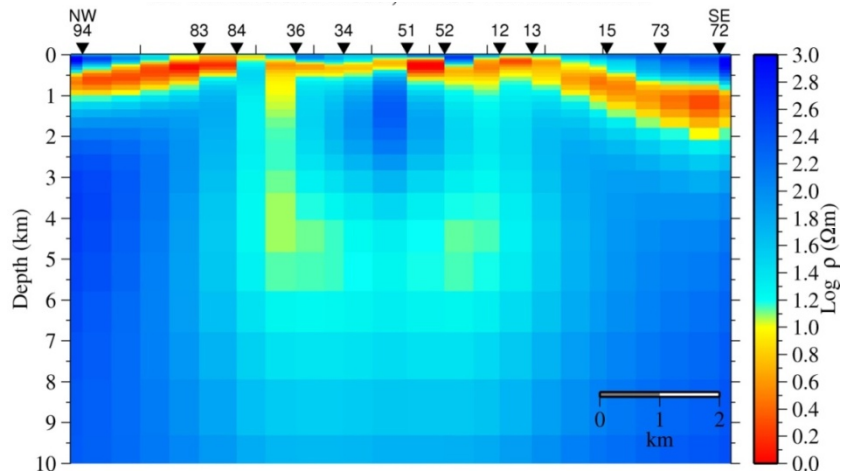

Figure 51: 2D model obtained by inverting the TM mode data for Profile-1 (not taking the ocean into account). This model was obtained after 8 iterations with RMS of 1.9
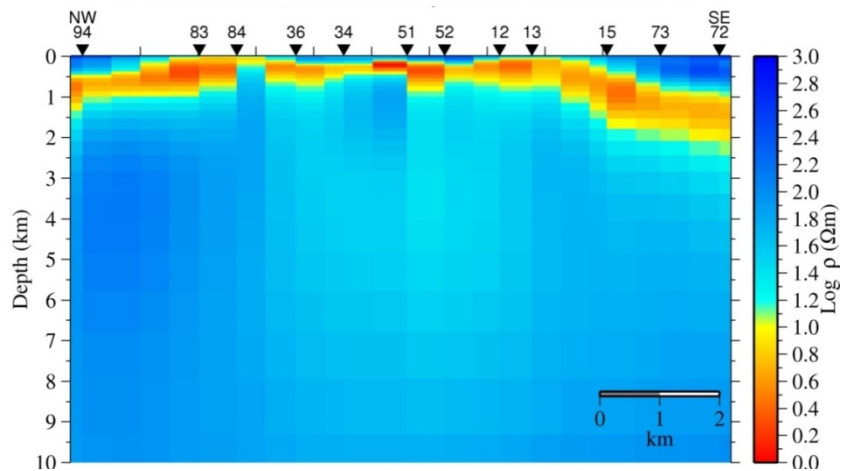

FIGURE 52: 2D model obtained by inverting the combined TE and TM mode data for Profile-1 (not taking the ocean into account). This model was obtained after 8 iterations with RMS of 3

Comparing the models of TE mode data, TM mode and joint inversion of TE and TM on Figures 50, 51, 52, 53, 54, and 55, there is no major change in the models for the case including and not including the ocean. However, low-resistivity vertical structure under and between sites 36 and 12 in Figure 51 (case without including ocean in the model) are not observed in the model in Figure 54 (case with the ocean included in the model). The result might suggest that it is necessary to include the ocean in the model to

48

remove the ocean effect. But it is not clear why the modelling artefacts are observed at the centre of the cross-section rather than under sites which are close to the ocean such as sites 73 and 72 (Figure 51).
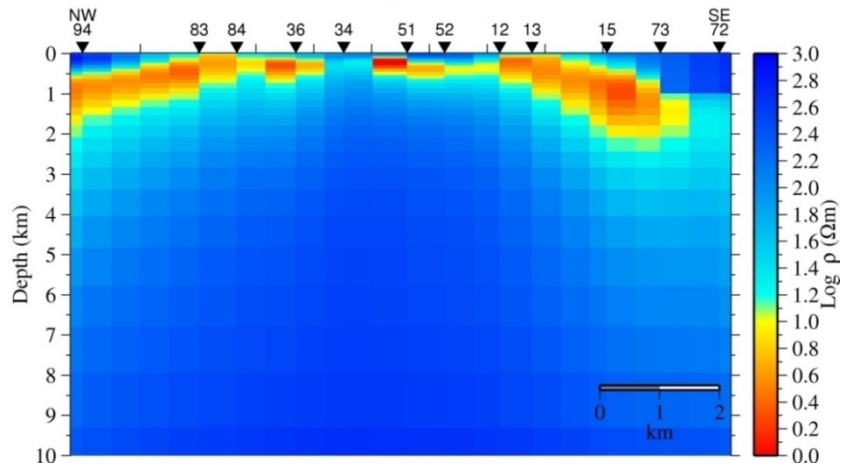

FIGURE 53: 2D model obtained by inverting the TE data from Profile-1.
This model was obtained after 10 iterations and RMS of 4
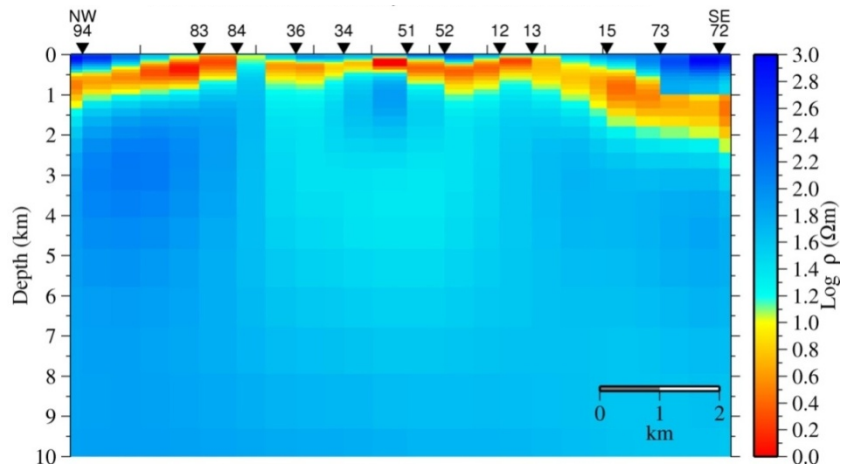

FIGURE 54: 2D model obtained by inverting the TM data from Profile-1.
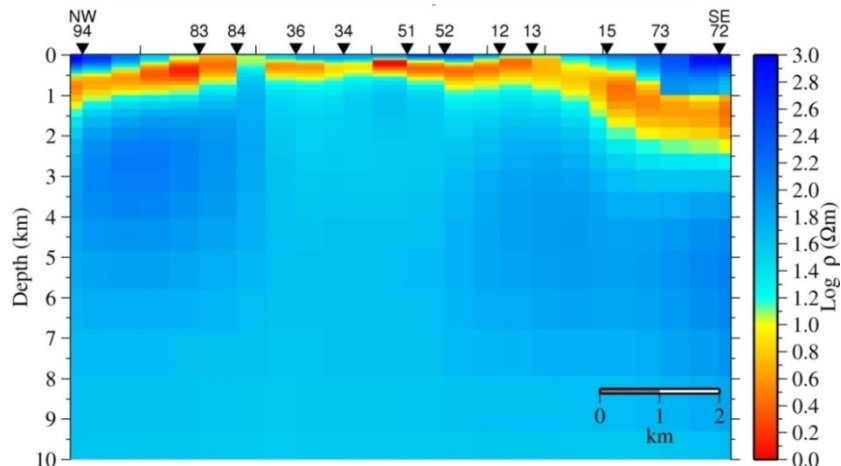This model was obtained after 7 iterations with RMS of 1.6

FIGURE 55: 2D model obtained by inverting both TE and TM mode data for Profile-1.
This model was obtained after 11 iterations with RMS of 3.4

A pseudo-section plot of observed MT data and response obtained by inverting TE and TM data for Profile-1 of the Krýsuvík geothermal field area are shown on Figures 56 and 57.
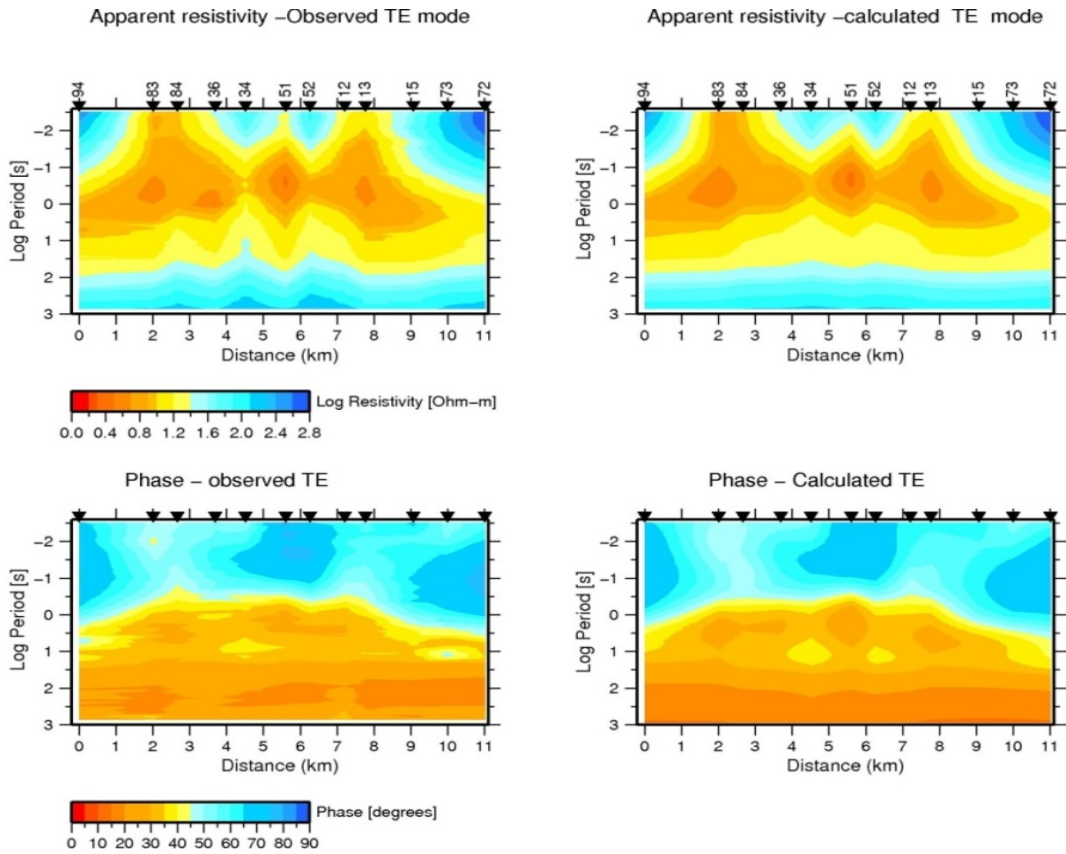
FIGURE 56: Pseudo-section plot of observed (shift corrected) and calculated
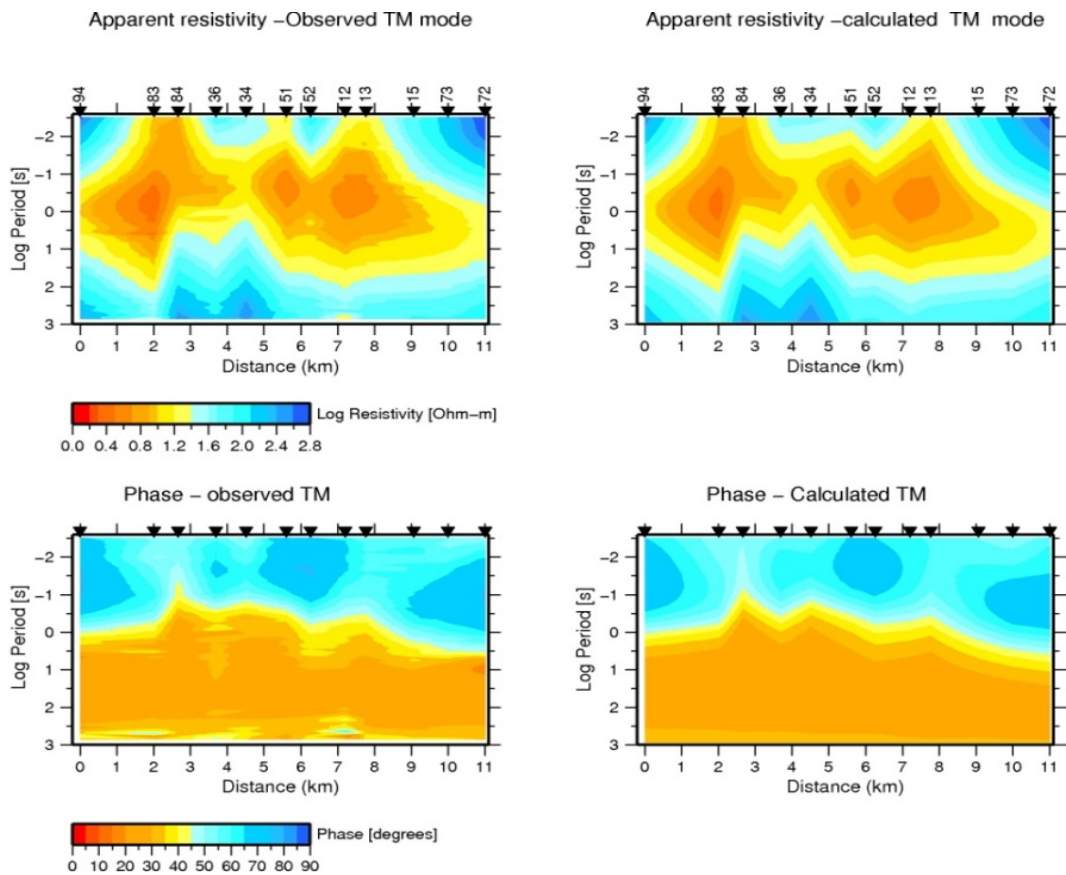apparent resistivity and phase obtained by inverting TE mode data for Profile-1

FIGURE 57: Pseudo-section plot of observed (shift corrected) and calculated
apparent resistivity and phase obtained by inverting TM mode data for Profile-1

50

From the a pseudo section plots of TE and TM modes of the observed MT data on the left panel of the Figures 56 and 57, qualitative interpretation can be made. A high-resistivity surface layer of variable thickness is observed under sites 94, 34, 52, 15, 13 and 72. Under these sites, at very short periods, decreasing apparent resistivity and high impedance phase ($> 55°$) were observed on both modes indicating a low-resistivity layer underlying high-resistivity surface layer. A low resistivity stretches (extends) to the surface from below in two locations under sites 83, 84, 36 and sites 12, 13 on both modes coincides with the location of dominant fissure swarms trending N40°E. At long periods (> 10 s) the increasing apparent resistivity and low impedance phase ($< 35°$) on both modes indicating a high resistivity underlying the low resistivity. The pseudo section plots of TE and TM modes of calculated MT responses on the right panel of Figures 57 and 58 are similar but smoother than the observed. Therefore, the pseudo section plots show that the measured data and the calculated responses are in good agreement.

6.6.6 Results from 2D inversion of Profile-2

The TE mode and TM mode data of Profile-2 were inverted taking into account the effect of the ocean on the MT soundings. To achieve this, a model control file was designed to fix the resistivity of the ocean. A prior model file was also created assigning a resistivity of the ocean 0.3 Ωm. The starting models used were half space resistivity of 50 Ωm.

The TE mode, TM mode and joint inversion of TE and TM mode models for Profile-2 are shown in Figures 58, 59, and 60, respectively. The fit of the data and model responses are given in Appendix B. All the resistivity models show a high-resistivity surface layer, underlain by a low-resistivity (conductive) cap of variable thickness followed by high-resistivity structure.
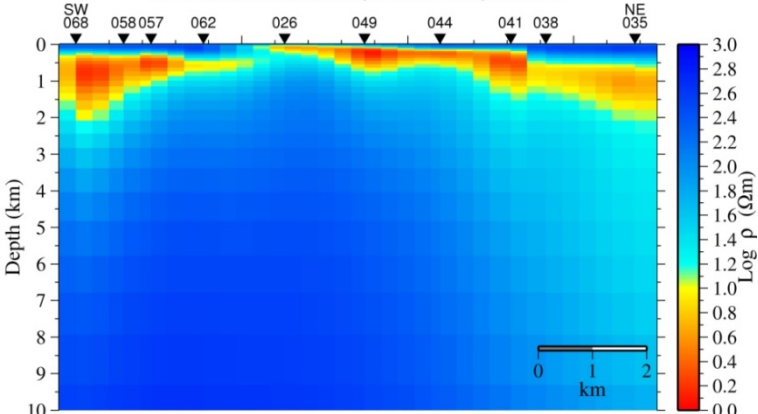

FIGURE 58: 2D model obtained by inverting the TE data for Profile-2.
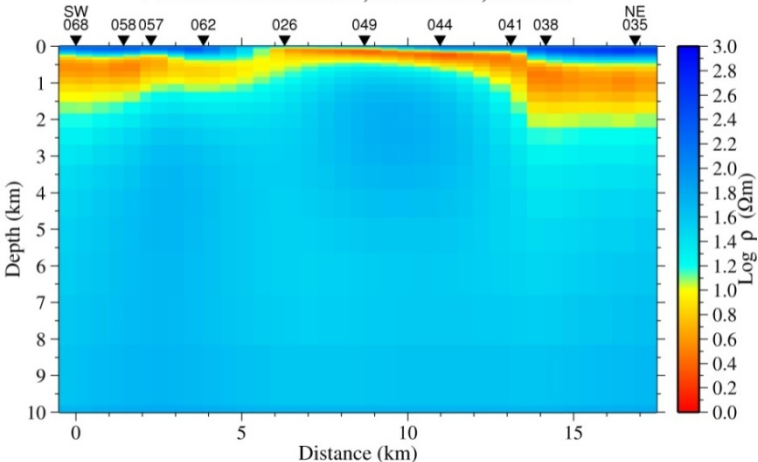This model was obtained after 7 iterations with RMS of 2.5

FIGURE 59: 2D model obtained by inverting the TM data for Profile-2.
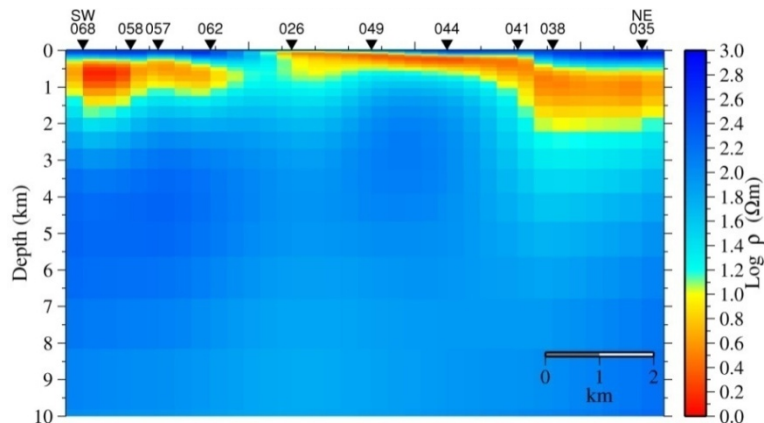This model was obtained after 9 iterations with RMS of 1.4

FIGURE 60: 2D model obtained by inverting both TE and TM modes data of Profile-2.
This model was obtained after 7 iterations with RMS of 2.4

6.6.7 Conclusions

Analysis of the polar diagrams shows that the impedances are 1D, 2D and 3D in nature across different frequencies and soundings along the two profiles. The TE and TM mode and joint inversion of TE and TM inversion models on the two profiles revealed similar resistivity structure.

Krýsuvík geothermal field is located close to the Atlantic Ocean. To account for the distortion of MT impedances because of highly conductive ocean, Atlantic Ocean was considered as a fixed feature in the model. Studies conducted by Eysteinsson and Hermance (1985) on theoretical resistivity ρ_a curves as a function of period showed the effect of the ocean at different distances from the ocean at different period range. The model calculations showed that the closer the MT sounding to the ocean, the greater its effect on the soundings. Modelling artefacts in the TM mode MT data model were removed by considering the effect of the ocean in the 2D inversion of Profile-1.

The main result from 2D inversion of Profile-1 and Profile-2 can be summarized as follows: three main resistivity layers are revealed from the 2D inversion. These are a surface layer of high resistivity (≥ 100 Ωm) of variable thickness followed by conductive layer ($\leq 15\Omega$m), underlain by a high resistivity ($>15\Omega$m). The shallow-resistivity structure of high-temperature geothermal systems in basaltic rocks in Iceland is controlled by hydrothermal alteration mineralogy (Kristmannsdóttir, 1979; Árnason et al., 2000). The surface high-resistivity layer can be correlated to unaltered basaltic lavas flows, hyaloclastites, pillow lavas and basaltic breccias. The second layer is very conductive and has variable thickness along the cross-section. This conductive layer can be associated with altered hyaloclasties, pillow lavas and basalts (smectite-zeolite or mixed layer clay alteration zone). The high resistivity below the conductive layer can be correlated chlorite-epidote alteration zone down to a depth of about 2.3 km. This high-resistivity layer below the conductive layer can be considered to be related to the reservoir of the geothermal system. The resistivity models of 2D inversion of MT data do not reveal a horizontal good conducting layer at great depth which is commonly observed in the crust beneath Iceland.

6.7 3D inversion of MT data

Since most of the MT data from Krýsuvík geothermal field show non 1D resistivity structure at long periods (xy and yx mode apparent resistivity curves show divergence), 3D inversion of the data was carried out. The 3D inversion program WSINV3DMT version 1.1.0 was used for 3D inversion of MT data (Siripunvaraporn et al., 2005). This inversion algorithm formulates the inversion problem in data space rather than the more usual model space approach (refer to Chapter 4). This approach significantly reduces the computational time required for the inversion. The 3D program assumes flat earth in the inversion.

The 3D inversion of MT data was performed for 58 MT sites at 16 periods for the full impedance tensor elements (i.e. 8 responses). The soundings were originally processed by ÍSOR staff (Hersir et al., 2010) and the appropriate EDI files used in this thesis. However, some of the soundings were reprocessed as a part of this work. The MT sites were systematically selected to uniformly cover the survey area and avoid less quality MT data sites (Figure 61). For the 3D inversion, the MT impedances were rotated to N40°E in order to minimize the influence of geological structures (faults and fissure swarms) in the survey area. The directions of x- and y- axis were 40° and 130° clockwise direction from North, respectively. For the 3D inversion four periods per decade were selected. Because of the computational cost of 3D inversion, the impedance data for the inversion was restricted to 16 periods spread over the period range 0.1064 to 149.2537 s. The 16 periods which were included for the inversion are

FIGURE 61: Location of 58 MT sites selected for 3D inversion in and round Krýsuvík geothermal field. Black dots denote MT sites

as follows: 0.1064, 0.2439, 0.4274, 0.7092, 0.9804, 1.6949, 2.8571, 3.9370, 6.8493, 11.3636, 15.8730, 27.0270, 45.4545, 74.6269, 108.6957 and 149.2537 s. This gives a total of 7427 MT data values.
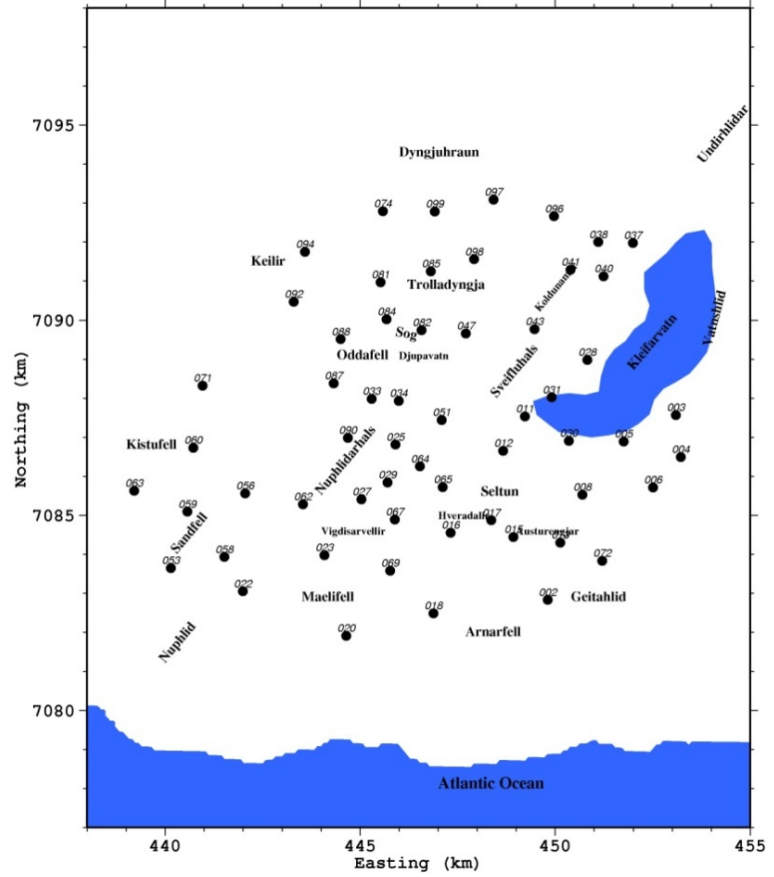
6.7.1 Static shift correction

Since the 3D inversion was performed for the MT impedance tensor, a static shift correction of the tensor elements was carried out. A static shift correction of the tensor elements is required to account for the distortion of impedance tensor mainly on the electric fields. If S_{xy} and S_{yx} are the shift multipliers for the xy and yx polarization of apparent resistivities, respectively, the shift corrected tensor Z^c is given by the following formula (Árnason et al., 2010):

$$\begin{bmatrix} Z^c_{xx} & Z^c_{xy} \\ Z^c_{yx} & Z^c_{yy} \end{bmatrix} = \begin{bmatrix} C_x & 0 \\ 0 & C_y \end{bmatrix} \begin{bmatrix} Z_{xx} & Z_{xy} \\ Z_{yx} & Z_{yy} \end{bmatrix};$$

Where,

$$C_x = \sqrt{1/S_{xy}} \; ; \; C_y = \sqrt{1/S_{yx}}$$

Static shift multipliers were determined for the xy and yx polarizations for 58 MT sites using the corresponding TEM sites. This was done by using the program TEMTD for 1D joint inversion of rotated MT data and corresponding TEM soundings from the same site. A typical result of 1D joint inversion of the xy or yx polarizations and corresponding TEM sounding is shown on Figure 62.

The static shift multipliers for xy and yx polarizations for the 58 MT sites used in the 3D inversion are plotted as a histogram as shown on Figure 63.
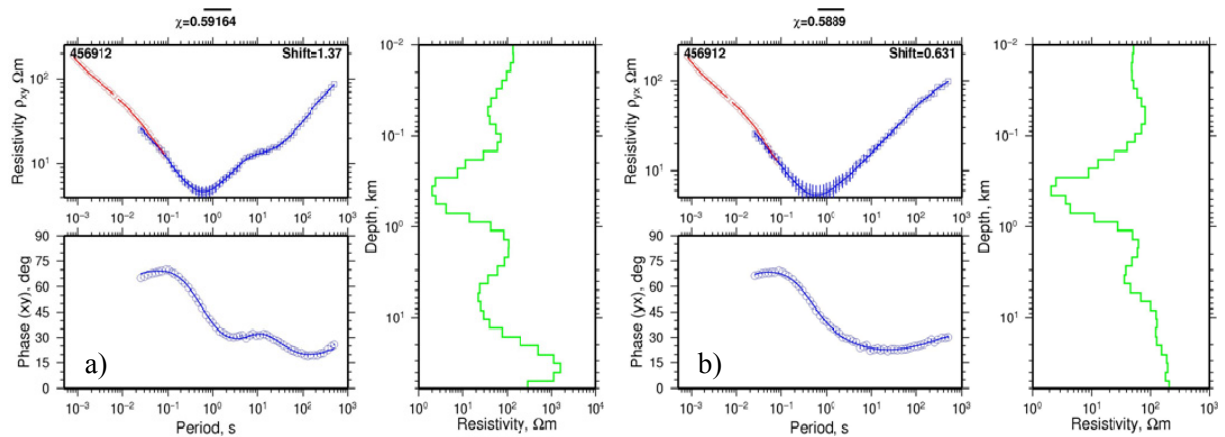
53

FIGURE 62: 1D joint inversion of the a) xy and b) yx polarizations and TEM sounding
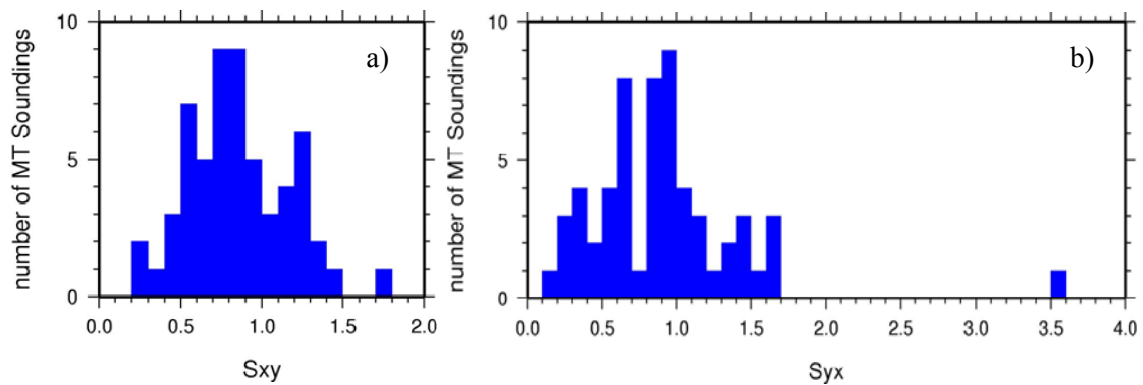in order to determine static shift of MT data

FIGURE 63: A histogram of shift multipliers Sxy and Syx for the 58 MT sites used in 3D MT
inversion. Both (a) and (b) show a wide range of static shift multipliers from 0.1 to 3.5

6.7.2 3D model mesh design

It is critical when building a 3D model that the mesh is designed as accurately as possible, which requires small block sizes. On the other hand, the total number of cells should be as small as possible so that we can obtain a solution in reasonable amount of time and without requiring a super computer.

The finite difference model mesh used for the 3D inversion has a dimension of 39 x 39 x 28 in x, y, and z directions. The central part of the model discretization was uniform, with a cell width of 1 km for 17 x 17 grid squares in x and y directions on the surface. The model mesh first layer in z direction is 50 m and was increased by 1.2 times overlying block size to a total depth of about 42.1 km. Site positions were adjusted slightly so that sites are located at the centre of a cell on the surface, as required by the version of WSINV3DMT code used (Figure 64). The total original number of model parameters used is 42588. Since part of the model was taken as a fixed feature to account for the ocean, the total number of model parameters used in the inversion was 38418. The computer memory required for this model run was ~ 3.2GB.

Since Krýsuvík geothermal field is surrounded by the Atlantic Ocean, the effect of the ocean was taken into account during the inversion. A model control file was designed so as to "freeze" part of the model mesh where the ocean is considered as fixed feature during the inversion. In the model control file a simplified coastline with straight line was assumed. The coastline is about 13 km in the North West, 7 km in the South East and 4 km in the South West away from the model co-ordinate system. The maximum ocean floor topography of 100 m in the North West, 300 m in the south West and 1000 m in the South East direction from survey area was used as obtained from Bathymetric map of Norwegian-Greenland seas (Gisle and Manik, 1977). The resistivity of the ocean was considered to be 0.3 Ωm in the starting model file.

54

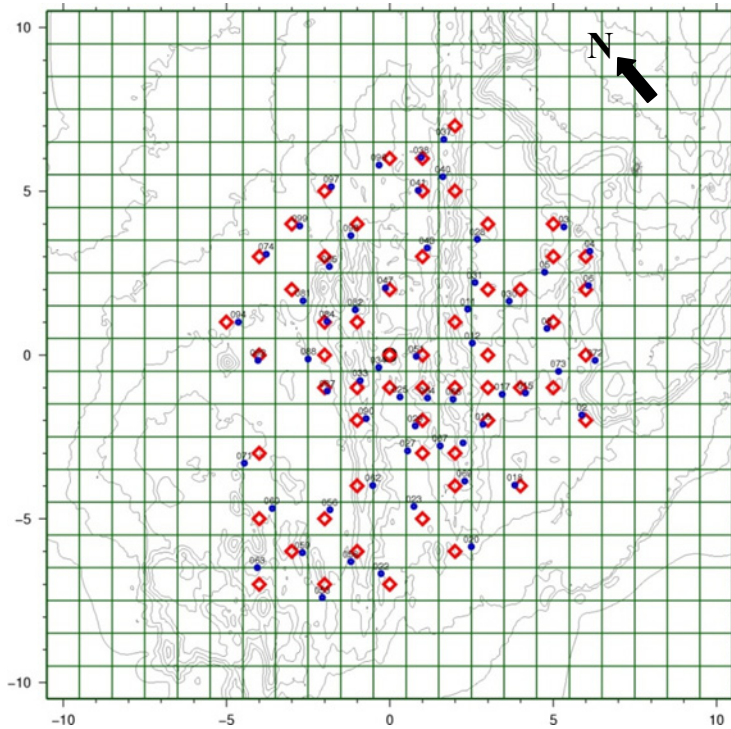## 6.7.3 Sensitivity test of mesh discretization and starting models

Forward modelling solutions depend significantly on the mesh grid discretization used. This also affects the 3D inversion results. In order to compare the resulting model of the inversion with the first mesh grid (fine mesh grid) described in the model mesh design section above, a second model mesh (coarse mesh grid) of dimensions 39 x 39 x 23 in x- , y- and z- directions was considered. These two model meshes have similar widths of blocks in x- and y- directions on the surface. The vertical grid discretizations of the two mesh grids were different. The second mesh grid (i.e. 39 x 39 x 23) block sizes in z- direction were the following: 100, 200, 200, 200, 200, 200, 500, 500, 500, 500, 800, 800, 1000, 1000, 2000, 2000, 3000, 3000, 5000, 8000, 10000, 15000, 20000, 30000. The second mesh grid is coarser than the first mesh grid in z- direction.

FIGURE 64: Location of MT sites in the central part of the 3D model grid on the surface (x-y direction). The grid squares are 1km x 1km in dimension. The MT sites are shown as blue circles. The red diamonds show MT site positions adjusted slightly so that the sites are located at the centre of the grid on the surface, as required by the version of WSINV3DMT code used. The impedance tensors used for the 3D inversion were rotated from geographic north to the geologic strike of N40°E

The 3D inversion of the 58 MT sites was carried out using these two mesh grids. The starting model was a homogeneous half space of 50 Ωm. The resulting 3D resistivity models after 5 iterations from the first mesh grid (fine mesh grid) with normalized RMS of 1.9 and second mesh grid (coarse mesh grid) after 5 iterations with normalized RMS of 1.9 , respectively, is shown in Figure 65.

The resistivity depth slice from the 3D inversion at a depth of 1000 m in Figure 65a for the fine mesh grid shows similar resistivity structure at the same depth as the coarse mesh grid in Figure 65b. The resistivity depth slices at depth 2850 m for the fine mesh grid and the coarse mesh grid in Figure 65c and d, respectively, show a low-resistivity anomaly at the central part of the resistivity models. But the location and trend of the low-resistivity anomaly is different for the two mesh grids used. Since the inversion code WSINV3DMT uses finite difference (FD) method for the forward modelling and calculates the electric and magnetic fields on the surface, the result depends on grid discretization. A finer mesh generally yields higher accuracy, but at the cost of long computing time and large memory requirement (Pellerin et al., 1996; Siripunvaraporn et al., 2002). Therefore, the finer mesh grid is used for the 3D inversion.

Two starting models were tested on the fine mesh grid. Firstly, a homogeneous half space of 50 Ωm and secondly a three layer earth model consisting of three layers (400 Ωm, 5 Ωm and 100 Ωm). The resulting 3D resistivity models after 5 iterations with RMS of 1.9 and after 7 iterations with RMS of 1.9 is shown in Figure 66, for the two starting models, respectively.

The resistivity model slices at depths of 600 m and 3500 m using homogeneous half space as starting model are shown in Figure 66a and e, respectively. The resistivity model slice at similar depths using the three layered earth as starting model are shown in Figure 66b and f. They show similar resistivity structures at their respective depths. The depth slice at a depth of 1000 m below the surface using

homogeneous half space and three layered earth model as starting model are shown in Figure 66c and d, respectively. They show different resistivity structure at the margins of the model depth slices. The layered earth starting model gave relatively higher resistivity as compared to half space at the margins of the depth slice. The inversion program uses the starting model as prior model if prior (base) model is not given. The inversion program searches for a new model around this prior model (starting model) after every iteration and tries to fit the data. Therefore, the sensitivity test of the two starting models shows that the difference in the resulting resistivity structure is minor.
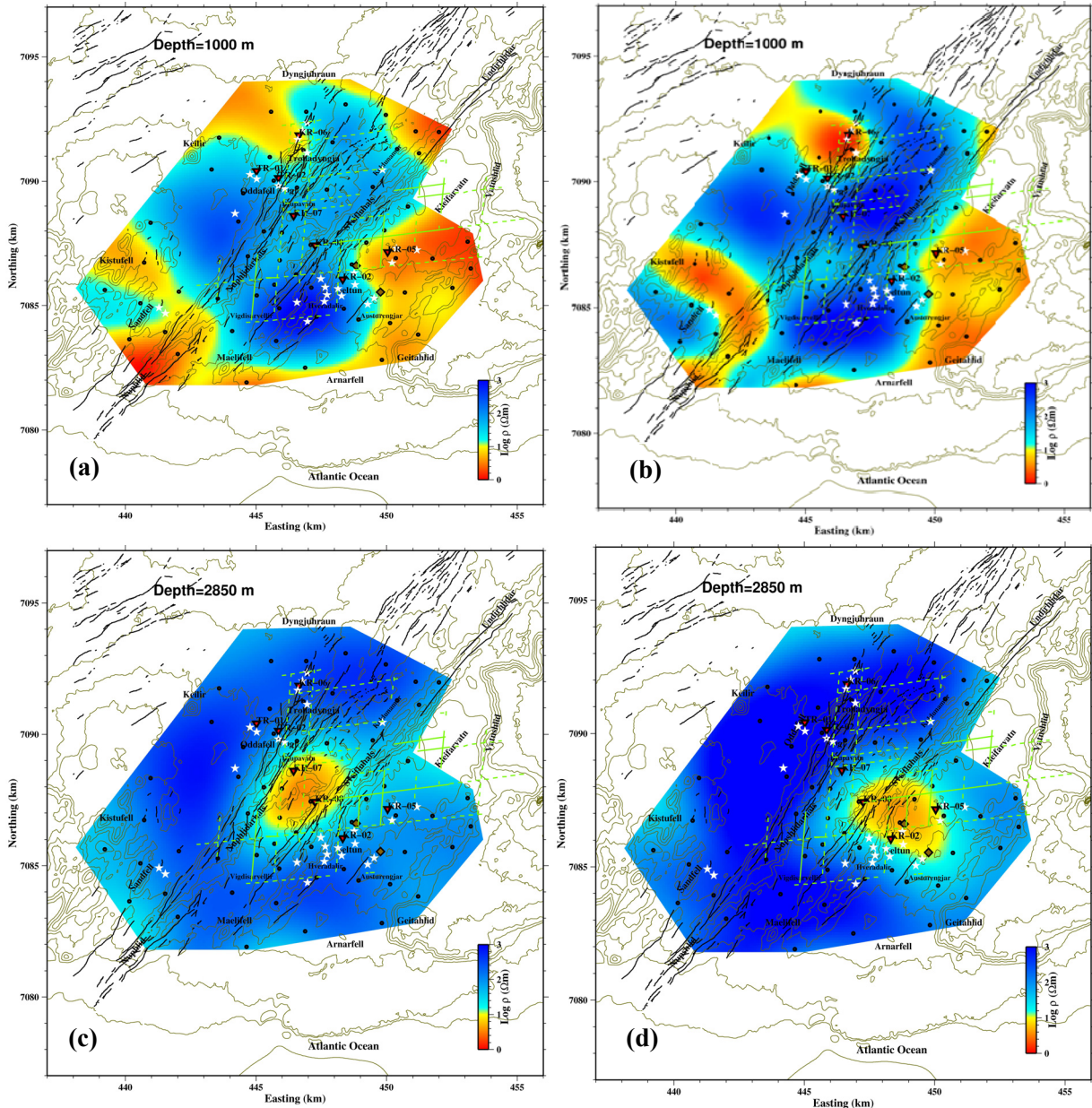
FIGURE 65: Smoothed resistivity slices at depths of 1000 m and 2850 m using a homogeneous half space of 50 Ωm (a) and (c) for the fine mesh grid (i.e. 39 x 39 x 28) and (b) and (d) for the coarse mesh grid (i.e. 39 x 39 x 23) from inversion of data from the 58 sites
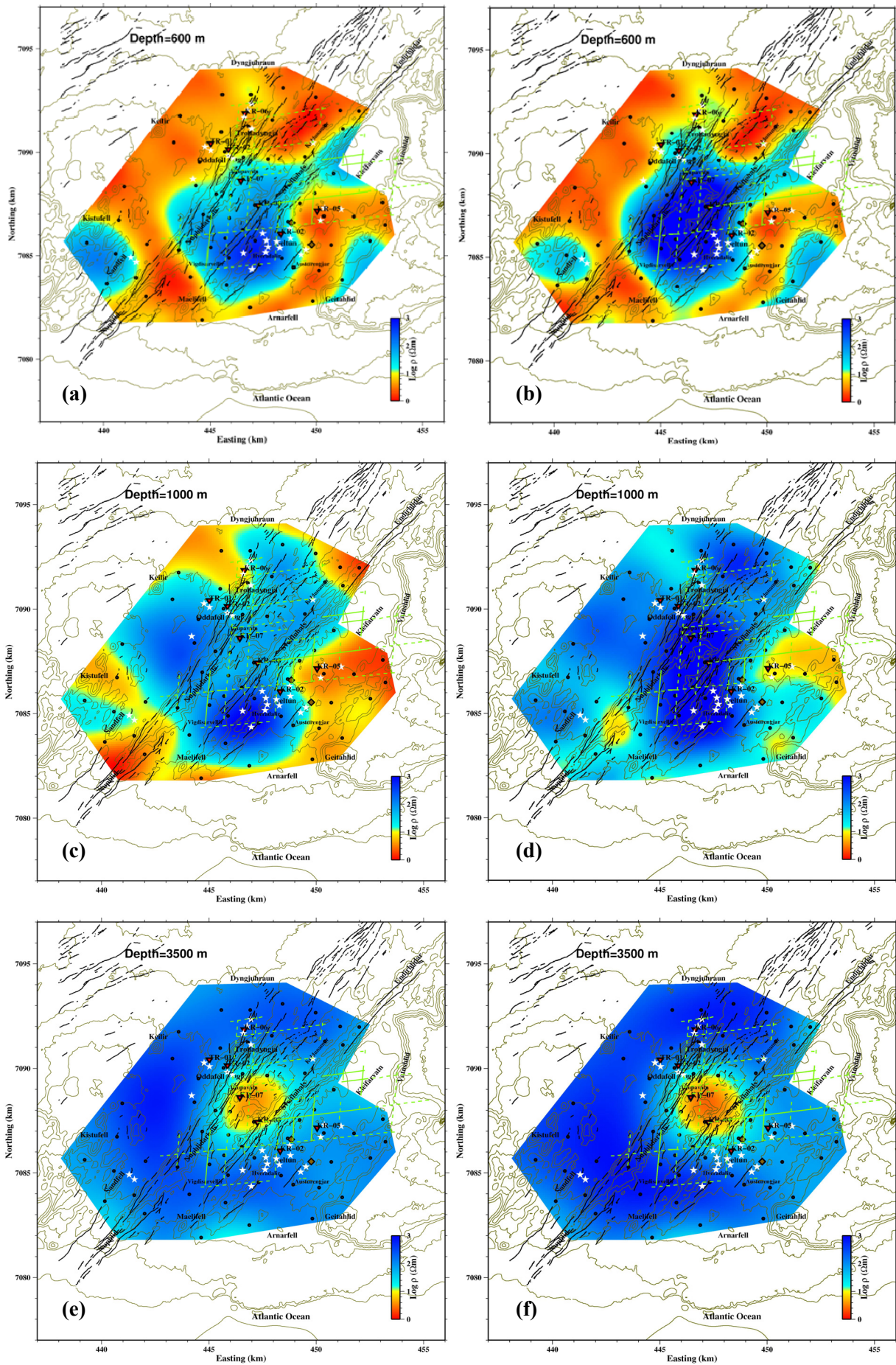
FIGURE 66: Resistivity slices at a depth of 600 m, 1000 m and 3500 m using a starting model of homogeneous half space of 50 Ωm as shown in (a), (c) and (e) and three layer earth model as shown in (b), (d) and (f) from inversion of MT data from the 58 sites

6.7.4 Results of 3D inversion

The 3D inversion result using the fine mesh grid and homogeneous half space of 50 Ωm as starting model will be discussed here. The 3D inversion reached a normalized RMS of 1.9 after five iteration and 150 hours of continuous computational time with Intel Xeon computer with 3.6 GB memory and 2.83 GHZ speed. In the 3D inversions models considered here, topography is not included.

The central part of the smoothed resistivity model resulting from 3D inversion is shown on Figure 67a-g, as horizontal slices at seven different depths. Also included in the Figure are geothermal surface manifestations (Saemundsson et al., 2010) and faults inferred from seismicity (Magnússon and Árnason, 2002). The fits of the data and the response for the 3D inversion from the 58 MT sites is given in Appendix C for xy and yx resistivity and phase.
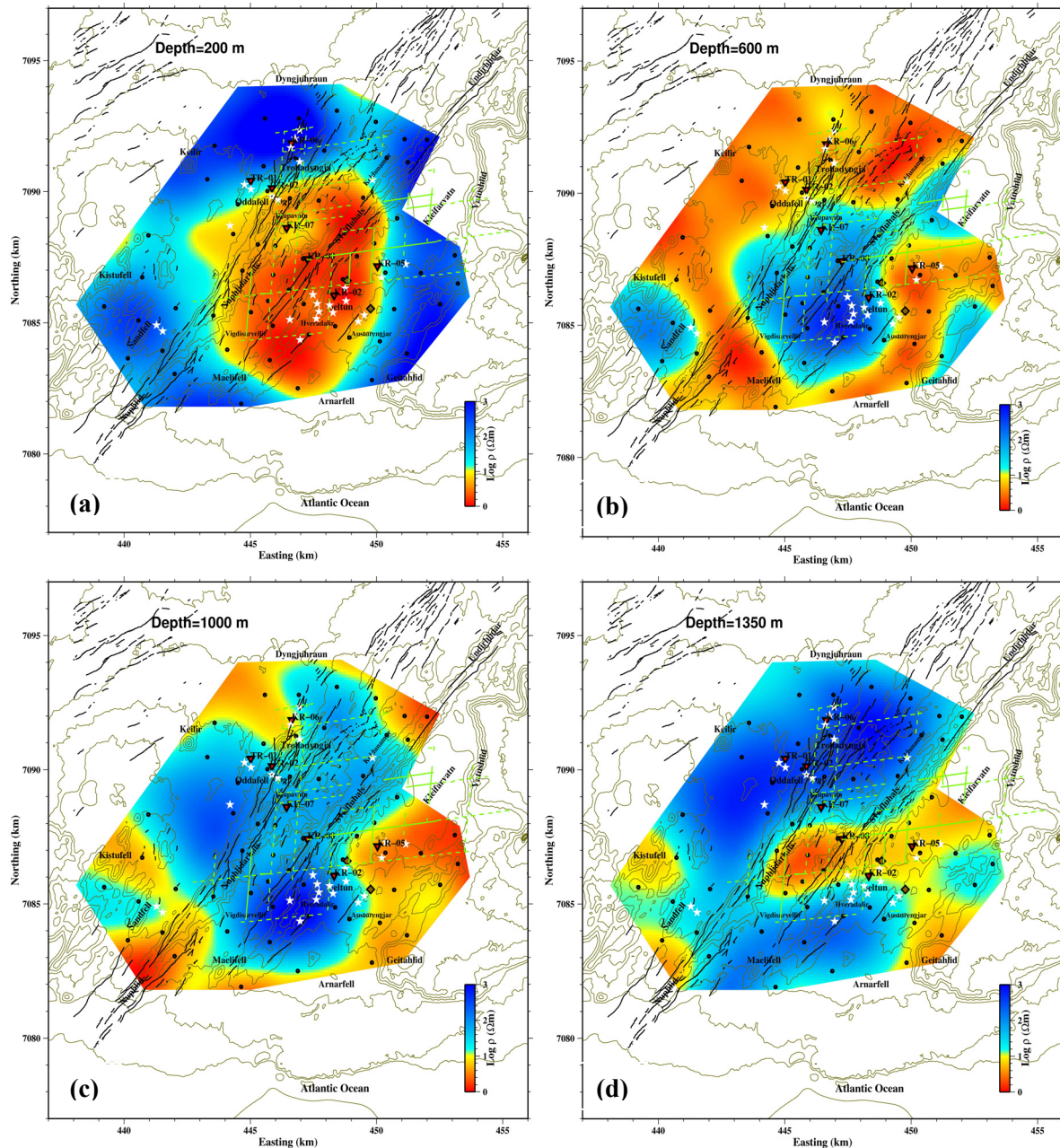

FIGURE 67: Resistivity from 3D inversion at seven depths derived from inversion of the 58 MT sites: i.e. (a) at 0.2 km depth; (b) at 0.6 km depth; (c) at 1 km depth; (d) at 1.35 km depth ; (e) at 2.85 km depth; (f) at 5.2 km depth; and (g) at 9.7 km depth. White star = boiling springs; Golden diamonds = hot springs; Black dots = MT sites; Inverted triangles = geothermal wells; Black lines = faults and fissures mapped on the surface; Green lines = faults inferred from seismicity; thin black curved lines = topographic contour lines in m a.s.l.

At a depth of 0.2 km, the model shows a broad low-resistivity zone (≤15 Ωm) at the central part of the slice (Figure 67a). The low-resistivity zone includes the area between Oddafell and Austurengjar in the NW-SE direction and Köldunámur-Maelifell in the NE-SW direction. This broad low-resistivity zone contains geothermal areas such as Sog and Seltún-Hveradalir (Figure 67a). This broad low-resistivity zone is presumably correlated to zeolite-smectite or mixed layer clay alteration of hyaloclastites, pillow lavas and basaltic breccias in the area. The region outside the central low-resistivity zone shows high resistivity (> 15 Ωm) (Figure 67a). This high-resistivity zone could be associated with unaltered rocks.

At a depth of 0.6 km, the model shows the replacement of the broad low-resistivity zone observed in the central part of the slice at a depth of 0.2 km below the surface by a high-resistivity zone (> 15 Ωm) (Figure 67b). This high-resistivity zone could be associated with high-temperature alteration (chlorite-epidote zone). The geothermal areas of Sog, Seltún-Hveradalir and Sandfell are within this high-resistivity zone. Almost all the region surrounding the central high resistivity at a depth of 0.6 km is characterized by low resistivity (≤ 15 Ωm) (Figure 67b). The low-resistivity zone is most likely correlated to smectite-zeolite alteration.
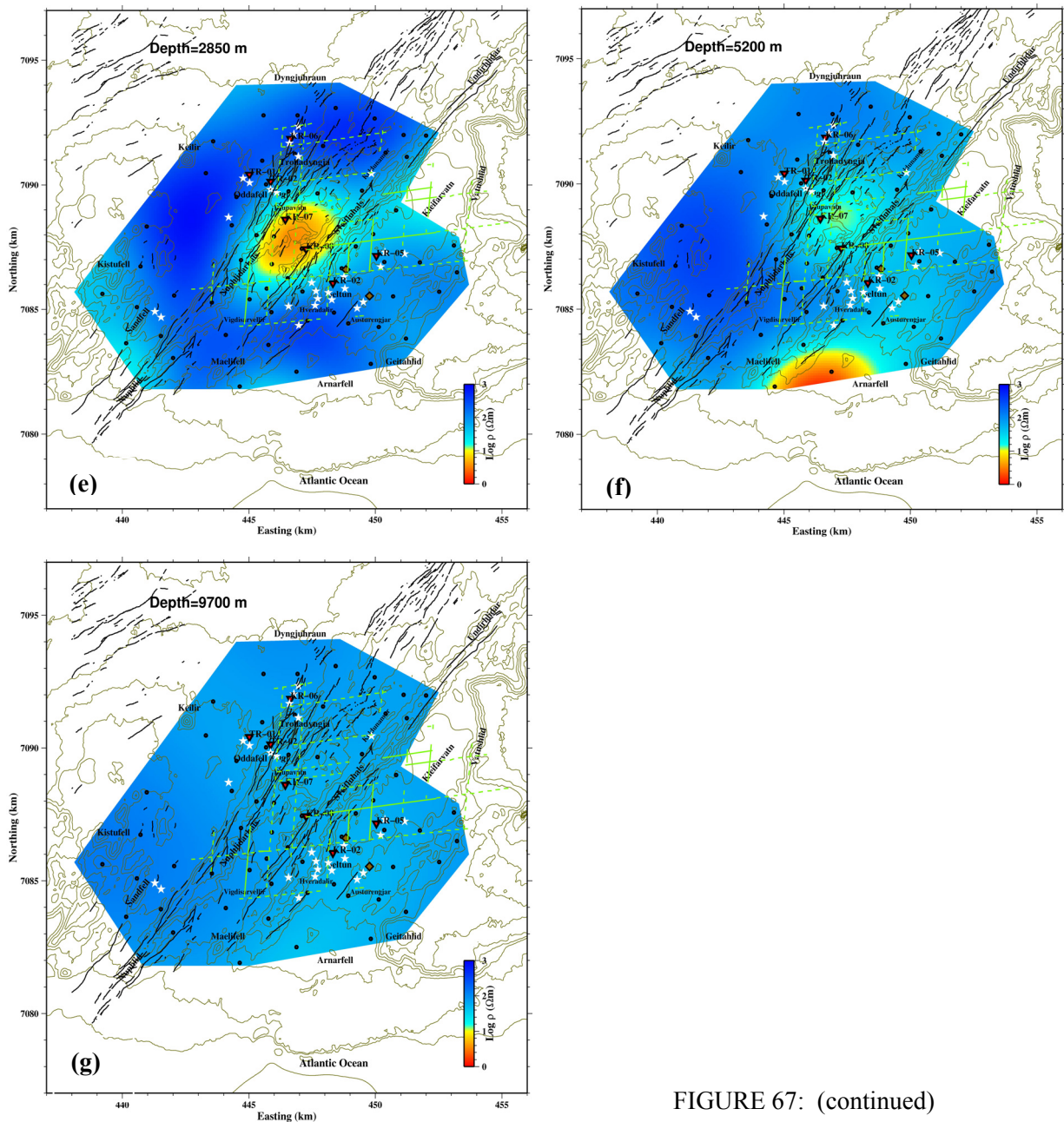

FIGURE 67: (continued)

59

At a depth of 1 km, the high resistivity (> 15 Ωm) observed in the central part of the slice at 0.6 km depth is broadening (Figure 67c). The anomaly includes Trölladyngja-Sog, Hveradalir-Seltún, Köldunámur and Sandfell. This high resistivity is presumably correlated to high-temperature alteration (chlorite-epidote alteration). The outer margin of the depth slice is characterized by low resistivity (≤ 15 Ωm) (Figure 67c).

At a depth of 1.35 km, a low-resistivity (≤ 15 Ωm) zone covers the area SW of Lake Kleifarvatn crossing the Sveifluháls hyaloclastite ridge and ending at Núphlídarháls hyaloclastite ridge (trending ENE to WSW direction) (Figure 67d). This low-resistivity anomaly coincides with trend of the transform faults inferred from seismicity shown as green lines in Figure 67d (Magnússon and Árnason, 2002). The nature of this low resistivity which is overlain by high resistivity is not known. The rest of the slice is almost characterized by high resistivity (> 15 Ωm) except spots near Kistufell and south of Sandfell (Figure 67d).

At a depth of 2.85 km, a low-resistivity zone is confined between the two hyaloclastites ridges (Núphlídarháls and Sveifluháls ridges). The low-resistivity zone is located between north west of Seltún area and south east of Djúpavatn explosion crater (Figure 67e). The low-resistivity structure may be associated with the heat source of the Krýsuvík geothermal system. The rest of the resistivity depth slice shows high resistivity (> 15 Ωm).

At a depth of 5.2 km, the narrow low-resistivity zone observed at a depth of 2.85 km has almost disappeared (Figure f). A high resistivity (> 15 Ωm) characterizes the entire depth slice except a spot north west of Arnarfell (Figure 67f). The low-resistivity spot north west of Arnarfell could be correlated to intrusion of the sea water into land.

At a depth of 9.7 km, the 3D resistivity model depth slice shows a high resistivity on the entire depth slice (>15 Ωm) (Figure 67g).

The resistivity model resulting from 3D inversion is also presented as vertical cross-sections along the x-axis (i.e. N40°E) and y-axis in the model coordinates system. Figure 68 shows the location of the cross-sections labelled by their x-coordinates (NW-SE) and their y-coordinates (SW-NE) cross-sections in the model coordinate system. The vertical resistivity cross-sections along y-coordinates and x-coordinates are shown in Figures 69 and 70, respectively.

The six vertical resistivity cross-sections in Figure 69 show three main resistivity layers: high-resistivity surface layer (>100 Ωm) underlain by low-resistivity layer (<15 Ωm) followed by high resistivity (>15 Ωm). All the six cross-sections in Figure 69 show variable thickness of the low-resistivity layer across the cross-section. The low-resistivity layer is thinner and shallower in the central part of the cross-sections as shown in Figure 69b, c, d, and e. The low-resistivity layer most likely is associated with smectite or mixed layer clay alteration. Within the high-resistivity bottom layer, a
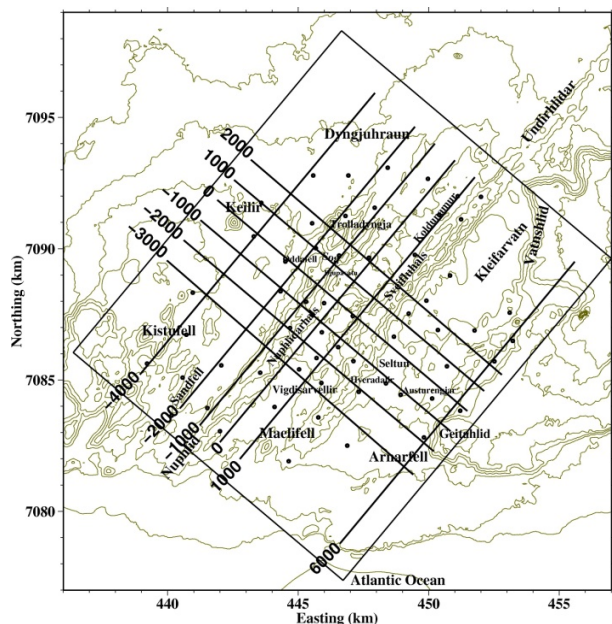

FIGURE 68: Location of the vertical resistivity cross-sections shown in Figures 6.41 and 6.42. Black dots: MT sites; thin black curved lines: topographic contour lines in m a.s.l.

conductive body of variable size is observed in the central part of the vertical cross-sections in Figure 69b, c, d, and e. The cross-section in Figure 69f inserted spurious structures of the conductive layer at the margins of the cross-section where there are no MT sites.
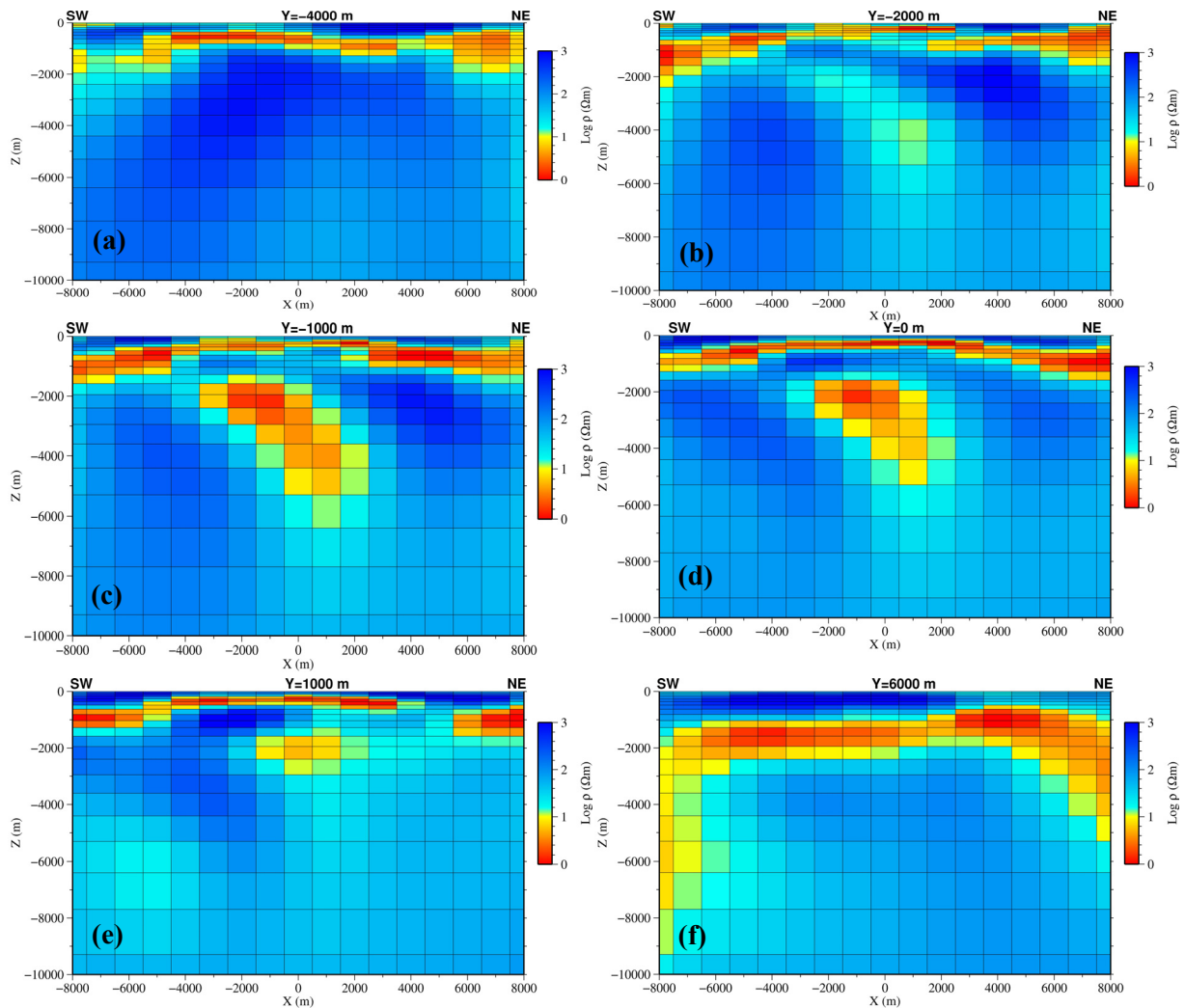
FIGURE 69: Vertical (SW-NE) resistivity cross-sections across the model y-coordinate system (location is shown in Figure 6.40): (a) at Y= -4000 m (b) at Y= -2000 m (c) at Y= -1000 m (d) at Y= 0 m (e) at Y=1000 m and (f) at Y= 6000 m

The vertical resistivity cross-sections in Figure 70 show three main resistivity layers down to a total depth of 10 km from the surface: surface high-resistivity layer (>100 Ωm) underlain by a low-resistivity layer (< 15 Ωm) followed by high resistivity (> 15 Ωm) similar to sections shown in Figure 69. All the vertical resistivity sections in Figure 70 show variable thickness and depth to the good conductor across the cross-section. The low-resistivity layer is thinner and shallower at the central part as compared to the margins of the cross-sections. Within the high resistivity below the shallow low resistivity, a low-resistivity body of variable size is embedded at a depth of about 2 km and extends up to 5.2 km from the surface as shown on Figure 70c, d, e and f.
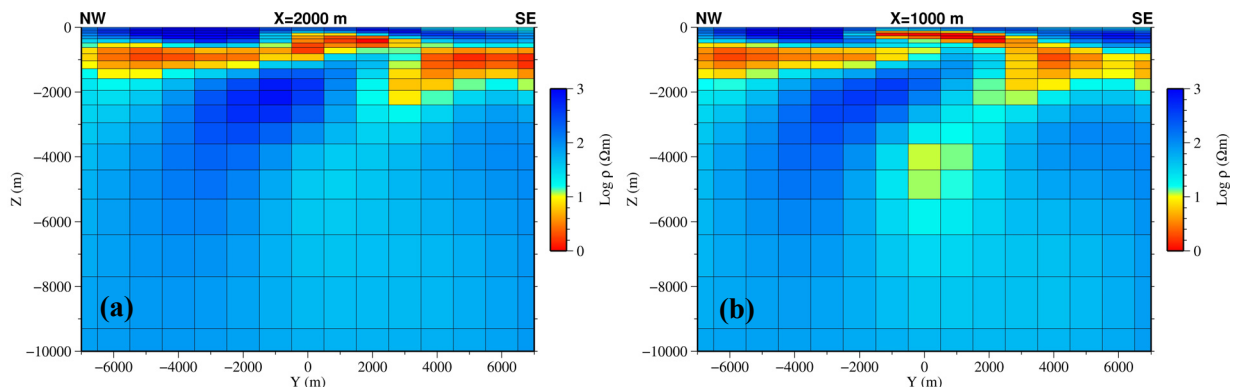

FIGURE 70: Vertical (NW-SE) resistivity cross-sections across the model x-coordinate system (location is shown in Figure 6.40): (a) at X= 2000 m (b) at X= 1000 m (c) at X= 0 m (d) at X= -100 0 m (e) at X=- -2000 m and (f) at X= -3000 m
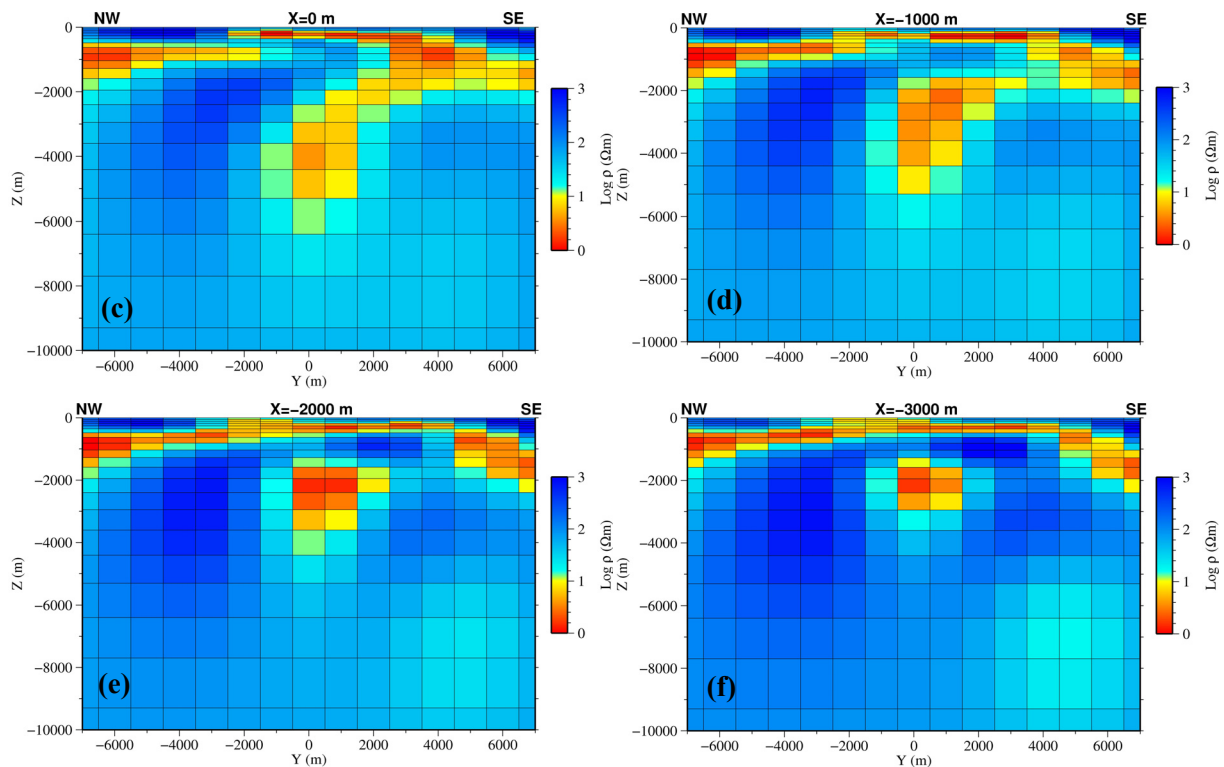
FIGURE 70: (continued)

6.7.5 Discussion of 3D inversion

The 3D MT inversion of the full impedance tensor for the 58 MT sites and 16 periods revealed the main parts of the subsurface resistivity structures at Krýsuvík geothermal field.

The resistivity model depth slices in Figure 67 and vertical cross-sections (Figures 69 and 70) showed a typical resistivity structure for high-temperature geothermal fields in Iceland, i.e. a low-resistivity cap underlain by a resistive core which presumably is related to the geothermal reservoir (Flóvenz et al., 1985; Árnason et al., 1987; Eysteinsson et al., 1994; Árnason et al., 2000).

The resistivity model slice at a depth of 1.35 km in Figure 67d shows a low-resistivity zone which is trending ENE–WSW and has similar direction as the transform faults inferred from seismicity by Magnússon and Árnason (2002) (shown as green lines in Figure 67). This low-resistivity structure might be associated with region of high fracture permeability and high temperature.

A low-resistivity anomaly is observed at a depth of about 2 km reaching down to about 5.2 km, between the two hyaloclastite ridges (Figures 67, 69, 70). There are mainly three possible sources for crustal conductive zones. These are water, magma, and conductive minerals such as graphite (Jiracek et al., 1995). The deep low-resistivity region observed at a depth of about 2 km could be associated with presence of partial melt or water trapped at depth. About 12% of the volume of Lake Kleifarvatn drained down through the upper crust at an average rate of 2 m³/s during the 18 months following 17th June, 2000 earthquake (Clifton et al., 2003). The water drained through NE to NNE-trending open fissures visible at the surface controlled by a concealed NS-trending dextral fault bounding the lake (Clifton et al., 2003). There is a possibility that this water is trapped at depth in the crust by capping mechanism. If the trapped water is below the critical temperature, it could act as a conductive zone. The other possibility could be a partially molten body, which may be associated to the heat source of the geothermal system. There is ongoing inflation (starting from September 2009-to date) taking place in the area between SW of Lake Kleifarvatn and Núphlídarháls fault observed by InSAR measurements (personal communication with Páll Einarsson). This may be related to upward movement and accumulation of molten magmatic body in Krýsuvík area. Therefore, this implies that the conductive zone may be associated with the partially molten body (heat source) rather than trapped

water. Similar deep conductive body was observed at about 3 km depth in Hengill area from 3D inversion of MT data (Árnason et al., 2010). The nature of the deep conductive zone in Hengill area is not clear (no sign of S-wave attenuation under the area), but one plausible interpretation of this high conductivity could be magmatic brine trapped in ductile intrusive rocks (Árnason et al., 2010). The Krýsuvík area is characterized by seismicity (Keiding et al., 2009). The earthquakes are mainly located at 2-9 km depth (Keiding et al., 2009). The shallowest earthquakes during 1997-2006 are located in the central Krýsuvík area, where considerable geothermal alteration is observed at the surface (Keiding et al., 2009). This increased seismic activity might be related to upward movement of molten magmatic material.

The vertical resistivity cross-sections which are located at the central part of the model mesh with high geothermal surface activity (surface alteration) as in Figure 69b-e (for location see Figure 70) reveal the low-resistivity cap rock at shallow depth as compared to the cross-sections far away from the central part in the model coordinate system as in Figure 69a and f. This shows the high degree of clay alteration in the central part of the modelled area because of the geothermal activity.

6.8 Comparison of 1D, 2D and 3D results

1D inversion of MT data for the determinant of the impedance tensor was discussed in section 6.5. When plotting 1D model cross-sections, topography was taken into account. 2D and 3D inversion of MT data were considered in sections 6.6 and 6.7. When plotting 2D and 3D model cross-sections, topography was not included. Since elevation of Krýsuvík area and its surroundings are about 100- 200 m on average (with exception of the two hyaloclastite ridges in the area), the 1D and 2D inversion results on the two profiles discussed in sections 6.5 and 6.6 can be compared to the corresponding 3D MT inversion vertical cross-sections. The 2D inversion model presented here is the joint inversion model of TE and TM mode, as it may give complete geoelectric information (Berdichevsky et al., 1995).

The 1D and 2D resistivity vertical cross-sections of Profile-1 and the corresponding 3D inversion vertical cross-section are given in Figure 71.

The 3D resistivity cross-section in Figure 71c shows similar resistivity structure as the 1D inversion model and the 2D resistivity cross-sections as shown in Figure 71a and b, respectively. All the three models show a three layer resistivity structure down to a total depth of 10 km, i.e. a high-resistivity layer (>100 Ωm) underlain by low-resistivity layer (<15 Ωm) followed by high resistivity (>15 Ωm). The main difference between 1D, 2D and 3D inversion vertical cross-sections for Profile-1 is the presence of a low-resistivity anomaly (<15 Ωm) embedded at a depth of about 2 km and extending down to 5 km below surface within the high resistivity in the 3D vertical cross-section (Figure
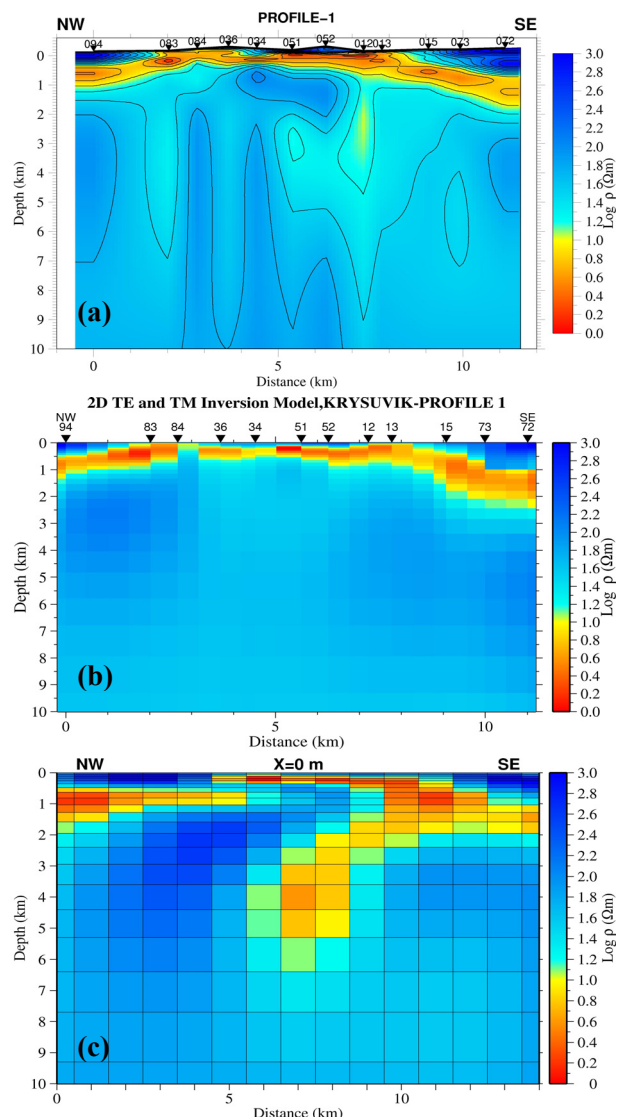

FIGURE 71: Comparison of 1D, 2D and 3D vertical resistivity cross-sections for Profile-1: (a) cross-section from joint 1D inversion of TEM and determinant MT data. (b) 2D cross-section obtained by inverting jointly TE and TM mode MT data. (c) 3D cross-section across the model at X = 0 corresponding to Profile-1

71c). Surprisingly there is an indication of the embedded low-resistivity body in the 1D inversion model under sites 12 and 13.

In a similar manner, 1D, 2D, and 3D resistivity vertical cross-sections of Profile-2 can be compared. The 1D and 2D resistivity cross-sections of Profile-2 and the corresponding 3D inversion vertical cross-section are given in Figure 72.

The 3D vertical resistivity cross-section in Figure 72c shows similar resistivity structure as the 1D inversion model and the 2D resistivity model as shown in Figure 72a and b, respectively. All the resistivity models show a three layer resistivity structure down to a total depth of 10 km. The 3D resistivity cross-section in Figure 72c reveals an additional resistivity structure not resolved by 1D and 2D inversion, i.e. a low-resistivity anomaly (<15 Ωm) embedded at a depth of 2 km at central part of the 3D resistivity cross-section.

6.9 Conclusions

The 1D and 2D inversion of MT data on the two profiles from Krýsuvík geothermal field and its surroundings revealed the main resistivity structures in the area. The 3D inversion of the 58 MT sites for the full impedance tensor elements and 16 periods helped to acquire additional information on the resistivity structure of the area.

The shallow resistivity structure of high-temperature geothermal systems in basaltic rocks in Iceland is controlled by alteration mineralogy (Árnason et al., 2010). The resistivity structure in Krýsuvík geothermal field is similar to other high-temperature geothermal systems in Iceland (Flóvenz et al., 1985; Árnason et al., 1987; Eysteinsson et al., 1994; Árnason et al., 2000). At a certain depth, a low-resistivity (conductive) cap domes up (the outer margin of the reservoir) and is underlain by higher resistivity (a resistive core).
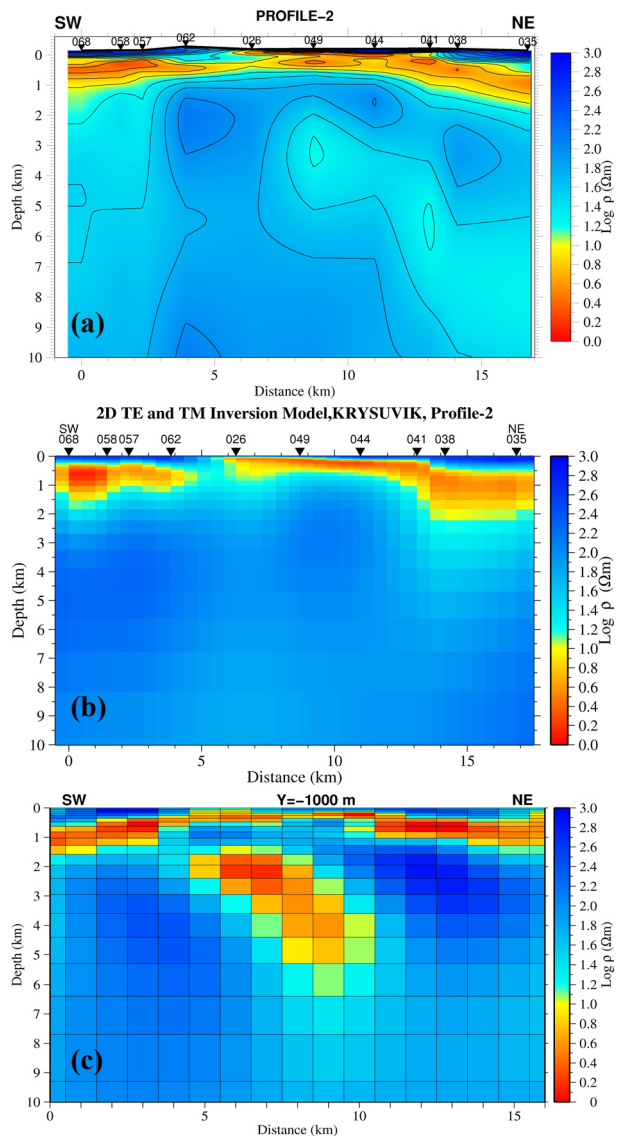

FIGURE 72: Comparison of 1D, 2D and 3D vertical resistivity cross-sections of Profile-2: (a) cross-section from joint 1D inversion. (b) 2D cross-section obtained by inverting jointly TE and TM mode MT data. (c) 3D cross-section across the model at Y = -1000 corresponding to Profile-2

The 1D and 2D inversion of MT data on the two profiles show three main resistivity structures down to a depth of 10 km. A high-resistivity surface layer associated with fresh basaltic lava, hyaloclastites and pillow lavas. A very low-resistivity second layer (< 15 Ωm) of variable thickness was observed along the vertical cross-sections. The conductive layer is presumably associated with smectite and mixed layer clay alteration. A high resistivity (> 15 Ωm) is observed underlying the conductive layer along the cross-sections. The high resistivity could be associated to high-temperature alteration (chlorite-epidote alteration zone) down to a depth of about 2.3 km.

The 3D inversion of 58 MT sites revealed a three layered resistivity structure as seen on 1D and 2D inversion models. In addition, the 3D inversion model slice showed a low-resistivity zone trending ENE-WEW at a depth of about 1.35 km which has the same direction as transform faults inferred from

seismicity. The nature of this low resistivity which is overlain by high resistivity is not known. The 3D inversion, moreover, delineated a deep conductive body embedded at a depth of about 2 km and reaching a depth of 5 km within the high resistivity which is overlain by a conductive layer. The deep conductive body is presumably associated with the heat source of the geothermal system. At greater depths (> 6 km), the 3D inversion of MT data does not show a horizontal deep conducting layer which is commonly observed in the crust beneath Iceland (Beblo and Björnsson, 1978, 1980; Beblo et al., 1983; Hersir et al., 1984; Eysteinsson and Hermance, 1985; Björnsson et al., 2005; Árnason et al., 2010).

REFERENCES

Abdelghafoor, M., 2007: Geological and geothermal mapping in Sveifluháls area, SW-Iceland. Report 3 in: *Geothermal Training in Iceland 2007*. UNU-GTP, Iceland, 1-23.

Ármannsson, H., Thórhallsson, S., Ragnarsson, Á., 1994: *Krýsuvík-Trölladyngja. Potential steam production and transmission to energy park, Straumsvík*. Orkustofnun, Reykjavík, report OS-94012/JHS-07B, 17 pp.

Árnason, K., 2006: *TEMTD (program for 1D inversion of central-loop TEM and MT data)*. ISOR - Iceland GeoSurvey, Reykjavík, short manual, 16 pp.

Árnason, K*.,* 2008: *The magnetotelluric static shift problem*. ISOR - Iceland GeoSurvey, report ÍSOR-08088, 16 pp.

Árnason, K., Eysteinsson, H., Hersir, G.P., 2010: Joint 1D inversion of TEM and MT data and 3D inversion of MT data in the Hengill area, SW Iceland. *Geothermics, vol 39*, 13-34.

Árnason, K., Flóvenz, Ó.G., 1992: Evaluation of physical methods in geothermal exploration of rifted volcanic crust. *GRC Transactions*, 16, 207-217.

Árnason, K., Haraldsson, G.I., Johnsen, G.V., THorbergsson, G., Hersir, G.P., Saemundsson, K., Georgsson, L.S., Rögnvaldsson, S.Th., Snorrason, S.P., 1987: *Nesjavellir-Ölkelduháls. Surface Exploration in 1986*. Orkustofnun, Reykjavík, report OS-87018/JHD-02 (in Icelandic), 112 pp.

Árnason, K., Karlsdóttir, R., Eysteinsson, H., Flóvenz, Ó.G., Gudlaugsson, S.T., 2000: The resistivity structure of high-temperature geothermal systems in Iceland. *Proceedings World Geothermal Congress 2000*, Kyushu- Tohoku, 923-928.

Arnórsson, S., 1987: Gas chemistry of the Krísuvík geothermal field, Iceland, with special reference to evaluation of steam condensation in upflow zones. *Jökull, 37,* 31-48.

Arnórsson, S., Björnsson, A., Gíslason, G., 1975: *Systematic exploration of the Krísuvík high-temperature area, Reykjanes Peninsula, Iceland*. Orkustofnun, Reykjavík, report OS-JHD-7528, 20 pp.

Bahr, K., 1988: Interpretation of the magnetotelluric impedance tensor: regional induction and local telluric distortion, *J. Geophys*., 62, 119-127.

Beblo, M., Björnsson, A., 1978: Magnetotelluric investigation of the lower crust and upper mantle beneath Iceland. *J. Geophys*. 45, 1–16.

Beblo, M., Björnsson, A., 1980: A model of electrical resistivity beneath NE-Iceland, correlation with temperature. *J. Geophys*. 47, 184–190.

Beblo, M., Björnsson, A., Árnason, K., Stein, B., Wolfgram, P., 1983: Electrical conductivity beneath Iceland – Constraints imposed by magnetotelluric results on temperature, partial melt, crust and mantle structure. *J. Geophys*. 53, 16–23.

Berdichevsky, M.N., 1968: *Electrical prospecting by the method of magnetotelluric profiling*. Nedra Publ. House, Moscow.

Berdichevsky, M.N., Bezruk, I.A., Safonov, A.S., 1989: Magnetotelluuric methods. In: Khmelevskoy, V.K. (ed.), *Electrical prospecting. Geophysical reference book*. Nedera Publ. House, Moscow, Part 1, 261-310.

Berdichevsky, M.N., Dmitriev, V.I., 1976: Basic principles of interpretation of magnetotelluric curves. In: Adam, A., (ed.), *Geoelectric and geothermal studies*. Akademini Kiado, 165-221.

Berdichevsky, M.N., Dmitriev, V.I., 2002: *Magnetotellurics in the context of the theory of ill-posed problems*. Society of Exploration Geophysicists, USA, 215 pp.

Berdichevsky, M.N., Dmitriev, V.I., Kuznetsov, V.A., 1995. Bimodal two-dimensional interpretation of MT-soundings. *Phys. Earth (Fizika Zemli), 31-10*, 821-837.

Berdichevsky, M.N., Dmitriev, V.I., Pozdnjakova, E.E., 1998: On two-dimensional interpretation of magnetotelluric soundings. *Geophys. J. Int.*, 133, 585-606.

Berktold, A., 1983: Electromagnetic studies in geothermal regions. *Geophys. Surv.*, 6, 173–200.

Björnsson, A., Eysteinsson, H., Beblo, M., 2005: Crustal formation and magma genesis beneath Iceland: magnetotelluric constraints. In: Foulger, G.R., Natland, J.H., Presnall, D.C., Anderson, D.L. (eds.), *Plates, plumes and paradigms*. Geological Society of America, Spec. Pap. vol. 388 (2005), 665–686.

Brigham, E.O., 1974: *The fast Fourier transform*. Prentice-Hall, Inc. 252 pp.

Cagniard, L., 1953: Basic theory of the magneto-telluric method of geophysical prospecting: *Geophysics*, 18, 605-635.

Chave, A.D., Smith, J.T., 1994: On electric and magnetic galvanic distortion tensor decompositions. *J. Geophys. Res.*, 99, B3, 4669-4682.

Clarke, J., Gamble, T.D., Goubau, W.M., Koch, R.H., Miracky, R.F., 1983: Remote reference magnetotellurics: Equipment and procedures. *Geophys. Prosp., 31*, 149-170.

Clifton, A., Pagli, C., Jónsdóttir, J., Eythórsdóttir, K., Vogfjörd, K., 2003: Surface effects of triggered fault slip on Reykjanes Peninsula, SW Iceland. *Tectonophysics*, *369*, 145-154.

Constable, C.S., Parker, R.L., Constable, C.G., 1987: Occam inversion: A practical algorithm for generating smooth models from electromagnetic sounding data. *Geophysics*, 52, 289-300.

Deer,W.A., Howie, R.A., Zussman, J.,1962: *Rock-forming minerals*, vol. 3: Sheet silicates. Longmans, Green and Co. Ltd., London, UK, 270 pp.

deGroot_Hedlin, C., Constable, S., 1990: Occam inversion to generate smooth, two dimensional models from magnetotelluric data. *Geophysics*, 55, 1613-1624.

Einarsson, S., Jóhannesson, H., Sveinbjörnsdóttir, Á., 1991: Age of the Kapelluhraun and Hellnahraun lava flows, Reykjanes Peninsula, South Iceland. *Jökull, 41*, 61-80.

Encyclopaedia Britannica, 2010: *Solar wind*. Encyclopædia Britannica Online, webpage: *www.britannica.com/EBchecked/topic/1589681/Solar-Dynamics-Observatory*.

Eysteinsson, H., 1999: *Resistivity measurements around Sandfell, Reykjanes Peninsula.* Orkustofnun, Reykjavik, report OS-99002 (in Icelandic), 71 pp.

Eysteinsson, H., 2001: *Resistivity measurements around Trölladyngja and Núpshlídarháls, Reykjanes Peninsula.* Orkustofnun, Reykjavik, report OS-2001/038 (in Icelandic), 110 pp.

Eysteinsson, H., Árnason, K., Flóvenz, Ó.G., 1994: Resistivity methods in geothermal prospecting in Iceland. *Surv. Geophy.* 15, 263–275.

Eysteinsson, H., and Hermance J.F., 1985: Magnetotelluric measurements across the eastern neovolcanic zone in south Iceland, *J. Geophys. Res.*, 90, 10093–10103.

Flóvenz, Ó.G., Fridleifsson, G.Ó., Johnsen, G.V., Kristmannsdóttir, H., Georgsson, L.S., Einarsson, S., Thórhallsson, S., Jónsson, S.L., 1986: *Vatnsleysa-Trölladyngja, freshwater and geothermal*

investigation. 3. Geothermal exploration. Orkustofnun, Reykjavík, report OS-86032/JHD-10 B, 39-92.

Flóvenz, Ó.G., Georgsson, L.S., Árnason, K., 1985: Resistivity structure of the upper crust in Iceland. *J. Geophys. Res.* 90, 10136–10150.

Flóvenz, Ó.G., Spangerberg, E., Kulenkampff, J., Árnason, K., Karlsdóttir, R., Huenges, E., 2005: The role of electrical interface conduction in geothermal exploration. *Proceeding World Geothermal Congress 2005*, Antalya, Turkey.

Fridleifsson, G.Ó., Richter, B., Björnsson, G., Thórhallsson, S., 2002: *Trölladyngja - well TR-01, progress report about drilling and research.* Orkustofnun, Reykjavík, report, OS-2002/053 (in Icelandic), 55 pp.

Gamble, T.D., Goubau, W.M., Clarke, J., 1979: Magnetotellurics with a remote magnetic reference. *Geophysics*, 44, 53-68.

Geoffroy, L., Dorbath, C., 2008: Deep downward fluid percolation driven by localized crust dilatation in Iceland. *Geophysical Research Letters*, 35.

Georgsson, L.S., 1987: Application of resistivity sounding in the exploration of high-temperature geothermal areas in Iceland with examples from the Trölladyngja-Krýsuvik area, SW-Iceland. *Technical programme and Abstracts of Exploration '87*, Toronto, 52.

Gisle, G., Manik, T., 1977: *Bathymetry of the Norwegian-Greenland seas map*, Department of Geology, University of Oslo, Norway.

Goubau, W.M., Gamble, T.D., Clarke, J., 1979. Magnetotelluric data analysis: removal of bias. *Geophysics, 43*, 1157-1169.

Groom, R.W., Bailey, R.C., 1989: Decomposition of the magnetotelluric impedance tensor in the presence of local three-dimensional galvanic distortion. *J. Geophys. Res.*, 94, 1913-1925.

Hersir, G.P., Björnsson, A., Pedersen, L.B., 1984: Magnetotelluric survey across the active spreading zone in southwest Iceland. *J. Volc. Geothermal Res.* 20, 253– 265.

Hersir, G.P., Vilhjálmsson, A.M., Rosenkjær, G.K., Eysteinsson, H., and Karlsdóttir, R., 2010: *The Krýsuvík geothermal field. Resistivity soundings 2007 and 2008.* ÍSOR - Iceland GeoSurvey, Reykjavík, report ÍSOR-2010/025 (in Icelandic), 263 pp.

Imsland, P., 1973: *The geology of Sveifluháls.* University of Iceland, BSc thesis (in Icelandic), 87 pp.

Jakobsson, S., 1972: Chemistry and distribution pattern of recent basaltic rocks in Iceland. *Lithos*, *5*, 365-386.

Jiracek, G., 1990: Near-surface and topographic distortions in electromagnetic induction. *Surv. Geophys.*, 11,163-203.

Jiracek, G.R., Haak, V., Olsen, K.H., 1995: Practical magnetotellurics in a continental rift environment; In: Olsen, H.K.. (ed.), *Continental rifts: evolution, structure, tectonics*: Elsevier, NY, 103-129.

Jónsson, J., 1978*: A geological map of the Reykjanes Peninsula.* Orkustofnun, Reykjavík, report OS/JHD 7831 (in Icelandic), 333 pp and maps.

Jupp, D. L.B., Vozoff , K., 1975: Stable iterative methods for the inversion of geophysical data. *Geophys. J. Roy. Astr. Soc.*, 42, 957-976.

Kamah, M.Y., 1996: Borehole geology, hydrothermal alteration and temperature evolution of well KR-2, Krýsuvík, SW-Iceland. Report 5 in: *Geothermal Training in Iceland 1996*. UNU-GTP, Iceland, 71-102.

Kaufman, A.A., 1988: Reduction of the geological noise in magnetotelluric soundings, *Geodex*, 25,145-161.

Kebede, Y., 2001: Application of the resistivity method in the Krísuvík geothermal area, Reykjanes Peninsula, SW-Iceland. Report 6 in: *Geothermal Training in Iceland 2001*. UNU-GTP, Iceland, 115-142.

Keiding, M., Lund, B., Árnadóttir, T., 2009: Earthquakes, stress, and strain along an obliquely divergent plate boundary: Reykjanes Peninsula, southwest Iceland. *J. Geophysical research*, 114, B09306.

Kristmannsdóttir, H., 1979: Alteration of basaltic rocks by hydrothermal activity at 100–300 °C. In: Mortland, M.M., Farmer, V.C. (eds.), *Proceedings of the VI International Clay Conference* 1978. Elsevier, New York, NY, USA, 277–288.

Mackie, R.L., Bennett, B.R., Madden, T.R., 1988: Long period magnetotelluric measurements near the central California coast: A land-locked view of the conductivity structure under the Pacific Ocean. *Geophys. J. R. Astron. Soc.*, 95, 181-194.

Mackie, R.L., 2002: *Multi-dimensional modelling and inversion*. GSY-USA Inc., San Francisco, Ca, USA, 16 pp.

Magnússon, I.Th., Árnason K., 2002: *Earthquakes and fractures around Trölladyngja and Krýsuvík, Comparison with the specific resistivity* (in Icelandic). Orkustofnun, Reykjavik, report OS-2002/048.

Malapitan, R.T., 1995: Borehole geology and hydrothermal alteration of well KR-9, Krýsuvik, SW-Iceland. Report 8 in: *Geothermal Training in Iceland 1995*. UNU-GTP, Iceland, 185-206.

Mortensen A.K., Jónsson, S.S., Richter, B., Sigurdsson, Ó., Birgisson, K., Karim Mahmood, A.T., Gíslason, J., 2006: *Trölladyngja, well TR-02, 3rd phase: Drilling of 12 ¼" production part from 800 to 2280 m depth.* ÍSOR, Reykjavík, report ÍSOR-2006/060 (in Icelandic), 75 pp.

Muller, W., Losecke, W., 1975: Accelerating convergence techniques and grid spacing problem in two dimensional magnetotelluric modelling. *Geophys. J. R. Astr. Soc.*, 41, 185-191.

Newman, G.A., Gasperikova, E., Hoversten, G.M., Wannamaker, P. E., 2008. Three-dimensional magnetotelluric characterization of the Coso geothermal field, *Geothermics* 37-4, 369-399.

Oldenburg, D.W., McGillivray, P.R., Ellis, R.G., 1993: Generalized subspace methods for large scale inverse problems, *Geophys. J. Internat.*, 114, 12-20.

Palacky, G.J., 1987: Resistivity characteristics of Geologic targets. In: *Electromagnetic methods in applied geophysics, 1. Theory.* Soc. Expl. Geophys., Tusla, OK, USA.

Pálmason, G., Saemundsson, K., 1974: Iceland in relation to the Mid-Atlantic Ridge. *Annual Review of Earth and Planetary Sciences, 2*, 25-50.

Parker, E.N., 1958: Dynamics of the interplanetary gas and magnetic field. *Astrophys. J.* 128, 664-676.

Parker, R.L., 1994: *Geophysical inverse theory.* Princeton University Press.

Parker, R.L., 1980: The inverse problem of electromagnetic induction: existence and construction of solutions based upon incomplete data. *J. Geophys. Res.*, 85, 4421-4425.

Parkinson, W.D., 1959: Direction of rapid geomagnetic fluctuations. *Geophys. J. R. Astron. Soc.*, 2, 1-14.

Parkinson, W.D., 1962: The influence of continents and oceans on geomagnetic variations. *Geophys. J. Royal Astron. Soc.*, 6, 441-449.

Pellerin, L., Hohmann, G.W., 1990: Transient electromagnetic inversion: A remedy for magnetotelluric static shifts. *Geophysics*, *55-9,* 1242-1250.

Pellerin, L., Johnston, J.M., Hohmann, G.W., 1996: Numerical evaluation of electromagnetic methods in geothermal exploration. *Geophysics*, 61-1, 121–130.

Phoenix Geophysics, 2005: *Data processing user guide.* Phoenix Geophysics Ltd., ON Canada.

Ranganayaki, R.P., 1984: An interpretative analysis of magnetotelluric data. *Geophysics,* 49, 1730-1748.

Ranganayaki, R.P., Madden, T.R., 1980: Generalized thin sheet analysis in magnetotellurics: An extension of Price's analysis, *Geophys. J. R. Astro. Soc.*, 60, 445-457.

Reddy, I.K., Rankin, D., Phillips, R.J. 1977: Three-dimensional modelling in magnetotelluric and magnetic variational sounding. *Geophys. J. R. Astr. Soc.* 51, 313-325.

Rodi, W.L., Mackie, R.L., 2001: Nonlinear conjugate gradients algorithm for 2-D magnetotelluric inversion. *Geophysics* 66, 174–187.

Saemundsson, K., 1995: *Geological map of the Hengill area, 1:25,000*. Orkustofnun, Reykjavík, Iceland.

Saemundsson, K., Einarsson, S., 1980: *Geological map of Iceland, sheet 3, SW-Iceland* (2nd edition). Museum of Natural History and the Iceland, Geodetic Survey, Reykjavík.

Saemundsson K., Jóhannesson H., Hjartarson Á., Kristinsson S.G., 2010: *Geological map of Southwest Iceland, 1:100.000*. ISOR - Iceland GeoSurvey, Orkustofnun, Reykjavík, Iceland.

Simpson, F., Bahr, K., 2005: *Practical magnetotellurics*. Cambridge University Press, Cambridge, UK, 254 pp.

Sims, W.E., Bostick, F.X., Smith, H.W., 1971: The estimation of magnetotelluric impedance tensor elements from measured data. *Geophysics*, 36, 938-942.

Siripunvaraporn, W., Egbert, 1999: *Software documentation and user manual a Reduced Basis Occam (REBOCC) inversion version 1.0 for Two-dimensional magnetotelluric data*. College of Oceanic and Atmospheric Sciences, Oregon State University, Corvallis, 97331, 19 pp.

Siripunvaraporn, W., Egbert, G., 2000: An efficient data-subspace inversion method for 2-D Magnetotelluric data. *Geophysics*, 65, 791-803.

Siripunvaraporn, W., Egbert, G., Lenbury,Y., 2002: Numerical accuracy of magnetotelluric modeling: a comparison of finite difference approximations. *Earth Planets Space* 54, 721–725.

Siripunvaraporn, W., Egbert, G., Lenbury, Y., Uyeshima, M., 2005: Three-dimensional magnetotelluric inversion: data-space method. *Phys. Earth Planet. Interiors,* 150, 3–14.

Siripunvaraporn,W., Egbert, G., Lenbury, Y., Uyeshima, M., 2006*: WSINV3DMT version 1.0.0 for single processor machine user manual.* Mahidol University, Department of physics, Faculty of Science, Bangkok, Thailand, 21 pp.

Smith, J.T., Booker, J.R., 1988: Magnetotelluric inversion for minimum structure. *Geophysics*, 53, 1556-1576.

Smith, J.T., Booker, J.R., 1991: Rapid inversion of two- and three-dimensional magnetotelluric data. *J. Geophys. Res.,* 96, 3905-3922.

Smith, J.T., 1995: Understanding telluric distortion matrices. *Geophys. J. Int.,* 122, 219-226.

Sternberg, B.K., Washburne, J.C., Pellerin, L., 1988: Correction for the static shift in magnetotellurics using transient electromagnetic soundings. *Geophysics,* 53, 1459-1468.

Tikhonov, A.N., 1950: *The determination of electrical properties of the deep layers of the Earth's crust.* Dokl. Acad. Nauk., SSR 73: 295-297 (in Russian).

Tikhonov, A.N., Arsenin, V.Y., 1977: *Solution to ill- posed problems*. John Wiley, New York.

Tikhonov, A.N., 1986: On determining electrical characteristics of the deep layers of the Earth's crust. In: Vozoff, K., (ed.), *Magnetotelluric methods*: Soc. of Expl. Geophys., 2-3.

Uchida, T., 1993: Smooth 2-D Inversion for magnetotelluric data based on statistical criterion ABIC*, J. Geomag. Geoelectr*., 45,841-858.

Vargas, J., 1992: *Geology and geothermal considerations of Krísuvík valley, Reykjanes Peninsula.* UNU-GTP, Iceland, report *13*, 35 pp.

Vozoff, K., 1972: The magnetotelluric method in the exploration of sedimentary basins. *Geophysics,* Soc. of Expl. Geophys., 37, 98-141.

Vozoff, K., 1991: The magnetotelluric method. In: *Electromagnetic methods in applied geophysics. vol. 2: Application.* Soc. Expl. Geophys., Tulsa, OK., 972 pp.

Wannamaker, P.E., Hohmann, G.W., Ward, S.H., 1984: Magnetotelluric responses of three-dimensional bodies in layered earth. *Geophysics*, 49**,** 1517–1533.

Weidelt, P., 1972: The inverse problem of geomagnetic induction. *Z. Geophys.,* 38. 257-289.

Wight, D.E., Bostick, F.X., 1980: Cascade decimation- A technique for real time estimation of power spectra, Acoustics, speech, and signal processing. *IEEE International Conference on ICASSP. Apos, 80-5*, 626 – 629.

Yohannes, E.B., 2004: Geochemical interpretation of thermal water and gas samples from Krýsuvik, Iceland and Alid, Eritrea. Report 18 in: *Geothermal Training in Iceland 2004.* UNU-GTP, Iceland, 403-437.

Zhang, P., Roberts, R.G., Pederson, L.B., 1987: Magnetotelluric strike rules. *Geophysics*, 149, 405-419.

Zhdanov, M.S., Keller, G.V., 1994: *The geoelectrical methods in geophysical exploration*. Elsevier, Amsterdam, 873 pp.

APPENDIX A: 1D joint inversion of TEM and MT
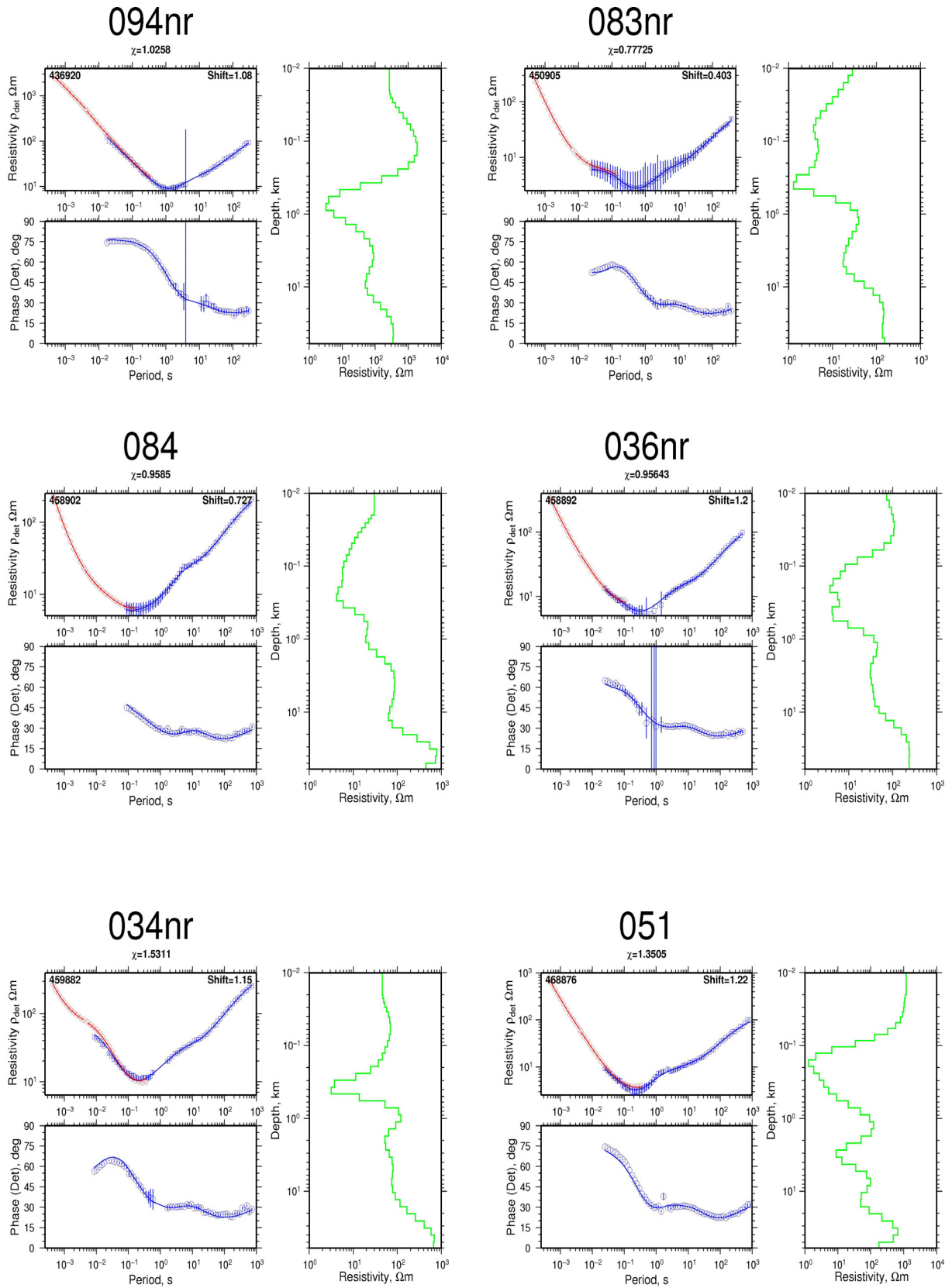
FIGURE A1: 1D joint inversion of TEM and MT model profile-1.Red diamonds are measured TEM data. Blue squares and blue circles are measured MT apparent resistivities and phases, respectively obtained from the determinant of the MT impedance tensor. The solid curves in the left panels are calculated responses from the Occam inversion model to the right
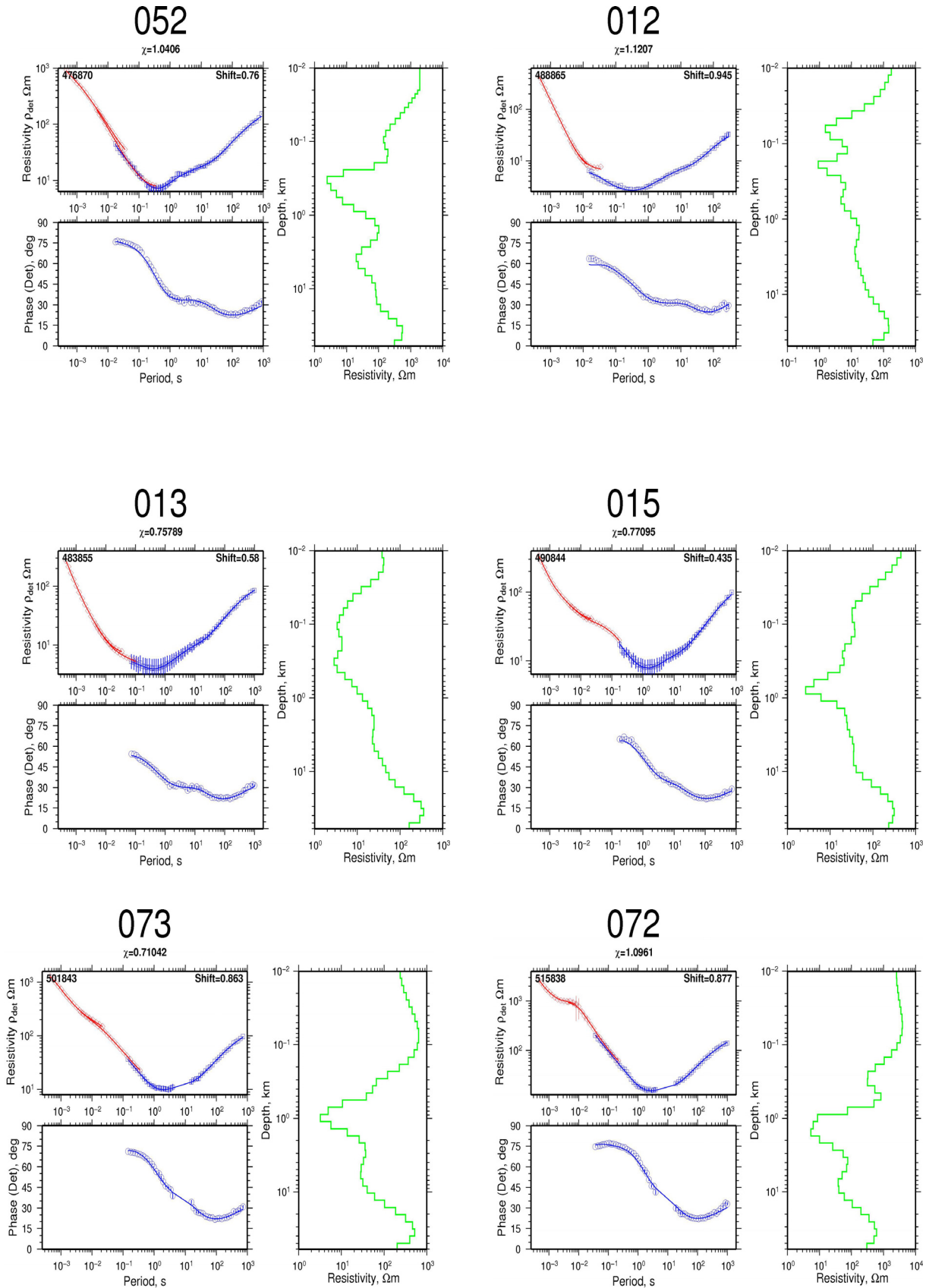
FIGURE A1: Continued
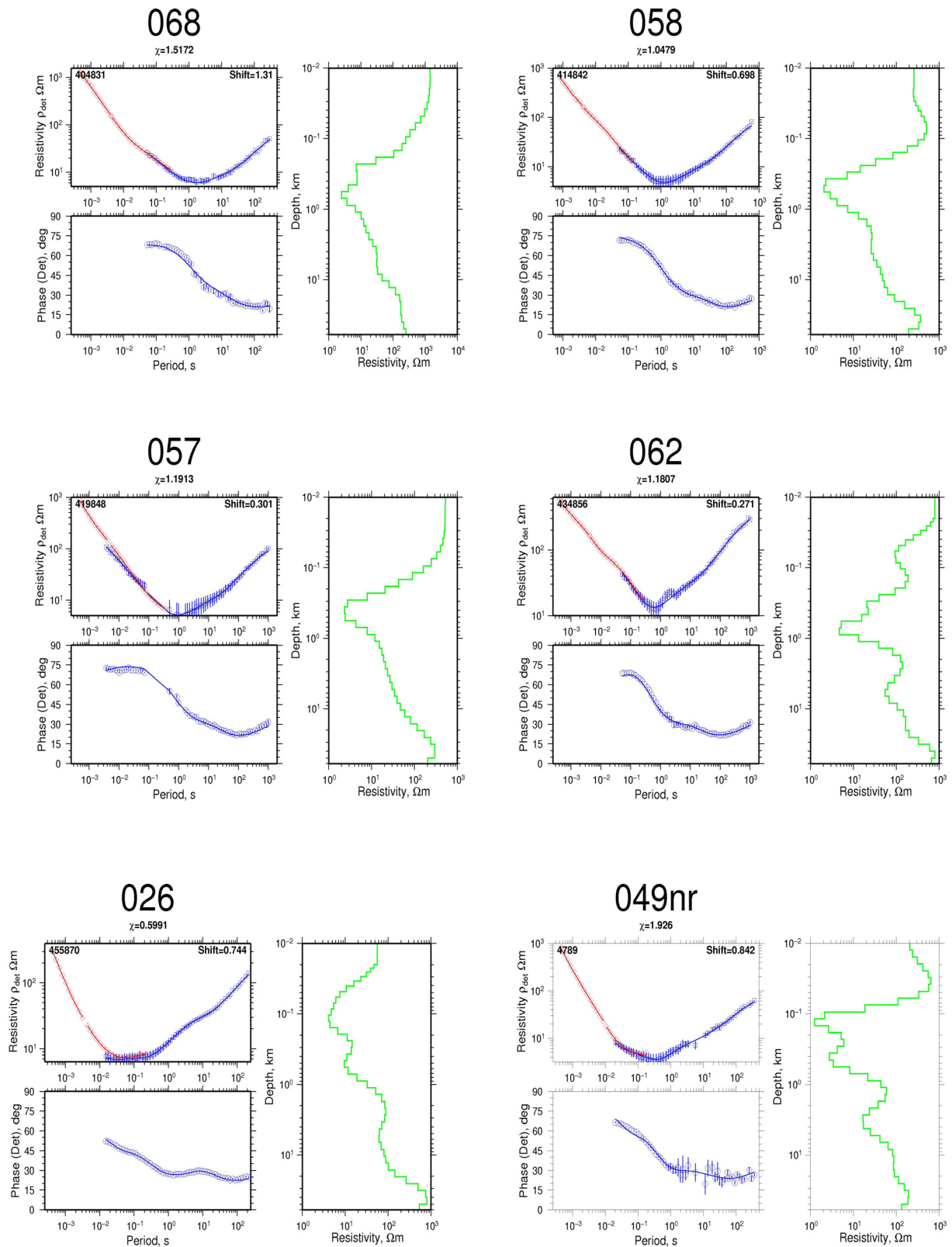
FIGURE A2: 1D joint inversion of TEM and MT model profile-2. Red diamonds are measured TEM data. Blue squares and blue circles are measured MT apparent resistivities and phases, respectively obtained from the determinant of the MT impedance tensor. The solid curves in the left panels are calculated responses from the Occam inversion model to the right
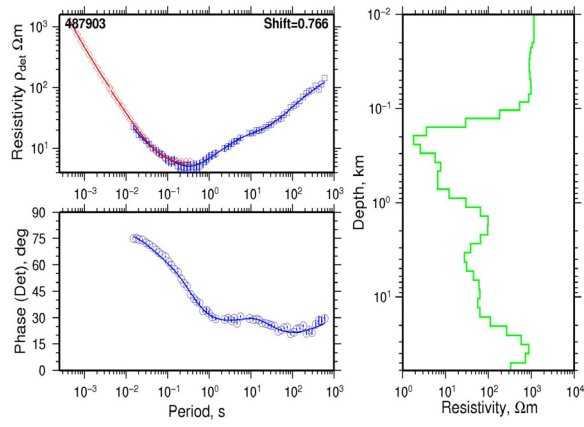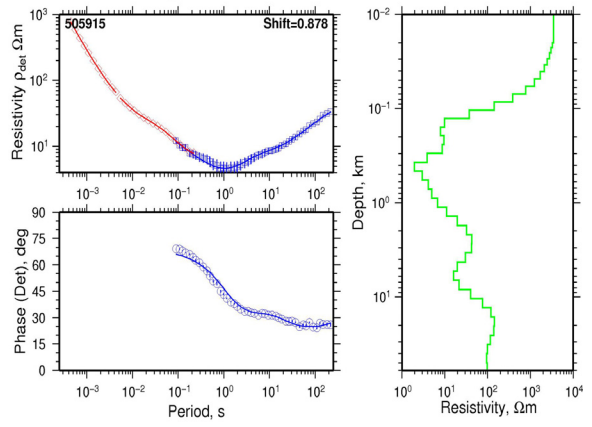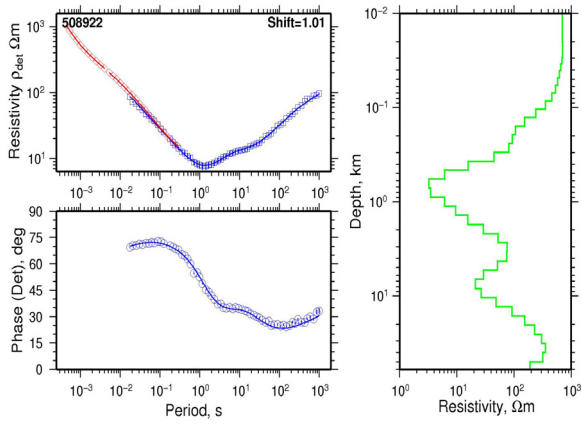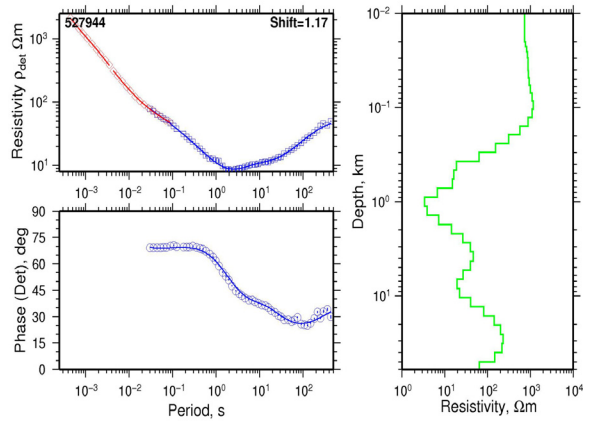
FIGURE A2: Continued

APPENDIX B: 2D inversion responses
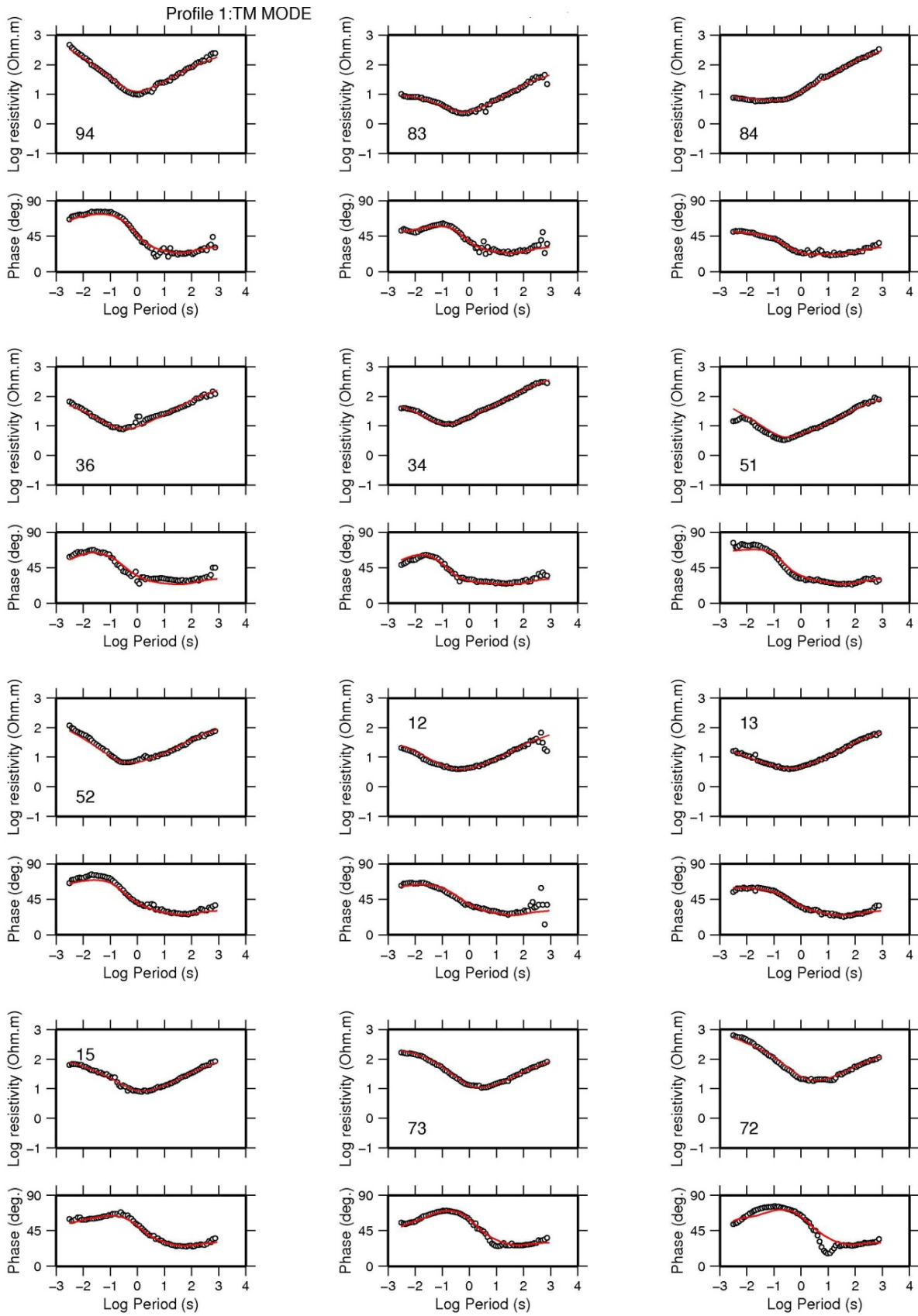
FIGURE B1: Fit for the 2D inversion TE mode apparent resistivity ρₐ in (Ωm) and phase ϕ in (°) of MT sites on profile-1. Solid red curves show the response of the inversion model. The black circles are measured MT data points
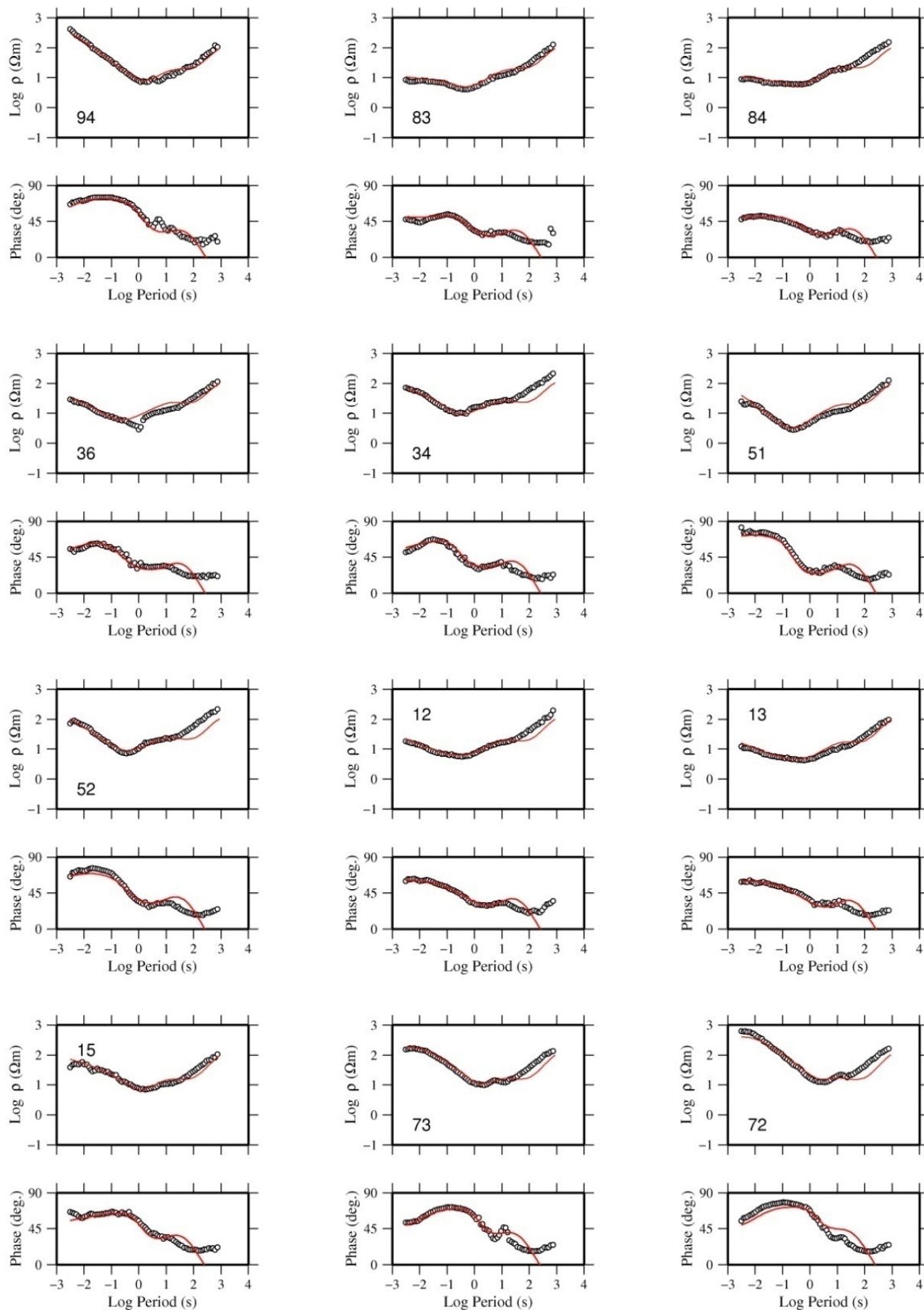
FIGURE B2: Fit for the 2D inversion TM mode apparent resistivity ρ_a in (Ωm) and phase ϕ in (°) of MT sites on Profile-1. Solid red curves show the response of the inversion model. The black circles are measured MT data points
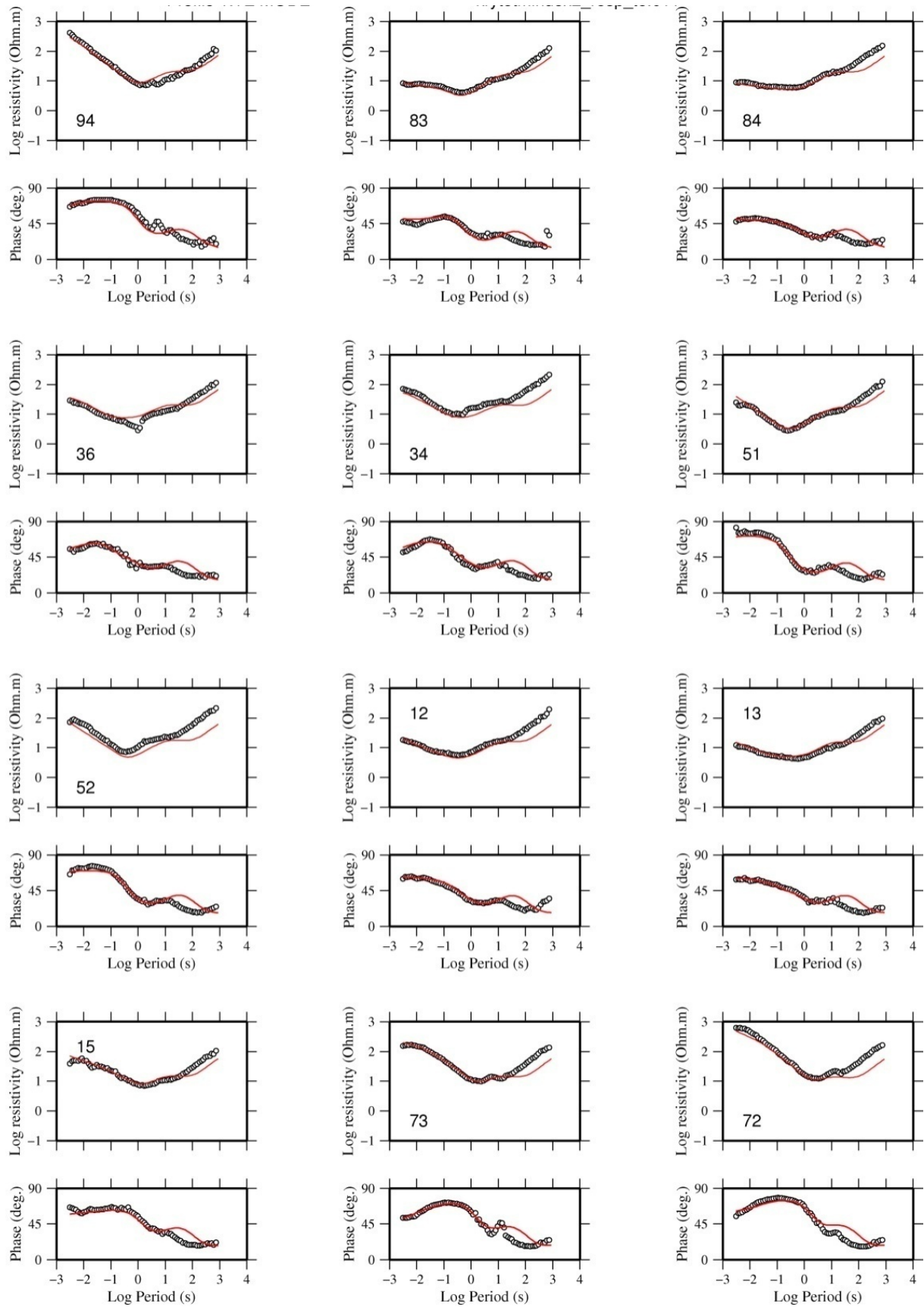
FIGURE B3: Fit for TE mode in joint TE and TM mode inversion apparent resistivity ρ_a in (Ωm) and phase ϕ in (°) of MT sites on Profile-1. Solid red curves show the response of the inversion model. The black circles are measured MT data points
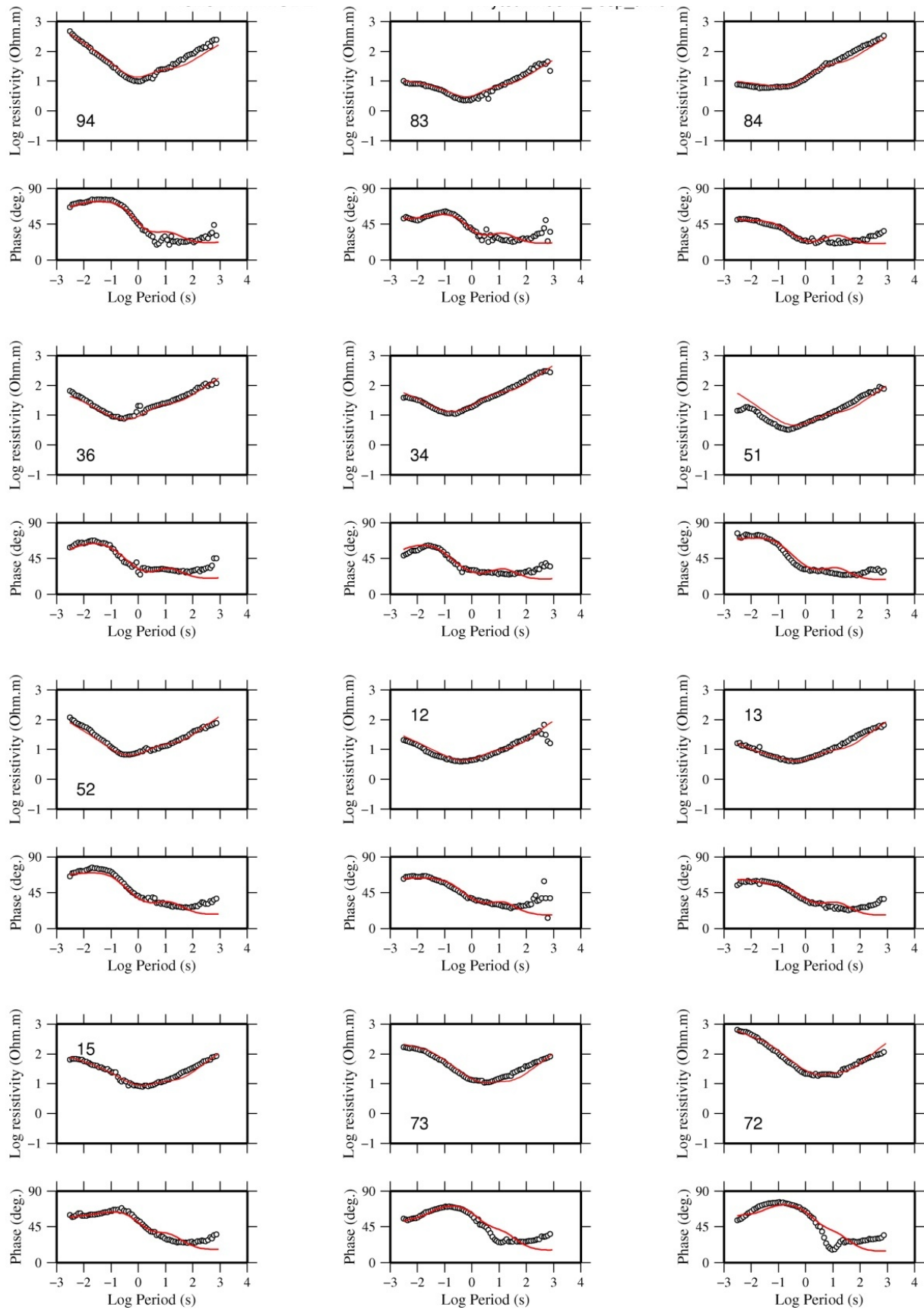
FIGURE B4: Fit for TM mode in joint TE and TM mode inversion apparent resistivity ρ_a in (Ωm) and phase ϕ in (°) of MT sites on profile-1. Solid red curves show the response of the inversion model. The black circles are measured MT data points
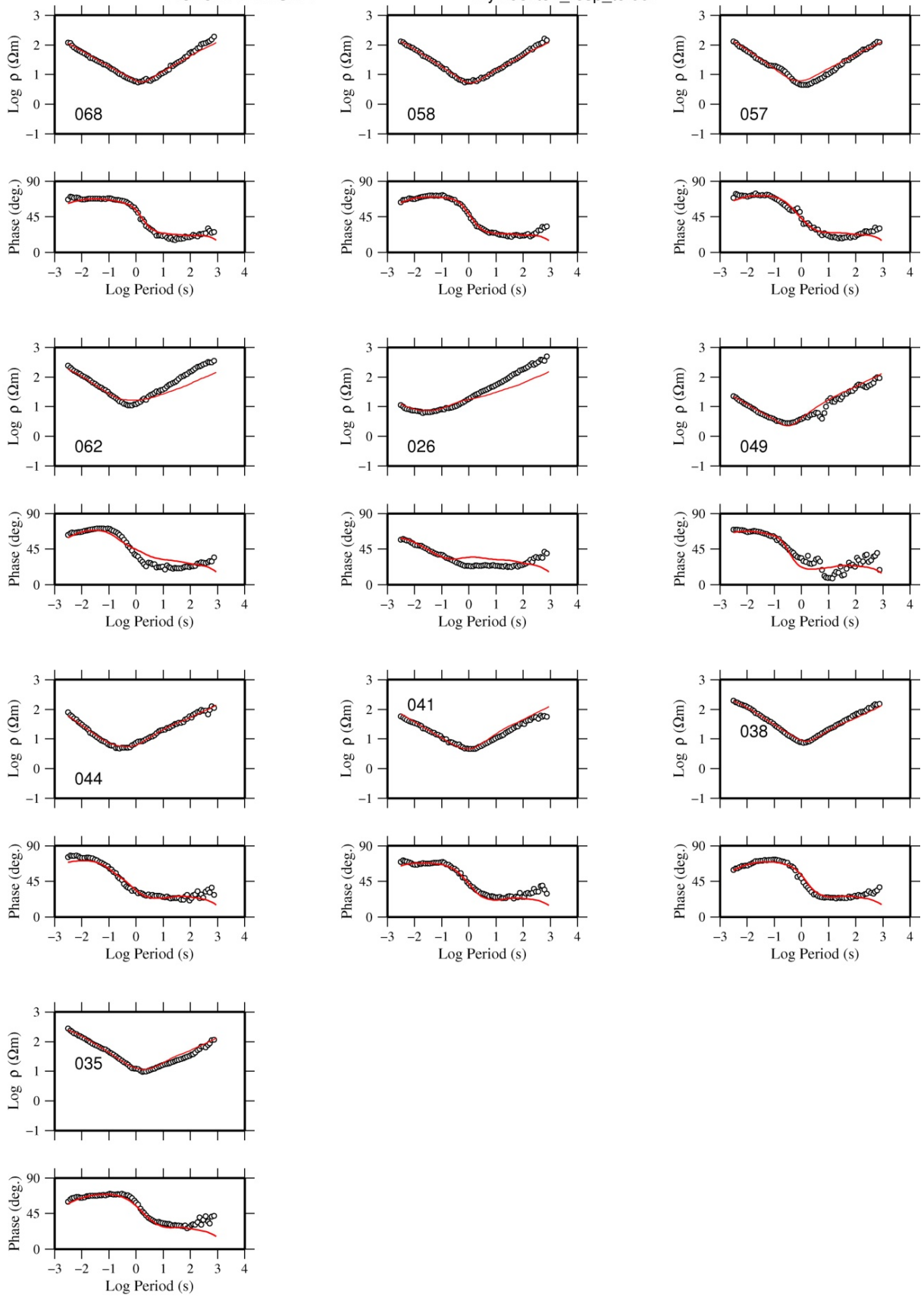
FIGURE B5: Fits for the 2D inversion for TE mode apparent resistivity ρ_a in (Ωm) and phase ϕ in (°) of MT sites on profile-2. Solid red curves show the response of the inversion model. The black circles are measured MT data points
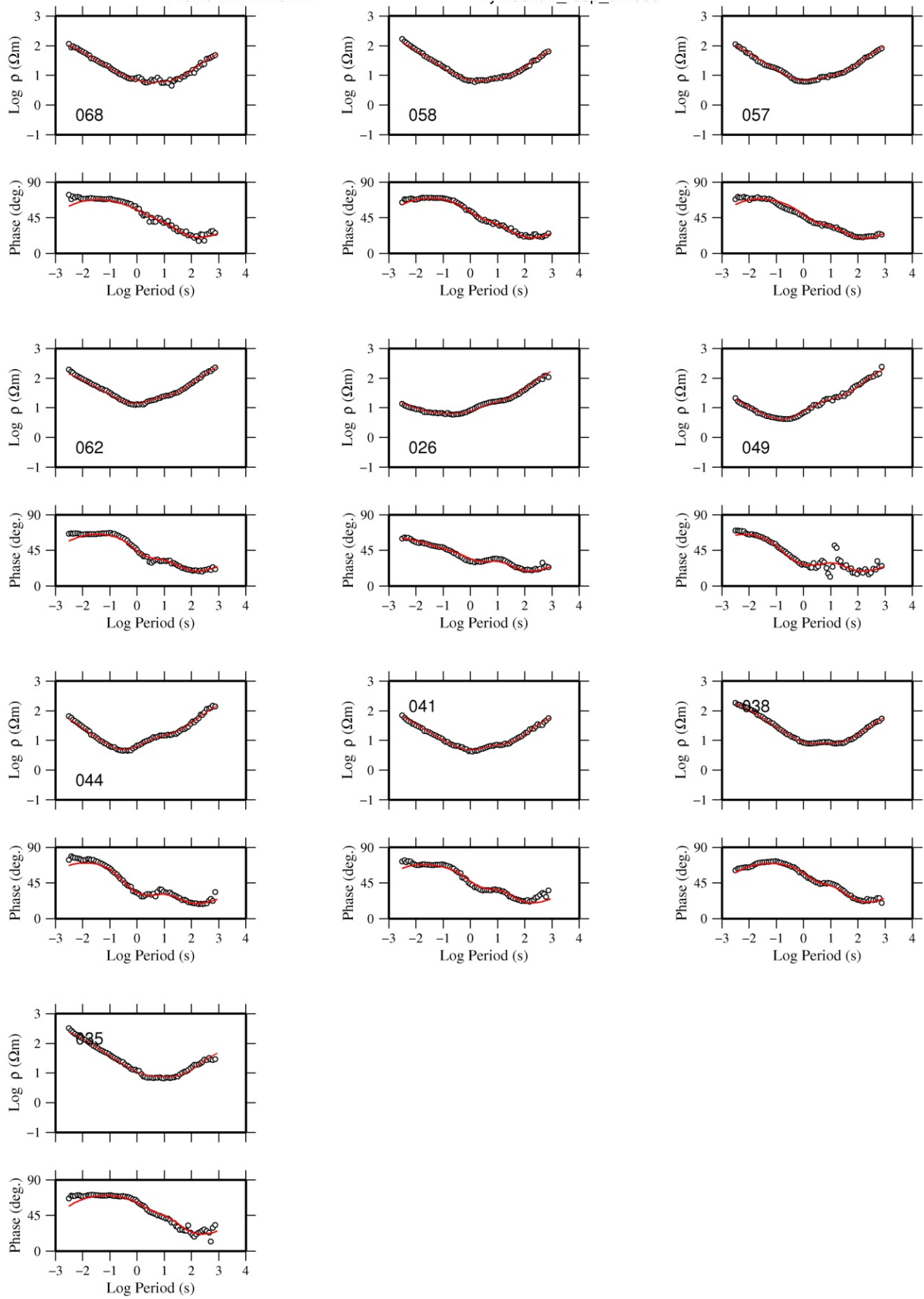
FIGURE B6: Fit for the 2D inversion for TM mode apparent resistivity ρ_a in (Ωm) and phase ϕ in (°) of MT sites on profile-2. Solid red curves show the response of the inversion model. The black circles are measured MT data points
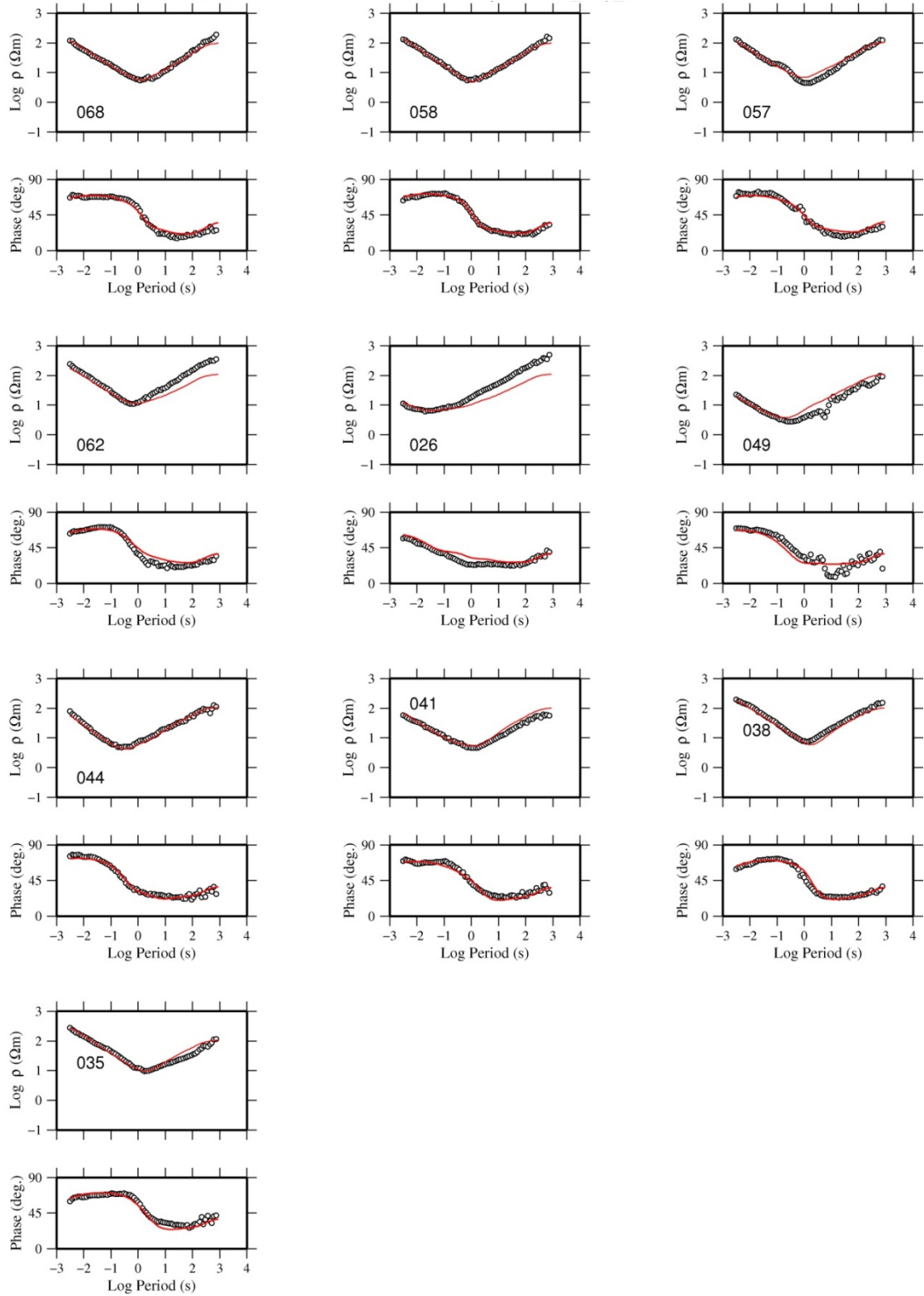
Figure B7: Fit for TE mode in joint TE and TM mode inversion apparent resistivity ρ_a in (Ωm) and phase ϕ in (°) of MT sites on profile-2. Solid red curves show the response of the inversion model. The black circles are measured MT data points
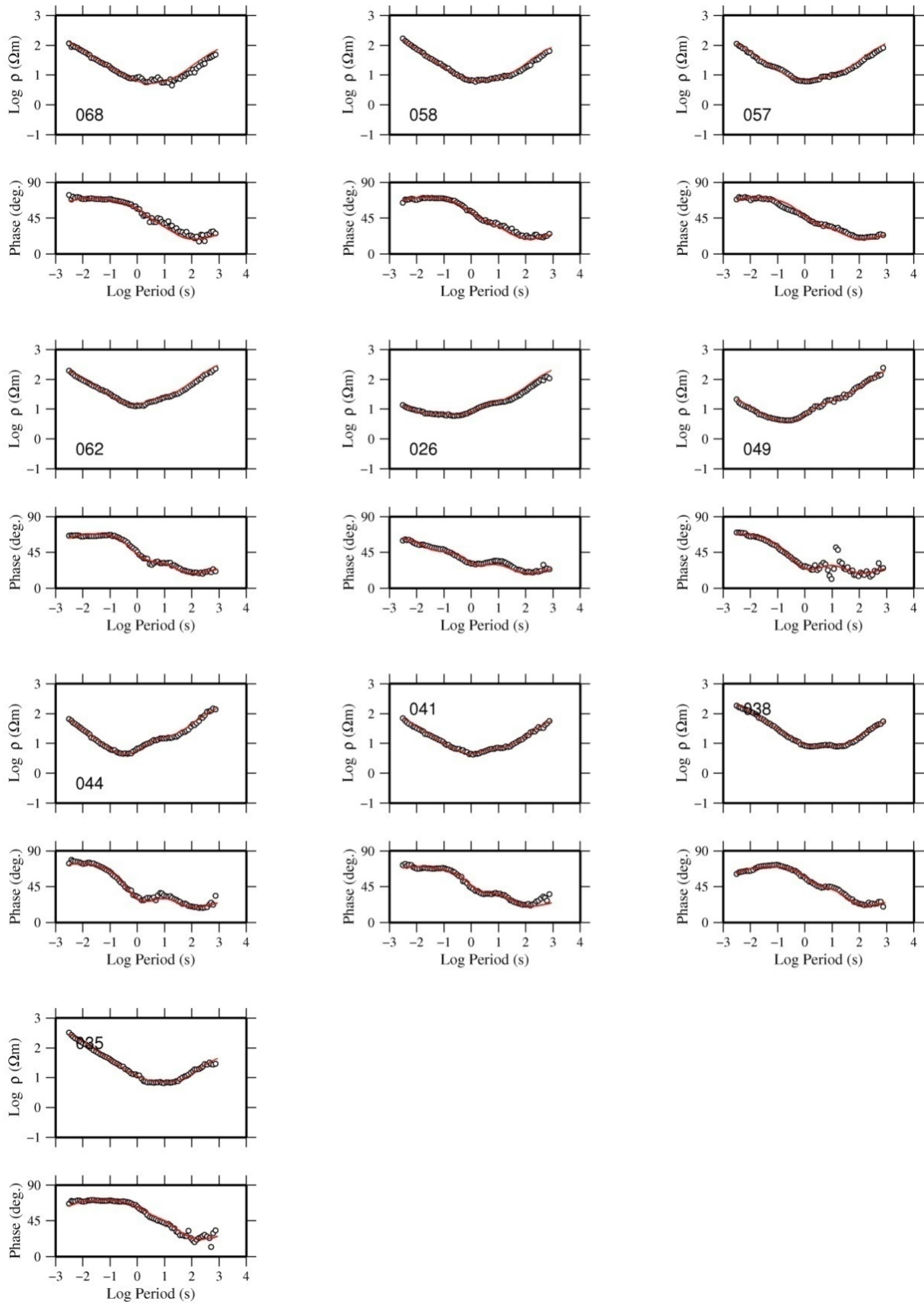
FIGURE B8: Fit for TM mode in joint TE and TM mode inversion apparent resistivity ρ_a in (Ωm) and phase ϕ in (°) of MT sites on profile-2. Solid red curves show the response of the inversion model. The black circles are measured MT data points

APPENDIX C: Krýsuvík MT dataset, locations and responses

The following figures presents model responses and measured MT data for apparent resistivity (ρ_{xy} and ρ_{yx}) in (Ωm) and phase ϕ in (°) of MT sites from 3D inversion.

TABLE C1: Location and elevation of MT soundings considered for 3D inversion.

MT site	Easting (UTM)	Northing (UTM)	Elevation(m)
002	449820	7082820	118
003	453100	7087570	155
004	453220	7086490	188
005	451760	7086890	151
006	452520	7085710	166
008	450700	7085530	222
011	449230	7087530	156
012	448670	7086650	163
015	448930	7084440	214
016	447320	7084550	191
017	448360	7084870	164
018	446880	7082500	129
020	444640	7081910	118
022	442000	7083050	112
023	444090	7083980	118
025	445910	7086820	188
027	445030	7085410	135
028	450820	7088980	149
029	445700	7085840	167
030	450350	7086910	146
031	449910	7088020	144
033	445300	7087980	296
034	445990	7087930	247
037	452000	7091980	311
038	451110	7092000	219
040	451240	7091120	355
041	450400	7091290	217
043	449470	7089770	211
047	447710	7089660	206
051	447090	7087440	199
053	440150	7083650	143
056	442050	7085560	158
058	441520	7083930	144
059	440570	7085090	147
060	440720	7086730	156
062	443540	7085280	273
063	439210	7085630	103
064	446530	7086250	243
065	447120	7085720	312
067	445890	7084890	203
069	445770	7083580	277
071	440960	7088330	198
072	451210	7083830	238
073	450130	7084300	211
074	445580	7092790	116
081	445530	7090970	137
082	446570	7089740	294
084	445680	7090020	224
085	446810	7091250	219
087	444320	7088380	183
088	444510	7089510	185
090	444690	7086980	296
092	443300	7090470	164
094	443590	7091750	154
096	449970	7092660	184
097	448430	7093090	170
098	447930	7091560	177
099	446920	7092790	128
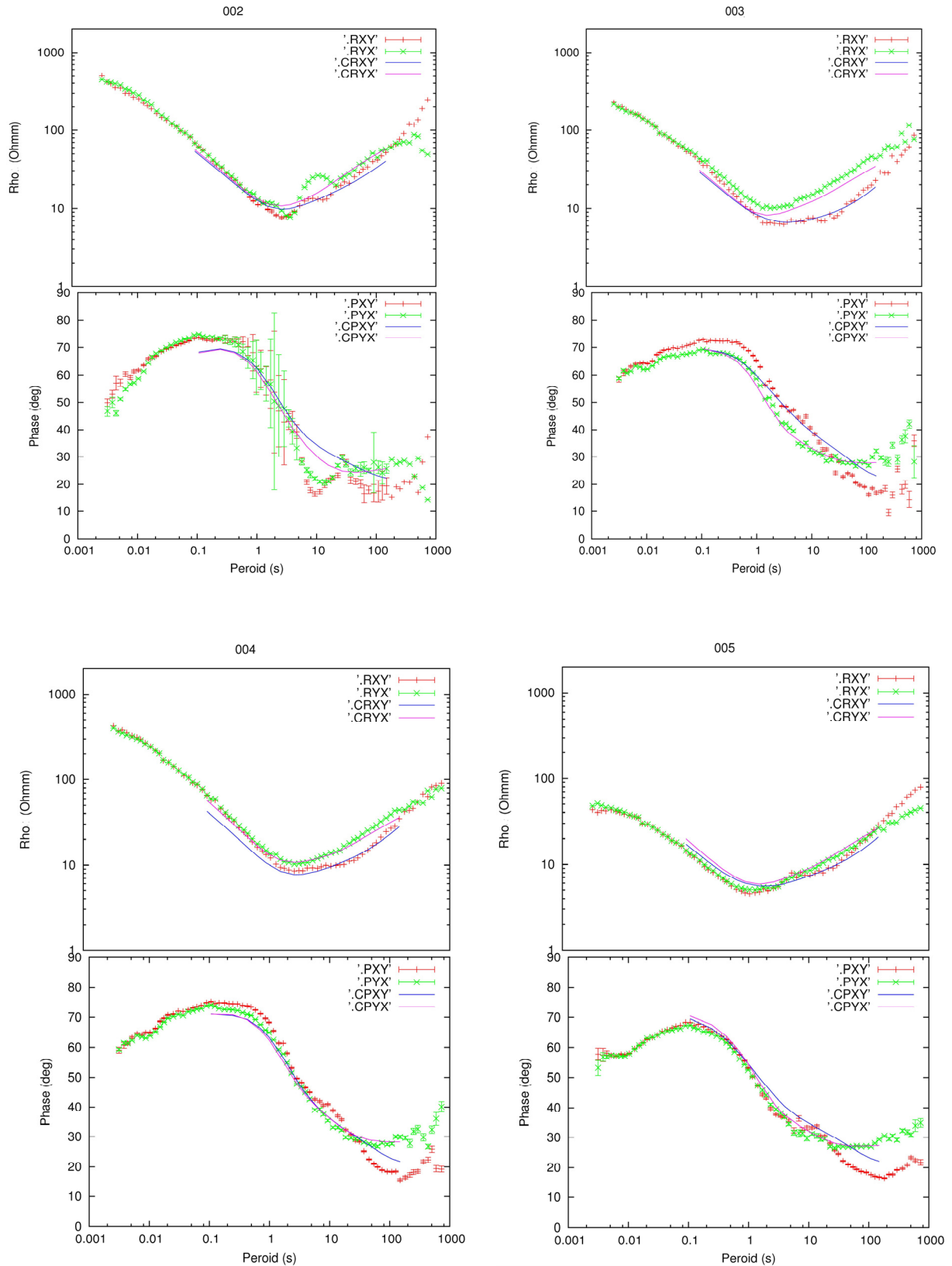
FIGURE C1: Fits of measured data values and model responses for the apparent resistivity and phase of MT sites from 3D inversion. Blue and purple solid lines: calculated responses of apparent resistivity and phase for xy and yx components, respectively. Red pluses and Green crosses: static shift corrected apparent resistivity and phase measured data for xy and yx components, respectively
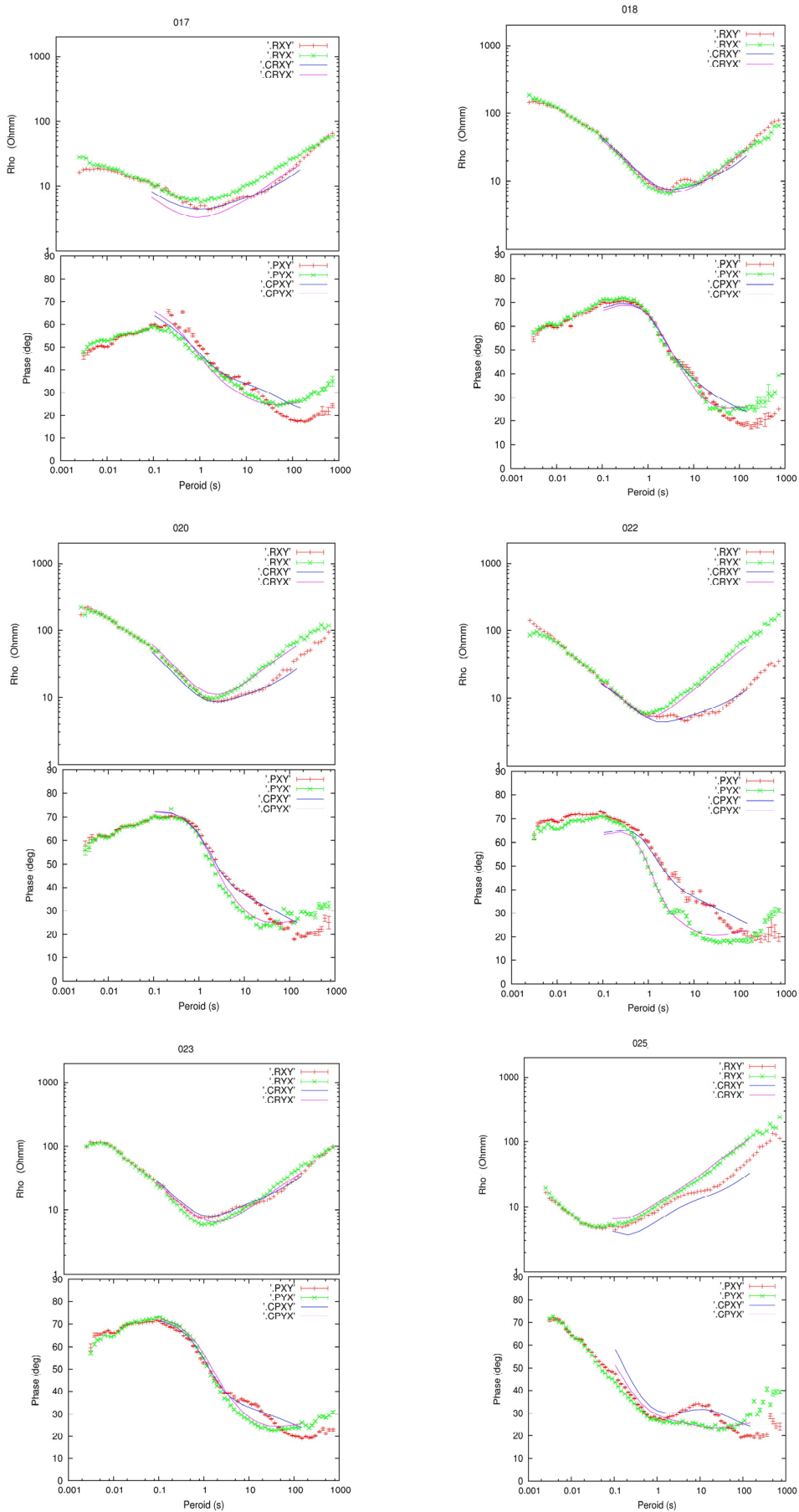
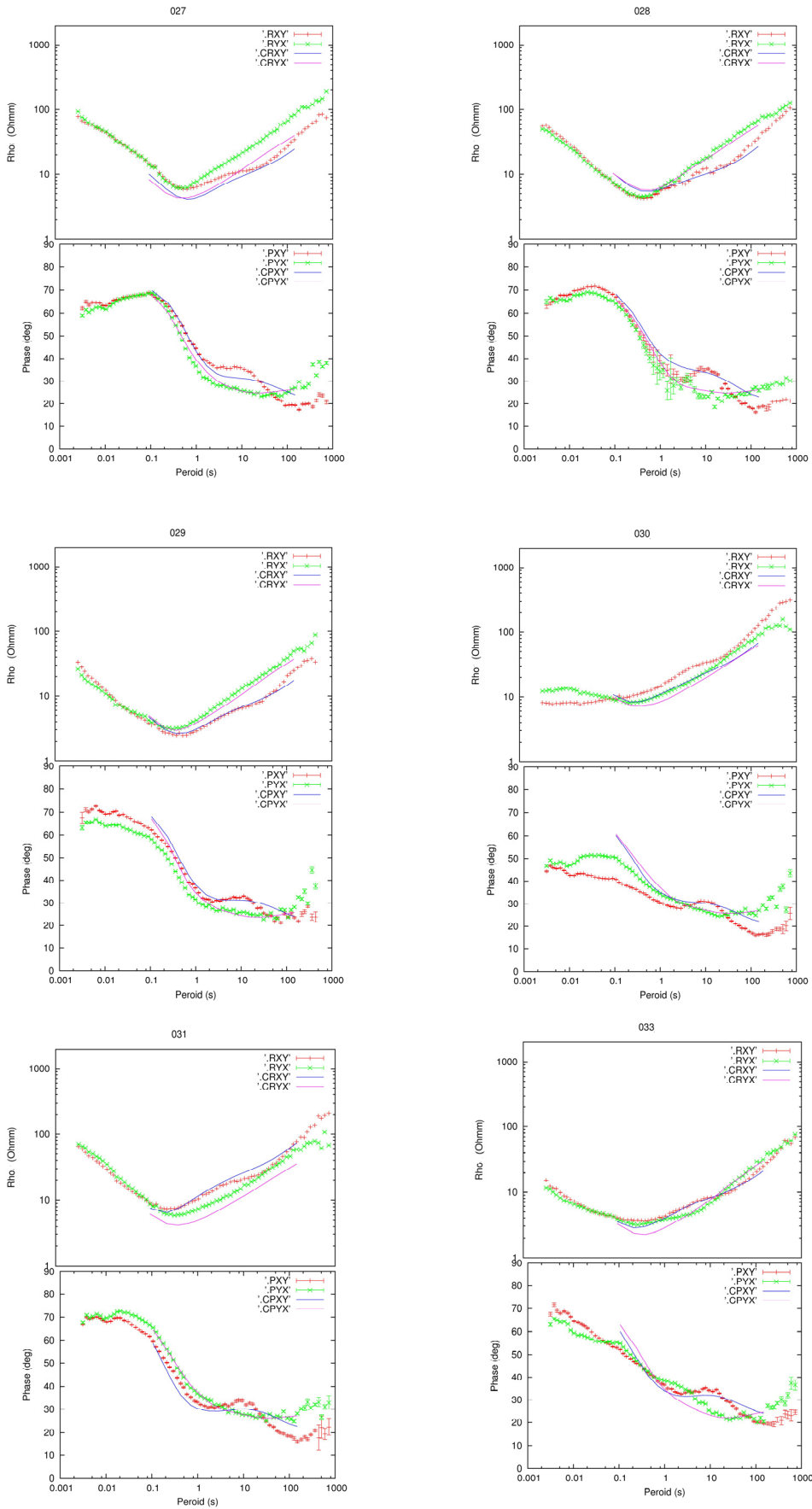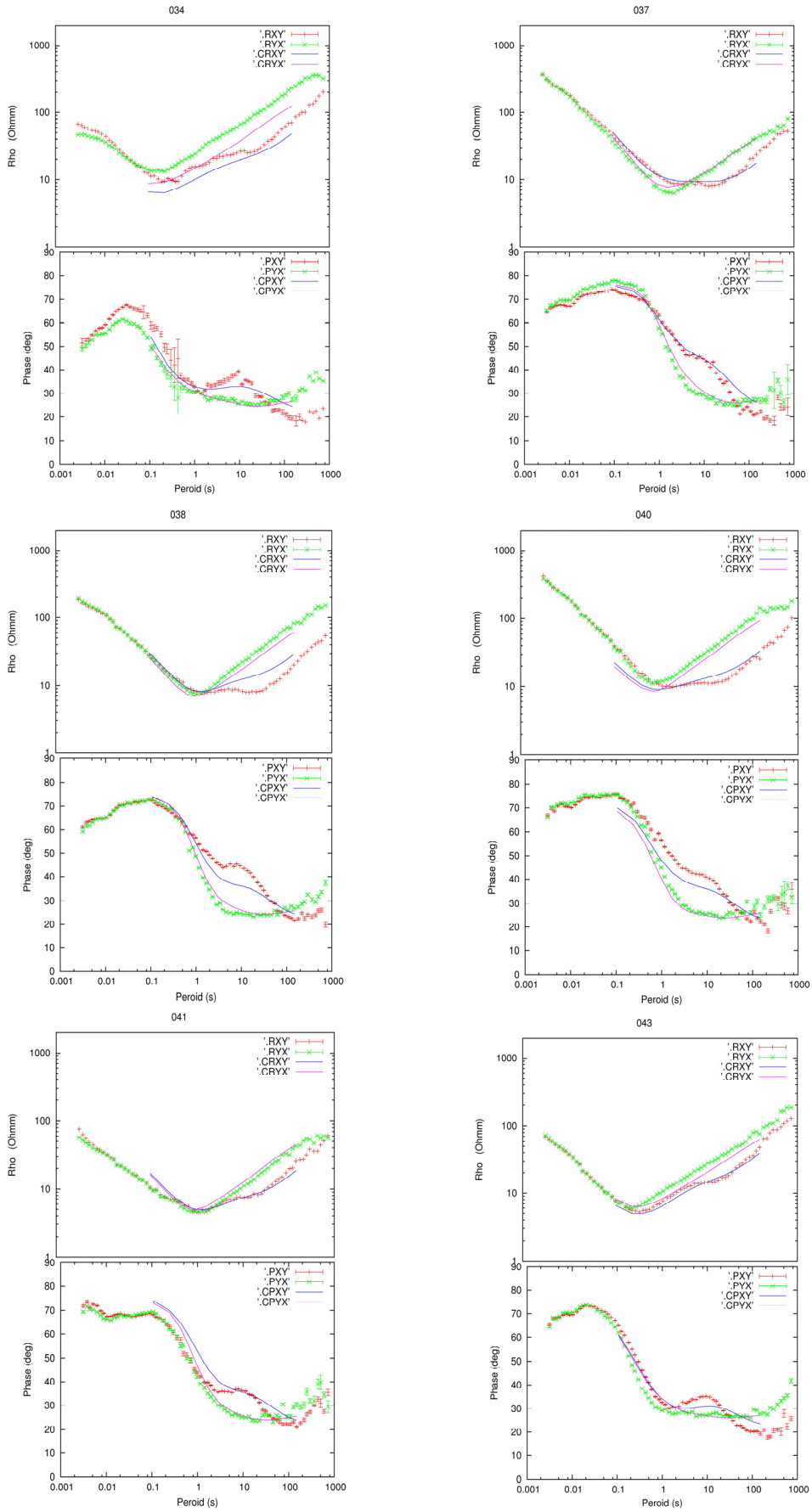FIGURE C1: (continued)
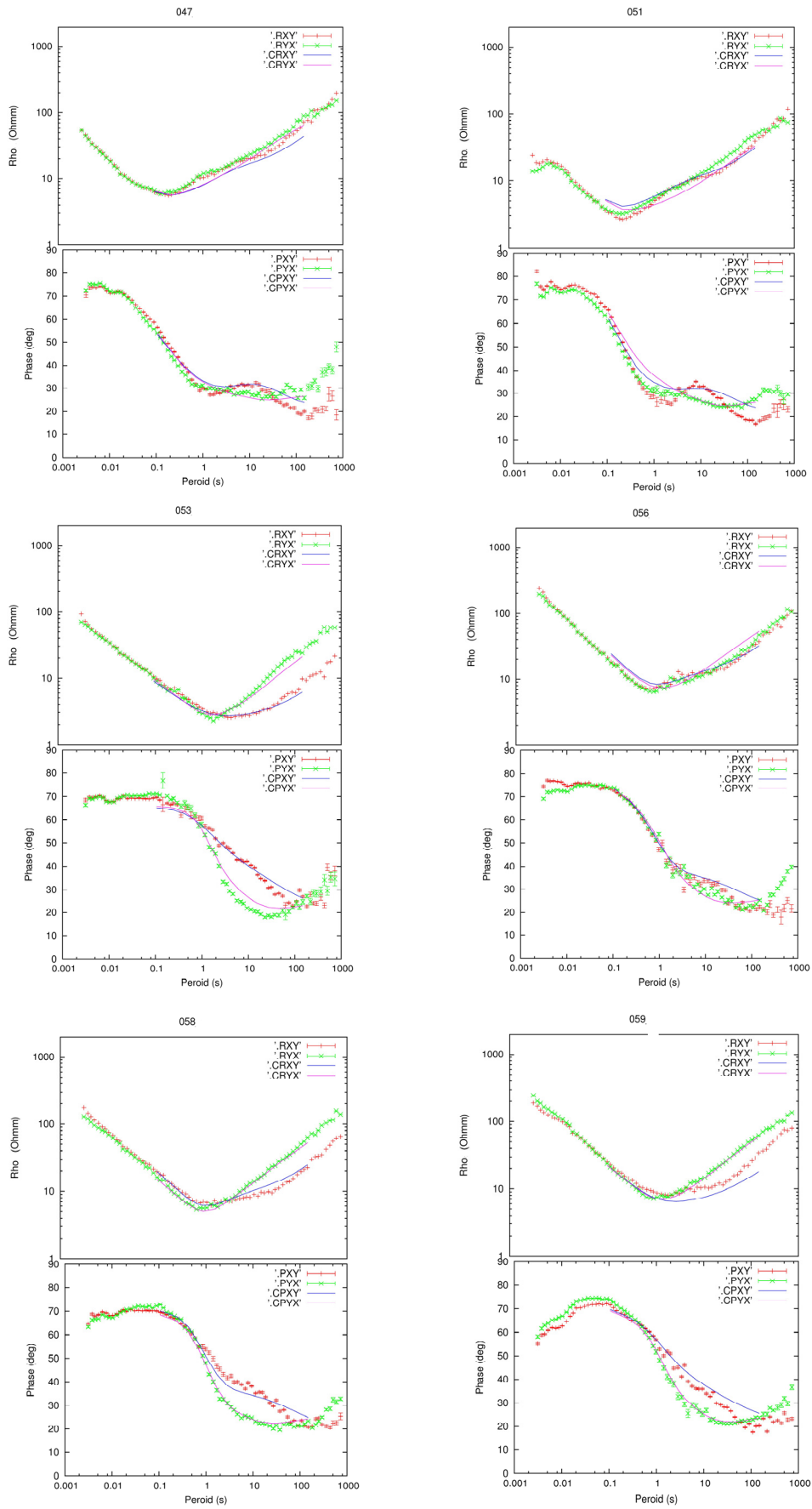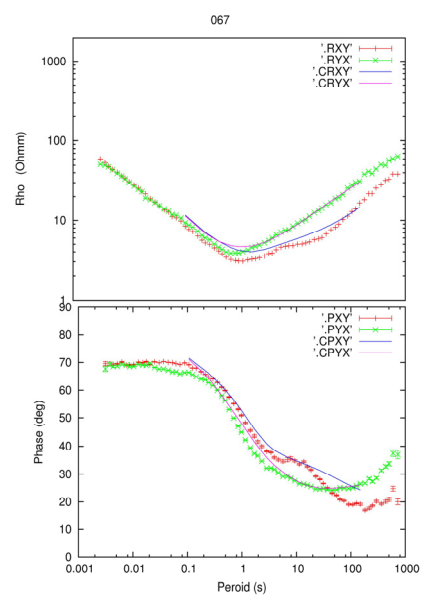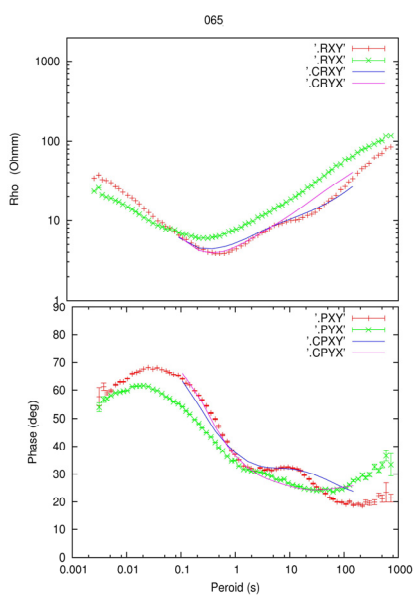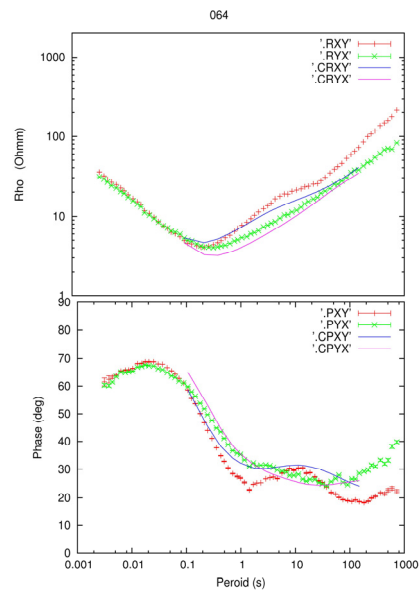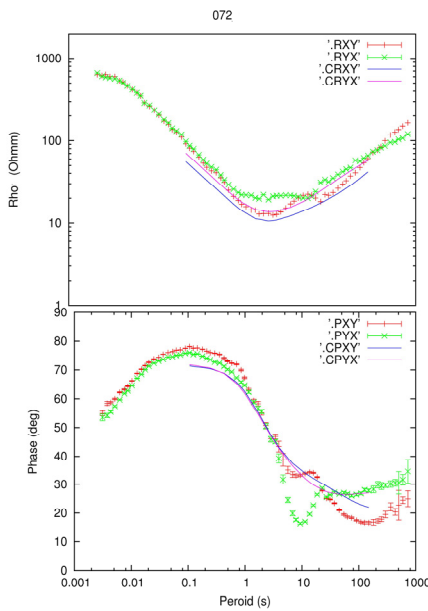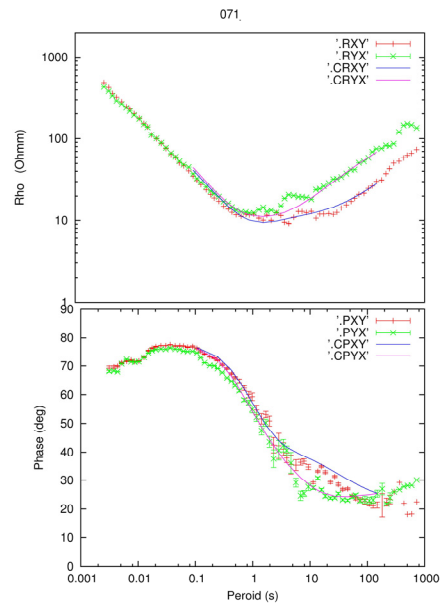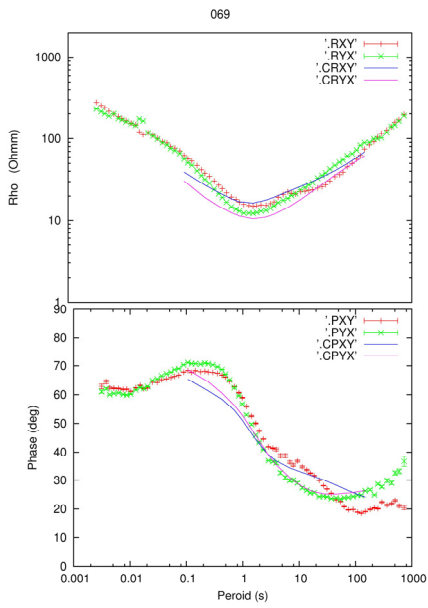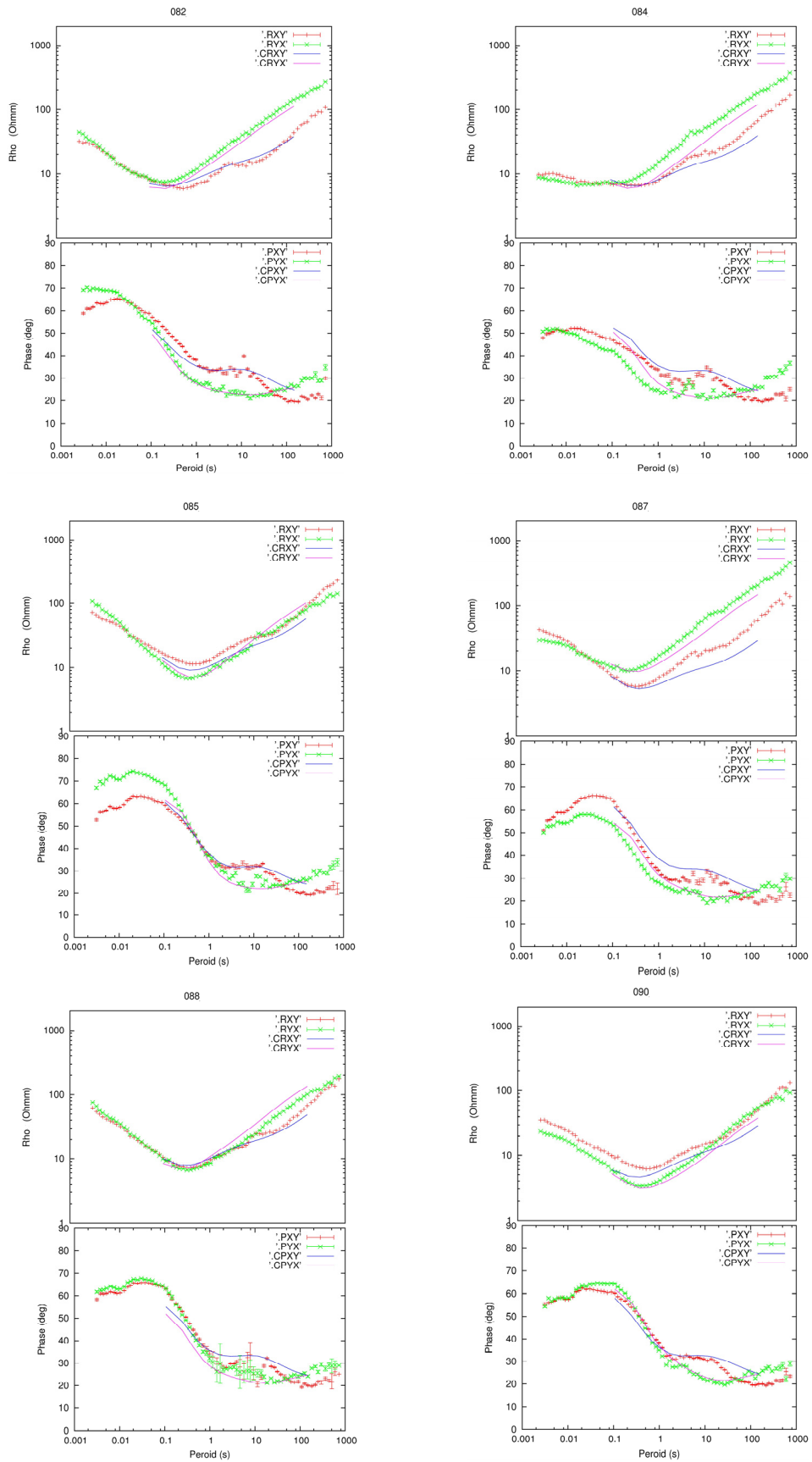
86

FIGURE C1: (continued)

87

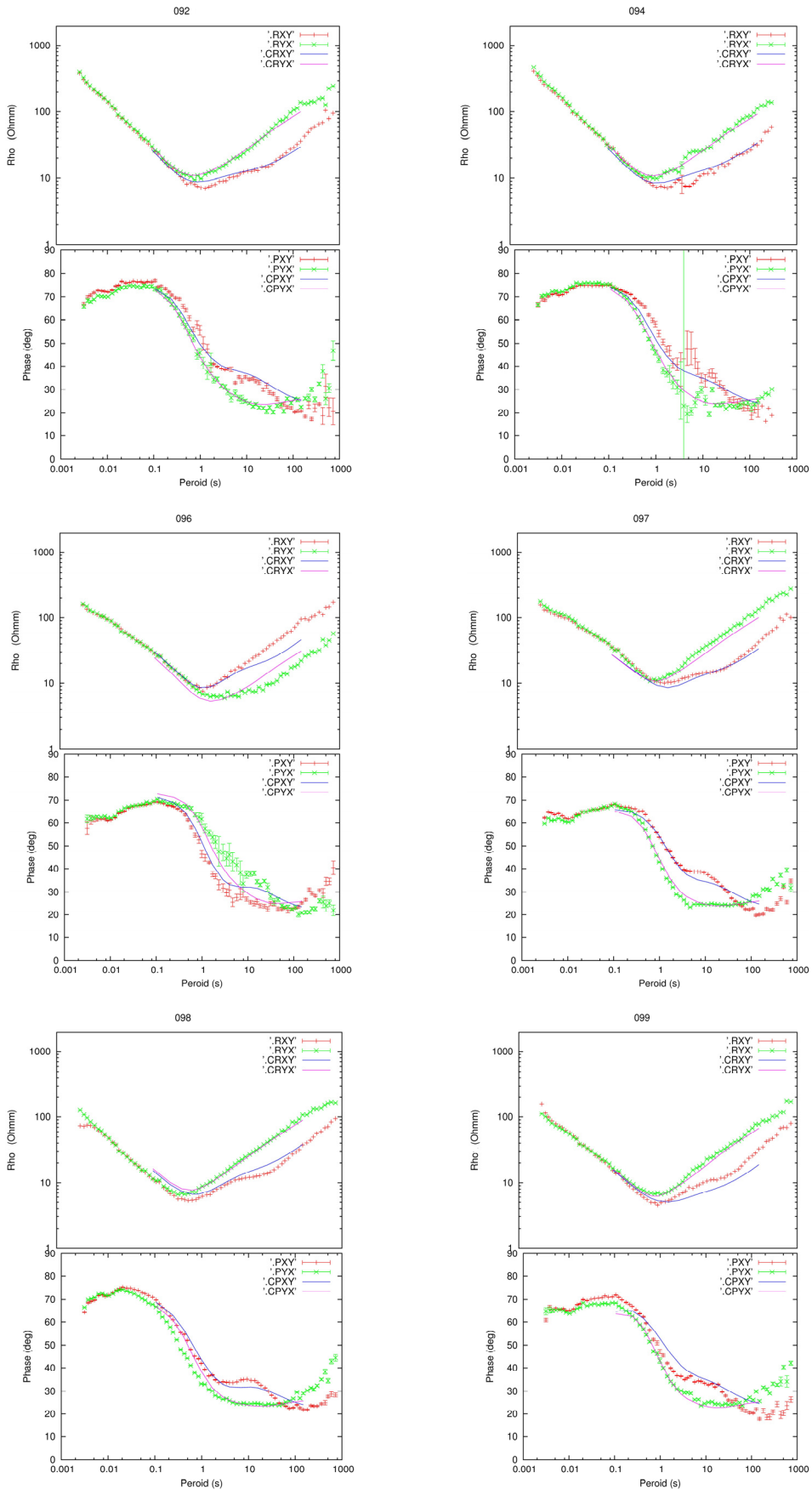FIGURE C1: (continued)

88

FIGURE C1: (continued)

FIGURE C1: (continued)

FIGURE C1: (continued)

FIGURE C1: (continued)

FIGURE C1: (continued)

FIGURE C1: (continued)